UNIVERSITY
of
GREENWICH

Greenwich Academic Literature Archive (GALA)
– the University of Greenwich open access repository
http://gala.gre.ac.uk

Citation:

Yin, Chunyan (2006) Experimental and modelling analysis on the performance of anisotropic conductive films as used in electronics packaging. PhD thesis, University of Greenwich.

Please note that the full text version provided on GALA is the final published version awarded by the university. "I certify that this work has not been accepted in substance for any degree, and is not concurrently being submitted for any degree other than that of (name of research degree) being studied at the University of Greenwich. I also declare that this work is the result of my own investigations except where otherwise identified by references and that I have not plagiarised the work of others".

Yin, Chunyan (2006) Experimental and modelling analysis on the performance of anisotropic conductive films as used in electronics packaging. ##thesis_type##, ##institution##

Available at: http://gala.gre.ac.uk/6355/

Contact: gala@gre.ac.uk

Declaration

I certify that this work has not been accepted in substance for any degree, and is not concurrently submitted for any degree other than that of Doctor of Philosophy (Ph.D.) of the University of Greenwich. I also declare that this work is the result of my own investigations except where otherwise stated.

Chunyan Yin
....

Chunyan Yin

....

Prof. Chris Bailey
(Supervisor)

Lu Hua
....

Dr. Hua Lu
(Supervisor)

Abstract

The aim of this research is to understand the failure modes and mechanisms of adhesive materials used to flip-chip bond a silicon die onto a polyimide substrate. The bonding material investigated in this research is called Anisotropic Conductive Film (ACF). This is a promising interconnection material and has gained extensive interest in the electronics packaging industry.

Both experimental and finite element analysis (FEA) methods were used in order to investigate the behaviour of the ACF materials when subjected to certain manufacturing and environmental testing conditions. The manufacturing condition investigated was a subsequent solder reflow process on an ACF flip-chip bonded device. The environmental testing condition investigated was the moisture test.

For the manufacturing condition, both experimental and modelling results demonstrate the impact of a subsequent reflow process on the behaviour of the ACF joint. Typical failures observed after this process were cracks at the pad/particle interface. This failure mode was more severe with a higher peak reflow temperature. This was also found using FEA where high tensile stresses were predicted in these regions. FEA modelling was also used to help identify the mechanisms leading to these failures. This is primarily due to the Coefficient of Thermal Expansion (CTE) miss-match in the materials and the elastic/plastic deformation behaviour of the conductive particle. Important design variables that can minimise these failures are the Young's Modulus and CTE of the adhesive and the height of the bump on the die.

For the environmental testing condition, an autoclave test at 121°C, 100%RH and pressure of 2atm was used. More than 85% of the ACF joints failed during the first 24 hours of testing. The failure mode observed was cracking along the interface between the adhesive and substrate and pad. A macro-micro modelling approach was used to help identify the mechanisms leading to these failures. It was found that most of the damage is caused by moisture diffusion and associated swelling. Important design variables that will help minimise this mode of failure are: Coefficient of Moisture Expansion (CME) and Young's Modulus of the adhesive and the height of the bump on the die.

Acknowledgments

I would like to sincerely thank both of my supervisors, Prof. Chris Bailey and Dr. Hua Lu for their supervision, guidance and encouragement during each stage of my study. Also I would like to thank all my colleagues at the University of Greenwich who have given me advices and shown the interests to my research.

I would like to express my deep gratitude to Prof. Yan-Cheong Chan within the Department of Electronic Engineering at City University of Hong Kong for initiating this joint Ph.D. program and all the support offered throughout my study. I would like to thank my colleagues at City University of Hong Kong for the support in the experimental work and in particular, Ms Sai Choo Tan, for her time and kind assistance for the work conducted at EPA Centre.

I would like to thank my parents for their encouragement through my Ph.D. study. My husband, Mr Guangbin Dou who is pursuing his Ph.D. at Loughborough University is deserved to be appreciated for his support and understanding, during the last ten years, we have been studying side by side all the time.

Finally, I would like to acknowledge the University of Greenwich and City University of Hong Kong for the financial support to undertake this research.

Table of Contents

ABSTRACT .... **I**

ACKNOWLEDGMENTS .... **II**

TABLE OF CONTENTS .... **III**

LIST OF FIGURES .... **IX**

LIST OF TABLES .... **XIII**

GLOSSARY .... **XIV**

CHAPTER 1: INTRODUCTION **1**

1.1 Background 1

1.2 Aims and Objectives of This Research 4

1.3 Layout of This Thesis 6

1.4 Original Techniques and Findings 7

CHAPTER 2: LITERATURE REVIEW **9**

2.1 Experimental Studies 9

2.1.1 ACA Materials 9

2.1.2 Curing Methods and Bonding Parameters 14

2.1.3 Environmental Testing 16

2.2 Computer Modelling 18

2.2.1 Flow Analysis of Bonding Process 19

2.2.2 Mechanical and Electrical Behaviour of Conductive Particles 23

2.2.3 Moisture Absorption and Induced stresses 27

2.3 Summary 30

CHAPTER 3: FLIP CHIP TECHNOLOGY **31**

3.1 Introduction 31
3.2 IC Assembly Technologies 33
3.2.1 Wirebonding 33
3.2.2 Tape Automated Bonding (TAB) 34
3.2.3 Flip Chip 35
3.3 Materials Used for Interconnections 36
3.3.1 Solder Alloys 37
3.3.1.1 Tin-Lead Solder 37
3.3.1.2 Lead-Free Solder 37
3.3.2 Electrically Conductive Adhesives (ECAs) 40
3.3.2.1 Isotropic Conductive Adhesives (ICAs) 40
3.3.2.2 Anisotropic Conductive Adhesives (ACAs) 42
3.3.2.3 Non Conductive Adhesives (NCAs) 43
3.4 Reliability Testing 44
3.4.1 Reliability and Failure 44
3.4.2 Reliability Test and Standard 45
3.4.2.1 Non-Accelerated Test 45
3.4.2.2 Accelerated Test 46
3.4.3 Failure Models 47
3.5 Applications of ACF Flip Chips 47
3.5.1 Liquid Crystal Display 48
3.5.2 Disk Drive 49
3.5.3 Limitations for Further Applications 50
3.6 Summary 51

CHAPTER 4: RELIABILITY OF ACFS FOR FLIP CHIP ON FLEX APPLICATIONS: AN EXPERIMENTAL STUDY 53

4.1 Introduction 53
4.2 Experimental Design 56
4.2.1 Materials 57

4.2.1.1 Silicon Die........58
4.2.1.2 Flexible Substrates........58
4.2.1.3 Anisotropic Conductive Film (ACF)........59
4.2.2 Flip Chip Bonding Process........62
4.2.3 Joint Resistance Measurement........65
4.3 Results and Discussion........66
4.3.1 Bonding Conditions........67
4.3.1.1 Bonding Pressure........67
4.3.1.2 Bonding Temperature........70
4.3.1.3 Bonding Time........71
4.3.2 DSC Test Results........72
4.3.3 Reliability Tests........75
4.3.3.1 Joint Resistances and Failure Rate........76
4.3.3.2 Scanning Electron Microscope (SEM) Photos........78
4.3.3.3 Effect of Solder Reflow........81
4.4 Conclusions........83

CHAPTER 5: MODELLING OF THE EFFECT OF SOLDER REFLOW ON ACF PERFORMANCE........85

5.1 Computational Modelling........85
5.1.1 Geometry and Mesh Model........86
5.1.2 Modelling Assumptions........88
5.1.3 Modelling Results........89
5.1.4 Parametric Study........91
5.1.4.1 Effect of the CTE of the Adhesive Matrix........91
5.1.4.2 Effect of the Young's Modulus of the Adhesive Matrix........92
5.1.4.3 Effect of the Bump Height........93
5.2 Sensitivity Analysis........96
5.2.1 Scaled and Un-scaled Design Points........97
5.2.2 Sensitivity Test Results........100

5.3 Impact of Moving From Lead to Lead Free Soldering 101

5.4 Conclusions 105

CHAPTER 6: HYGRO-MECHANICAL ANALYSIS OF AN ACF ASSEMBLY IN AUTOCLAVE TEST 106

6.1 Introduction 107

6.2 Computer Modelling Technique 107

- 6.2.1 Challenges in Modelling the ACF Assembly 108
- 6.2.2 Macro-Micro Modelling Technique 108
- 6.2.3 Interpolation of the Displacement Fields 110

6.3 Demonstration of the Macro-Micro Modelling Technique 113

- 6.3.1 Geometry and FE Models 113
- 6.3.2 Material Properties 116
- 6.3.3 Modelling Results and Error Analysis 116

6.4 Moisture Diffusion Prediction 120

- 6.4.1 Conservation Equation in PHYSICA 120
- 6.4.2 Wetness Fraction Approach 121
- 6.4.3 Test Case: One Dimensional Moisture Diffusion 124

6.5 Modelling Analysis of an ACF flip chip Assembly 127

- 6.5.1 Geometry and Mesh Model 127
- 6.5.2 Material Properties and Modelling Assumptions 129
- 6.5.3 Modelling Results 130
  - 6.5.3.1 Moisture Diffusion 130
  - 6.5.3.2 Moisture Induced Stress 133
  - 6.5.3.3 Temperature Induced Stresses 136
- 6.5.4 Parametric Analysis 137
  - 6.5.4.1. Effect of the CME of the Adhesive Matrix 138
  - 6.5.4.2. Effect of the Young's Modulus of the Adhesive Matrix 139
  - 6.5.4.3. Effect of the Bump Height 140

6.6 Failure Mechanisms 141

6.7 Conclusions 142

CHAPTER 7: CONCLUSIONS AND FURTHER WORK 144

7.1 Conclusions 144

7.2 Further Work 146

7.2.1 Experiments 147

7.2.2 Computational Modelling 147

7.2.3 Future Challenges with ACAs 148

APPENDICES 149

A. Differential Equation of Diffusion 149

B. Material Behaviours 152

B.1 Elasticity 153

B.2 Plasticity 153

B.3 Rate Dependent Material Behaviour 154

C. Finite Element Method (FEM) 155

C.1 Linear Elasticity 157

C.1.1 Equilibrium Equations 157

C.1.2 Discretization of Solution Domain 160

C.1.3 Discretization of Equilibrium Equations 164

C.1.4 Solution Procedure 167

C.2 Elasto Visco-Plasticity 168

C.2.1 Elasto-Viscoplasticity Material Model 168

C.2.2 Three Dimensional Elasto-Viscoplastic Model 170

C.2.3 A Newon-Raphson-Based Iteration Method 172

D. PHYSICA - A Simulation Tool 175

E. Liquid Crystal Display: A Case Study Using PHYSICA 176

E.1 Problem Description 178

E.2 Geometry and Computational Mesh 178

E.3 Boundary Conditions and Material Properties 180

E.4 Solution of the Modelling Analysis 181
E.5 Results Analysis 182

REFERENCES 185

List of Figures

Figure 1.1: The first three levels in the electronics packaging [1] 2

Figure 2.1: A typical ACA connection system 10

Figure 2.2: Structure of bumpless and Au bump dies 11

Figure 2.3: Structure of a double layer ACF and its assembly 13

Figure 2.4: Water absorption at five temperature levels (100%RH, 1atm) (courtesy of Cao *et al.* [38]) 16

Figure 2.5: Schematic drawing of an ACA flow during the bonding [51] 20

Figure 2.6: Deformation distribution of different particle systems, (a) rigid particle system, (b) deformable particle system and (c) fully deformable system (courtesy of Wu *et al.* [59]) 24

Figure 2.7: Temperature iso-surfaces during bonding at different times of the process (courtesy of Dudek *et al.* [54]) 24

Figure 2.8: Stress σ_{yy} and particle deformation caused by bonding at 190 ^{o}C and subsequent cooling to room temperature (courtesy of Dudek *et al.* [54]) 25

Figure 2.9: Predicted particle resistance for different degree of deformation, (a) for *Au/Ni*-polymer with various metal thicknesses, (b) for solid metal particles (courtesy of Määttänen *et al.* [68]) 27

Figure 2.10: Finite element model (a) structure of the global and local area (b) mesh information (courtesy of Mercado *et al.* [12]) 29

Figure 3.1: Moore's Law predicts the IC integration to double every 18 months 32

Figure 3.2: Example of an IC package 33

Figure 3.3: Chip on substrate interconnection technologies 34

Figure 3.4: Flip chip process using solder alloy 36

Figure 3.5: Typical interconnection systems using ICA, ACA and NCA 41

Figure 3.6: Idealize bathtub curve 44

Figure 3.7: A typical LCD assembly [96] 48

Figure 3.8: The disk drive using ACF technology [97] 49

Figure 4.1 A typical display using ACF and solder together 54

Figure 4.2: The flow chart of the experimental procedure 57

Figure 4.3: Pattern of the silicon die 58

Figure 4.4: Pattern of the polyimide substrate 59
Figure 4.5: A typical ACF made by Ni/Au coated polymer particles 61
Figure 4.6: Flip chip bonding process using the ACF 63
Figure 4.7: Top view of the ACF flip chip sample 64
Figure 4.8: Toray semi-auto flip chip bonder (Toray SA2000) 64
Figure 4.9: The four point method to test the joint resistance 65
Figure 4.10: The facilities used for measuring the joint resistances 66
Figure 4.11: Variation of joint resistance with bonding pressure 67
Figure 4.12: ACF joints, bonded at (a) lower (b) appropriate and (c) higher pressure 69
Figure 4.13: Variation of joint resistances versus bonding temperature 70
Figure 4.14: Variation of joint resistance with bonding time 72
Figure 4.15: Curing profile of (a) Raw ACF (b) Cured ACF and (c) Cured ACF with reflow treatment 74
Figure 4.16: The facility used for autoclave test 75
Figure 4.17: ACF joint failure rate and open joint rate 77
Figure 4.18: Joint resistance of ACF joints during autoclave test 77
Figure 4.19: SEM photos showing the ACF interconnections 79
Figure 4. 20: SEM photos of the ACF interconnections after 24 hours autoclave test 82
Figure 5.1: Section view of the structure of the ACF joint 86
Figure 5.2: FE model of an ACF joint 87
Figure 5.3: Boundary conditions used in the modelling 88
Figure 5.4: Stress σ_{yy} distribution in the ACF joint 90
Figure 5.5: Plastic strain distribution in the ACF joint 90
Figure 5.6: The relationship between the interfacial stresses and the CTE of the adhesive matrix 92
Figure 5.7: The relationship between the interfacial stress and Young's Modulus of adhesive matrix 93
Figure 5.8: The relationship between the interfacial stresses and the bump height 94
Figure 5.9: ACF interconnection with *Au* bump 95
Figure 5.10: Sensitivity of interfacial stress of design variables and their interactions 100
Figure 5.11: Response Surface predictions .vs. Finite Element predictions 101
Figure 5.12: Relationship between the interfacial stress and the peak reflow temperature 102

Figure 5.13: SEM photos showing the ACF interconnection through conductive particles (a) as-bonded at 200°C, 86.2MPa, 10s, and after reflow with the peak temperature at (b) 210°C (c) 230°C and (d) 260°C 104

Figure 6.1: Interpolation from the global to local mesh 111

Figure 6.2: Structure and geometry of a simplified flip chip solder joint. 114

Figure 6.3: Mesh details of the macro, micro and global model 115

Figure 6.4: Strain distribution predicted by using the macro-micro model (the left row) and the global model (the right row) 117

Figure 6.5: Strain distribution in solder predicted by using the macro model (left row) and the global model with a fine mesh (the right row) 119

Figure 6.6: Moisture concentrations across bi-material interface 121

Figure 6.7: Wetness fraction across bi-material interface 122

Figure 6.8: The mesh of the 1D model diffusion model 124

Figure 6.9: The analytical and modelling results 125

Figure 6.10: Effect of the mesh density and time step on the numerical results 126

Figure 6.11: The layout of the silicon chip 127

Figure 6.12: The mesh of the macro model 128

Figure 6.13: The mesh information of micro model 129

Figure 6.14: Wetness fractions at the centre of the ACF layer 131

Figure 6.15: The wetness fraction distribution in ACF layer 132

Figure 6.16: The deformation and stress distribution of the whole package 133

Figure 6.17: Pattern of the Von-Mises stress distribution 134

Figure 6.18: Pattern of the tensile stress distribution 134

Figure 6.19: The interfacial stresses due to moisture absorption 135

Figure 6.20: The pattern of the normal stress distribution due to temperature change 136

Figure 6.21: Moisture and thermal induced interfacial stresses 137

Figure 6.22: The interfacial stresses with different CME values of the adhesive matrix... 138

Figure 6.23: The interfacial stresses with different Young's Modulus value of the adhesive matrix 139

Figure 6.24: The interfacial stresses with different bump height 140

Figure A.1: Element of volume 150

Figure B.1: Plastic material behaviour. (a) Elastic, perfectly plastic and (b) elastic, linear work hardening 154

Figure C.1: Mesh elements and mesh nodes 160
Figure C.2: Mesh element in global and local coordinates 161
Figure C.3: Sketch of a mechanical model that reflects the basic physics of elasto-viscoplastic deformation 169
Figure E.1: The LCD sample to be modelled 177
Figure E.2: A section view of the LCD and material information 177
Figure E.3: The finite element model 179
Figure E.4: The boundary condition used in modelling 180
Figure E.5: The deformation of the package at 100°C 182
Figure E.6: Shear stress distribution in the package at 100°C 183
Figure E.7: Values of shear stress at weak locations 183
Figure E.8: Tensile stress at the weak locations 184

List of Tables

Table 3.1: Lead and Lead-free solder alloy under study [83] 39
Table 4.1: Specification of the ACF used in this experiment........ 60
Table 4.2: The bonding parameters used in experiment........ 61
Table 4.3: The results to show the reflow effect........ 81
Table 5.1: Material characteristics used for this simulation........ 89
Table 5.2: The results to show the reflow effect........ 95
Table 5.3: Scaled values of the design variables 98
Table 5.4: Un-scaled values of the design variables and response of interest........ 99
Table 5.5: Joint resistance with different peak temperature of reflow profile........ 103
Table 6.1: Material characteristics used for this simulation........ 116
Table 6.2: Certain values from three models 118
Table 6.3: The relationship of the thermal and moisture simulation [111]........ 123
Table 6.4: Material properties used for the one-dimensional diffusion simulation........ 125
Table 6.5: Moisture properties of the ACF and polyimide substrate........ 130
Table A.1: The relationship of the thermal and moisture simulation........ 152
Table E.1: The geometry details of the LCD package 179
Table E.2: The basic material information........ 181

Glossary

ACA	Anisotropic Conductive Adhesive
ACF	Anisotropic Conductive Film
ACP	Anisotropic Conductive Paste
AMLCD	Active Matrix Liquid Crystal Display
BGA	Ball Grid Array
CAD	Computer Aided Design
CFD	Computational Fluid Dynamic
COF	Chip on Flex
COG	Chip on Glass
CRT's	Cathode Ray Tubes
CTE	Coefficient of Thermal Expansion
CME	Coefficient of Moisture Expansion
DC	Direct Current
DOE	Design of Experiment
DSC	Differential Scanning Calorimeter
ECA	Electrically Conductive Adhesive
ELV	End of Life Vehicles
FCOF	Flip Chip on Flex
FEA	Finite Element Analysis
FEM	Finite Element Method
FPC	Flexible Printed Circuit
FPP	Four Point Probe
FTIR	Fourier Transform Infrared Spectrophotometer
FV	Finite Volume
HDD	Hard disk drive

HGA	Head Gimbal Assembly
IC	Integrated Chip
ICA	Isotropic Conductive Adhesive
I/O	Input/Output
ITO	Indium-Tin-Oxide
LCD	Liquid Crystal Display
LCP	Liquid Crystal Polymer
NCA	Non Conductive Adhesive
PCB	Printed Circuit Board
PCT	Pressure Cooker Test
PEN	Polyethylene Napthalate
PET	Polyethylene Terephthalate
RH	Relative Humidity
RS	Response Surface
RoHS	Restriction of Hazardous Substrates
SAC	Tin-Silver-Copper
SEM	Scanning Electronic Micrographs
SMT	Surface Mount Technology
TAB	Tape Automated Bonding
Tg	Glass Transition Temperature
2D	Two dimensional
3D	Three dimensional
UBM	Under Bump Metallization
UV	Ultraviolet
VFMW	Variable Frequency Microwave
WEEE	Waste from Electrical and Electronic Equipment

Chapter 1

Introduction

This Chapter describes the background to the research undertaken and the aims. Also discussed are the layout of this thesis and a summary of the achievements made from this research.

1.1 Background

Major trends for today's electronic products are to make them smaller, lighter and cheaper, while at the same time more friendly, functional, and reliable. These demands have induced the rapid development of high-density, multi-function electronic components with increasing functionality packaged into smaller and smaller spaces. For example, in 1992 the typical video camera consisted of over 1800 components, with a density of 12 components per cm^2, and occupied $2380mm^3$. In 1998 the video camera consisted of only 848 components, with a density of 21 components per cm^2 and occupied only $1598mm^3$. The size of the video camera was expected to be further reduced by 50 percent by year 2002 [1].

Electronics packaging is a key technology that must be addressed in making robust, miniaturized and integrated products. Packaging is defined as the bridge that connects the Integrated Circuit (IC) and other components into a system-level board to form the product [1][3]. Figure 1.1 shows a schematic representation of the packaging

capability to produce high density I/O using low temperature assembly which is very attractive for many applications which cannot withstand the high temperatures associated with metallic solder connections. Liquid Crystal Displays (LCDs) are one application where anisotropic conductive materials have made a major impact.

ACAs consist of electrically conductive particles within a polymer matrix. This material can be placed between an IC and a substrate to form the electrical interconnection. This connection is anisotropic as the current can only travel in the vertical direction.

The earliest concept of ACAs occurred in the 1950s and since then extensive research and development within the community has taken place [4]. In the early 1980s, several companies, such as Sheldahl in the United States and Sony in Japan, were facing problems connecting low temperature materials. At this time Sheldahl and other flexible circuit manufacturers focused many resources to the problem of connecting ICs to low temperature circuit boards. In Japan there was a concerted effort in solving the connection problem for substrates used for liquid crystal displays.

The Japanese company Sony first introduced samples of an interconnect film that contained carbon fibres which were oriented in parallel and acted as the electrical conductors. At this time companies in the United States suggested that the conductors within the polymer matrix should be spherically-shaped metals and both Sheldahl and Amp produced ACAs using silver particles in 1985. Since then, considerable research has been undertaken around the world to develop new ACA materials. Today, ACAs are available in just every form and type ranging from liquid pastes to dry films, using thermosets and thermoplastics.

Anisotropic Conductive Films (ACFs) are now popular interconnect materials especially in the flat-panel display, disk drive and smart card industries, where the traditional solder alloys are becoming very difficult to achieve both fine pitch and low temperature assembly requirements. For example, the requirements for better resolution and colour quality of LCD panels induce higher numbers of pixels and more

I/Os to be interconnected, thus the pitch size (i.e. the distance between the I/O pads) is becoming much finer. Using ACFs allows fine pitch connections of less than 100μm which is generally impossible to be connected using traditional solder alloys [5]. Lower processing temperature is another strength of ACFs compared to solder alloys since many components are sensitive to heat and cannot survive the solder reflow process where the peak temperatures can be as high as 250°C. For many electronic products and materials this temperature is far too high.

Adopting ACFs provides significant advantages of fine pitch connections and low temperature assembly. The material is also lead-free and hence satisfies many of the current environmental legislation restrictions stated in the European directives. The major concern with ACF materials is their reliability performance. Compared with the traditional metallic solder materials, especially the tin-lead solders, ACFs are very new with little documented reliability data.

1.2 Aims and Objectives of This Research

This research is motivated by the desire to improve the reliability performance of ACF materials and interconnections. The methodology used to undertake this research is based around both experimental work and finite element modelling.

The majority of published research for ACFs has focused on the bonding parameters (i.e. bonding temperature, pressure and time) and the behaviour of the material during accelerated life testing under thermal, vibration and moisture induced conditions. Although much work has been done, there are still some areas which are not fully understood and some questions still remain.

The electronic manufacturing industry is very interested in combining ACFs and solders onto the same board. This is for applications which require the fine pitch advantage of ACFs and the high reliability advantage of solders. The concern of this combining process is the behaviour of the ACFs when subjected to the high reflow temperatures required for solders.

Humidity and moisture diffusion into the ACF material results in stresses and is probably the major cause of failures with these materials [7][8][9][10][11][12][13]. Currently the failure mechanisms are still not well understood. One of the limitations of previous modelling research is mostly using the two dimensional (2D) models due to the difficulties caused by the multi-length nature of the problem, and thus the global effect was ignored. In some cases, three dimensional (3D) models of ACF flip chips were built, but the structure of each ACF joint was simplified [48][49][61].

The overall aims of this research project is to use both computer modelling and experimental failure analysis to investigate:

a) The ability to use both ACFs and solders on the same board. Can the ACF material withstand the high solder reflow temperatures?

b) The failure mechanisms of ACF materials when subjected to high humidity environments.

These aims will be achieved through:

1) Investigate on Flip-chip assembled IC devices with ACF materials using different bonding conditions. Subject these devices to solder reflow temperatures and undertake a failure analysis study.

2) Building finite element models of the above assembly and predicting the locations of high stress throughout the package and ACF materials when subjected to a solder reflow temperature.

3) Using Flip-chip assembly of ICs onto flex substrates with ACFs and subjecting these to high humidity environments. Undertaking a failure analysis study.

4) Building finite element models using a macro-micro approach to predict the behaviour of the ACF materials when subjected to a humidity environment.

These aims and objectives will provide an insight into the stress magnitudes and locations for ACF joints when subjected to a solder reflow profile and to investigate important design parameters that can minimise these stresses. With regards to the performance of ACF joints when subjected to high humidity test environments the study will provide an insight into the failure mechanisms and how specific changes to the geometry/material properties can increase the reliability of these materials. The study will also show how novel modelling technology can be used with experiments to help characterize the performance of electronical packaging materials.

1.3 Layout of This Thesis

There are 7 chapters in this thesis. The research background is presented in Chapter 1, which outlines the challenges in the electronics industry at present and explains why the research on ACFs is important.

In Chapter 2, a literature review of the recent activities about ACA assemblies is presented. More than 50 papers are referred and classified into two main areas: experiments and computational modelling.

An introduction of flip chip technology is given in Chapter 3, the most common connection materials used in flip chips ranging from solder alloys to electronically conductive adhesives (ECAs) are described. The concepts of reliability and failure analysis of electronic products are discussed and the applications of ACFs in LCDs and disc drives are presented.

Chapter 4 details the whole process of the experimental work from sample preparation to reliability testing. The effects of bonding parameters, solder reflow temperature and moisture absorption on the electrical/reliability performance of ACF joints are studied and the results are presented in joint resistance, curing degree, and Scanning Electronic Micrographs (SEM).

In Chapter 5, modelling analysis on the performance of ACF joints during solder reflow process is conducted. The parametric study considers the effect of the coefficient of thermal expansion (CTE), Young's modulus of adhesive and bump height on the interfacial stresses in an ACF joint. The failure mechanism of ACF joints during solder reflow is discussed based on both modelling and experimental results.

The moisture effects on the reliability performance of an ACF flip chip assembly are discussed in Chapter 6. The wetness fraction technique is introduced and the moisture diffusion in an ACF flip chip under autoclave test conditions is predicted. The moisture induced stress is analyzed and the effects of the coefficient of moisture expansion (CME) and Young's modulus of adhesive, and bump height, on the interfacial stresses are presented. The failure mechanism of the ACF joints in autoclave test is discussed based on both modelling and experimental results.

Finally, a summary of the achievements from this research and the possible further work are discussed in Chapter 7.

1.4 Original Techniques and Findings

Findings and developments from this research can be categorised as follows:

1. Conditions for the compatibility of ACF with traditional soldering technology have been demonstrated. Both reliability testing and computational modelling have been used to identify the impact of geometry and material properties on the performance of the ACFs after being subjected to the high reflow temperatures associated with soldering.

2. A moisture diffusion model was implemented into the finite element software: PHYSICA. This enabled the prediction of temperature, moisture and thermal/hygro stresses for the packaging components investigated.

3. A macro-micro modelling technique was developed to model phenomena taking place at the package (macro) and joint (micro) levels. 3D models of ACF flip chip assembly at both the macro and micro levels were developed.

4. In the solder reflow, the tensile stress along the interface between the conductive particle and metal pad tends to lift the bump from the pad causing the loss of the contact area and the increase in the contact resistance, this interfacial stress is much affected by the CTE value of the adhesive and the reflow peak temperature.

5. During the autoclave test, moisture diffuses mostly through the flexible substrate into the ACF layer; most ACF joints failed in the first 24 hours upon the moisture absorption. The moisture induced swelling effect contributes to the joint opening rather than the temperature effect.

This research work was involved in a collaboration research programme between the University of Greenwich and City University of Hong Kong. The computer modelling part of the work was undertaken at the University of Greenwich, and the experimental part of the work was undertaken at City University of Hong Kong. So far, this research work has resulted in 3 journal papers [126][127][128], 8 international conference papers [129][130][131][133][134][135][136][137] and 1 article for a trade magazine [138].

Chapter 2

Literature Review

This Chapter reviews the public domain literature on research for ACA materials. More than 50 publications are referred in order to provide a concise, structured overview in this research area. Most of the recent research is summarized and classified into two main areas, experiments and computer modelling. The research work undertaken by using experimental technique is presented first, and followed by computer modelling.

2.1 Experimental Studies

There is plenty of research can be found using experimental techniques in the academic literature. The topics can be classified into three main areas: ACA materials, curing method and bonding process, and environmental testing.

2.1.1 ACA Materials

ACA consists of an adhesive matrix and randomly distributed conductive particles. During the bonding process, some of the conductive particles are captured between the chip bumps and substrate pads, deformed to achieve the electrical path between the chip and substrate. The cured adhesive helps maintain the deformation of the conductive particles after the bonding process is finished. A typical ACA connection system is shown in Figure 2.1.

cured adhesive was studied by Zhang *et al.* [18]. Good performance was observed after considering the influence of bonding pressure, bonding temperature and moisture absorption. Strength between the ACFs and the aluminium was not affected seriously by bonding pressure but it increased with bonding temperature. It was suggested that the oxidation reaction could provide a fresh rough surface that may enhance adhesion strength. Tan *et al.* [9] reported the reliability performance of ACF flip chip assemblies using bumpless dies during the pressure cook testing, the joint resistance increased during the test and some micro cracks were observed along the interface between the copper trace and the adhesive. The formation of the oxidation layer on the top surface of the aluminium metallization was concluded as one of the main reasons for stress-corrosion cracking.

The reliability performance of the ACF filled with nickel particles or metal coated polymer particles during the thermal cycling test was compared by Frisk *et al.* [21]. The ACF filled with metal coated polymer particles showed less delamination after reliability testing, the nickel particles were more rigid than polymer particles and had less potential to compensate the expansion of the adhesive matrix when the temperature increased. Paik *et al.* [22] studied the effect of the non-conducting silica fillers on the thermo-mechanical performance of the modified ACA materials. The results suggested that the content of non-conducting fillers was a key factor which controlled the basic material properties of ACA composition. As the content increased, the storage modulus increased and the CTE below the glass transition temperature (Tg) decreased. The changes in these material properties induced better reliability performance of ACA packaging when using higher content of non-conducting fillers. Yim *et al.* [23] proved the effect of the CTE of the ACA on the thermal strain distribution in an ACA assembly, the thermal strain decreased proportional to the CTE of ACA. In another paper [24], the same group studied how to improve the thermal conductivity by incorporating silicon carbide (SiC) fillers into the ACA formulation.

Besides the filler types, the structure of ACF was also studied. The structure of a double layer ACF is shown in Figure 2.3. Compared to the single layer ACF, double

2.1.2 Curing Methods and Bonding Parameters

The demand for lighter, faster, and smaller microelectronic devices has created a need for new materials and new material processing methods. One of the biggest contributions to the processing time for advanced, high performance ICs and for packages is the time required to cure polymer dielectrics. A number of papers have focused on finding alternatives to thermal processing techniques for curing polymer dielectrics [24]. There are three kinds of curing methods that can be used for ACA assemblies, thermal curing, ultraviolet (UV) curing and microwave curing. Currently, most of ACA assemblies are finished by thermal curing and there is plenty of research that has been focused on the reliability performance of thermal curing joints.

ACAs cured by UV radiation offers several advantages over the conventional thermal curing process, these include rapid cure, little to no emission of volatile organic compounds and without affecting other components in the assembly [25]. Recent developed UV type ACAs have been suggested for use in heat sensitive electronics packages. In order to optimize the bonding conditions for the fabrication of UV curable ACA, research on smart card packaging has been carried out [15][16][17]. By comparing the experimental results in curing degree, shear strength of the ACA joint and the reading distance of the smart card samples, a set of parameters which gave better performance of the chip on flex (COF) bonding were determined. The higher UV light intensity, the longer exposure time led to a higher curing degree of the ACAs. The longer the post-curing time and the higher pre-bonding light activation intensity, the greater the shear load required to detach the test chip and the flexible substrate. These reliability studies have contributed to a better understanding of the failure mechanism of the UV cured ACA joints in smart card applications.

Microwave heating can significantly speed up the curing process of polymer and polymer-based composites. It also offers other advantages over conventional thermal processing techniques, such as selective heating of materials through differential absorption, penetrating radiation, controllable electric field distribution, and self-limiting reactions [26][27]. Therefore, a number of researchers have recently investigated the use of microwave radiation to cure adhesive joints [28][29][30], and single mode microwave cured adhesives for electronics packaging applications have been developed [31]. Recent theoretical work has studied the microwave transmission through the electrically conductive adhesive (ECA), heat generation and transfer inside the ECA and subsequently the microwave heating rate of the ECA. It showed that the penetration depth of the skin effect in the metal filler was significantly smaller than the one of a bulk metal material. The heat generation e.g. microwave power absorption was negligible in the metal filler due to its high electric conductivity [28]. Islam *et al.* [29] have studied the microwave preheating mechanism in order to decrease the bonding temperature of ACA assemblies and suggested if the microwave preheating was used for 2~3 seconds prior to the final bonding, the maximum curing temperature could be reduced by 10 to 170°C. Wang *et al.* [30] introduced a new technology called Variable Frequency Microwave (VFMW) and demonstrated it's capability in curing metal-filled ECAs.

With regards to the thermal curing joint, there are plenty of papers about the effects of the bonding parameters on the electrical and reliability performance of ACF joints [32][33][34][35][92]. It was proved that the performance of ACF interconnects was much affected by the curing level of the adhesive and the transformation degree of conductive particles which were mainly determined by the bonding parameters such as bonding pressure, bonding temperature and bonding time. The curing degree also affected the adhesion strength between the adhesive and the flex substrate. Hence the adhesion strength increased with the curing degree [36]. Tan *et al.* studied the thermal stability of ACF joints bonded at different bonding temperature ranging from 160°C to 225°C. ACF cured at a higher bonding temperature was thermally less stable, especially at 225°C as compared to at a lower bonding temperature. According to the Fourier Transform Infrared Spectrophotometer (FTIR) test results, high bonding temperature would promote a thermal oxidation reaction, this would later affect the reliability performance of the ACF [37].

2.1.3 Environmental Testing

Reliability of ACA assembles has presented a big challenge to the replacement of traditional soldering. The moisture effect on ACA packaging has been acknowledged as a key reliability issue and was studied experimentally [8][9][10][38]. Cao *et al.* [38] studied the interfacial adhesion of ACA assemblies under different environment conditions and found that the interfacial fracture toughness decreased by 25% after 48 hours exposure at 85°C/85%RH condition. The fracture usually occurred at the adhesive/polyimide substrate interface. It was also found that the moisture uptake was directly proportional to temperature and time as shown in Figure 2.4, where the higher the temperature, the higher the saturated moisture content was.

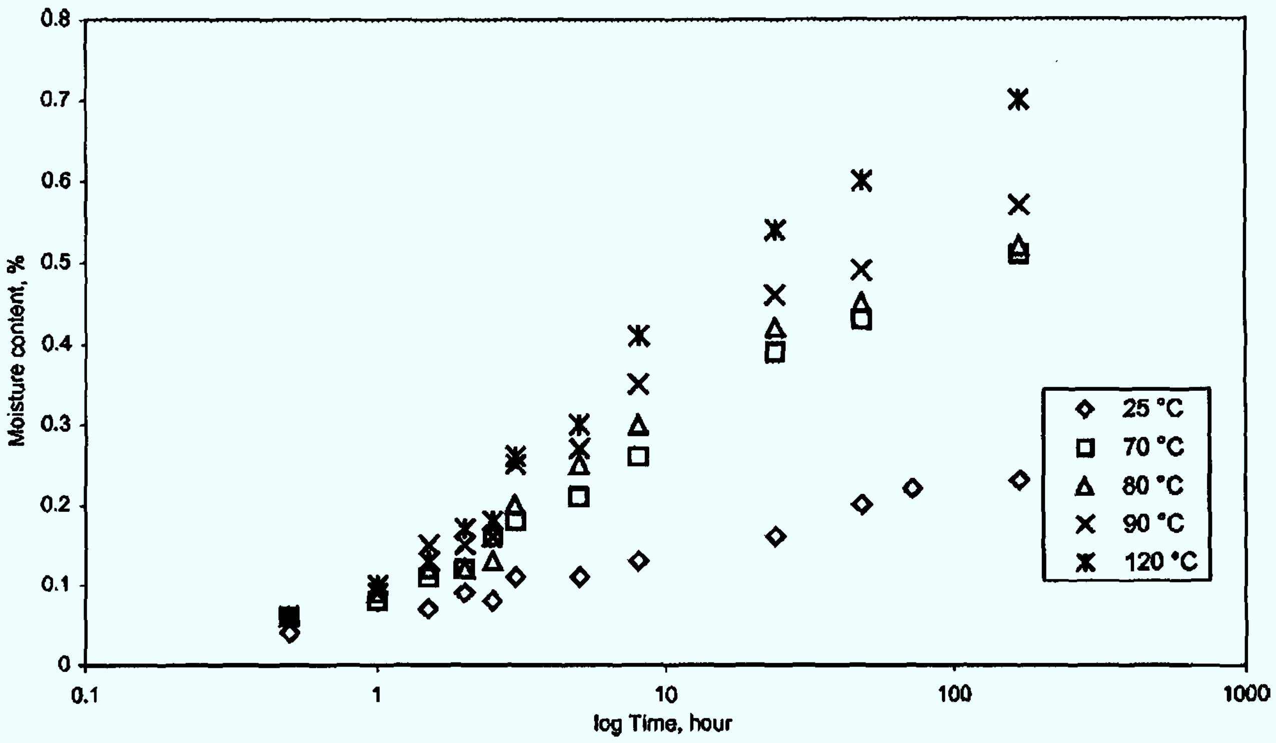

Figure 2.4: Water absorption at five temperature levels (100%RH, 1atm) (courtesy of Cao *et al.* [38])

The effect of moisture and temperature on the interfacial toughness of a polymer/metal interface was studied by Ferguson *et al.* [8], the results proved that the interfacial toughness was severely affected by the presence of moisture rather than temperature and the dominant failure mechanism for the reliability of the interface was attributed to moisture being directly present at the underfill/copper interface. Moisture was believed to be the most important factor in the degradation of an IC flip chip bonded on flexible substrates, especially cyclic exposure of adhesives to humidity and temperature was much more harmful to the quality of the flip chip on foil adhesive interconnects than continuous loading [44]. Lam *et al.* [40] developed a chemical kinetic model for describing the stress-assisted hydration of adhesion bonds; the model revealed that time to failure was dependent on the saturation water content, the stress gradient, and the water concentration gradient and was exponentially dependent on the peak stress. It was concluded that the bond degradation was governed by time-dependent stress-assisted hydration rather than governed by the water concentration alone.

Both the thermal cycling test (-40°C to 85°C) and humidity test (85°C/85%RH) were carried out by Frisk *et al.* [21] using ACF flip chip on Liquid crystal polymer (LCP) flexible substrate, delaminations were found within the ACF samples after 500 hours thermal cycling test, however, no delamination was found in the test samples after the humidity test. The thermal cycling reliability of ACF flip chips on organic substrates was studied by Kwon *et al.* [41]. The thermal induced deformation and warpages were investigated using in situ high sensitivity moiré interferometry and the effects of ACF materials on the thermal strain and susceptibility to delamination were studied. It suggested that the ACF properties had a significant role in overall reliability during thermal cycling testing, low CTE and high modulus can reduce the thermally induced shear strain in ACF layer and increased the overall thermal cycling lifetime. Ali *et al.* [42] also reported that the glass transition temperature of ACF had a significant effect on the reliability during the thermal cycling test. The test samples showed more increase in contact resistance when the thermal cycling profile exceeded the Tg of the ACF. Especially, the reliability of small pitch size flip chip on flex interconnections (pitch size < 80μm) was tested in 85°C/85%RH environment and -40 to 125°C thermal shock trials. It was suggested that reliable joints could be achieved by using suitable adhesive and optimum pad design [43].

The SMT-compatibility of adhesive flip chip on foil interconnections with 40μm pitch was studied by Vries *et al.* [45]. The samples were subjected to a certain well-defined humid environment (168 hours at 30°C/60%RH with an accelerated soak requirement of 40 hours at 60°C/60%RH) and then pass three times through a reflow oven. The gradual degradation in the subsequent humidity stress tests was observed and suggested due to the progressive decline of the initially present compressive force. The 40μm pitch assemblies have a failure distribution that is very much comparable to the 100μm type. The study has shown the feasibility in the moisure and reflow soldering test of such assemblies with a first level pitch down to 40μm.

The effect of solder reflow on the reliability performance of ACF assemblies was also studied by Chiang *et al.* [20] using bumpless dies. The ACF joint behaved differently under different reflow soldering profiles. The lower reflow temperature resulted in more reliable ACF joints by maintaining low contact resistance. By contrast, higher contact resistance was measured from the assemblies treated with higher reflow temperature. Under humidity aging (85°C/85%RH), bumpless chips proved to be unreliable due to a corrosion mechanism. Moreover, the ACFs showed degradation in chemical and physical properties, including modulus reduction, Tg depression, polymer hydrolysis, and surface swelling after exposing to humidity aging.

Other reliability tests results on ACFs include the impact test reported by Wu *et al.* [46], mechanical loading test reported by Tan *et al.* [47], the 3-points bending test reported by Rizvi *et al.* [48], and thermal aging test reported by Tan *et al.* [37] etc. All of this experimental research has generated much reliability data which is very useful for the electronics packaging industry.

2.2 Computer Modelling

Component package design and assembly process in electronics manufacturing require careful observation and pre-planning to achieve the ultimate goal of manufacturing low cost and reliable products. Use of simulation to help validate and understand reliability is required to assure that technologies are deployed with reasonable risk. Computer modelling method to predict reliability are needed to speed development processes [50].

Computer modelling analysis, in particular the finite element analysis (FEA), is being used as a powerful tool to predict the behaviour and responses of ACA assemblies during bonding process and reliability testing. The ACA bonding process is quite complicated and there are a number of key steps including pre-assembly, component placements, heating, assembly pressure applications, resin flow and particle compression, resin cure, assembly pressure release, and cooling [51]. So far, computer modelling work has been mainly focused on three aspects including flow analysis, thermal mechanical analysis and hygro-mechanical analysis.

2.2.1 Flow Analysis of Bonding Process

The success of the ACA bonding technology is sensitive to the number and distribution of the conductive particles trapped between chip bumps and substrate pads. The final position reached by a particle is determined by the flow of the adhesive during the bonding process. Therefore, to understand the adhesive flow behaviour during the bonding process is important for improving the ACA technology.

During the ACA bonding process, the compression/flow of the adhesive resin is divided into two distinct types [51]. These are: Type I flow, where the bumps on the substrate of components penetrate into the adhesive and the adhesive flows into the gaps between the pads; and Type II flow, where all of the space between the pads has been filled and the adhesive must then flow out from under the component. A typical situation of the particle flow is given in Figure 2.5.

The ACA bonding process is ideally expected to be finished when the type I flow is fully completed and the type II flow just starts. If the type I flow is not finished, voids could remain under the components, and thus reduce the bonding strength and the reliability of ACA assemblies. In the potential type II flow process, when the free

where R is an effective component radius and defined as $R = L/\sqrt{\pi}$, L is the component length/width. η_0 is the consistency of the adhesive and n is the power law index of viscosity and the viscosity, η, is given by:

$$\eta = \eta_0(\dot{\gamma})^{n-1} \tag{2.2}$$

Equation 2.1 assumes that $R>>h$, however the comparison of the prediction from Equation 2.1 with computational fluid dynamics (CFD) models showed that this equation was applicable with only small errors down to $R/h \approx 3$ [53]. For $n=1$, i.e. for a Newtonian fluid, Equation 2.1 is simplified to:

$$\frac{dh}{dt} = -\frac{2Fh^3}{3\pi\eta_0 R^4} \tag{2.3}$$

Dudek *et al.* [54] also modelled the adhesive compression process analytically using a 2D representation rather than the rotationally symmetric approximation used by Ogunjimi:

$$\frac{dh}{dt} = -\frac{Fh^3}{\eta b L^3} \tag{2.4}$$

where L is the pad/component length and b is the pad width. The 2D approximation of Equation 2.4 is likely to be more appropriate for assemblies where the pads have high length to width ratio, such as LCD to flex connections. Equation 2.4 neglects the effects of shear thinning of the adhesive, which significantly affects the resin flow and can not be safely used for type II flow if the adhesive resin flow is non-Newtonian.

Dudek *et al.* [54] also analyzed the type I flow process using numerical analysis with a single bump. The conductive particles were treated as dimensionless points embedded in a viscous matrix during the bonding. It demonstrated that the temperature gradients in the thickness of the foil can cause the viscosity gradients over the gap height which can slow down the process of particle emigration from the bumps remarkably.

Mannan *et al.* [53] modelled the initial stages of ACA joints assembly process and predicted the time required to squeeze out the adhesive from beneath the chip with the ignoring of the presence of the conducting particles in the adhesive. In the later report, Mannan *et al.* [55] studied the ACA squeezing process using a CFD software package: Fidap 7.52. This CFD modelling successfully took into account the detailed geometry of the assembly and showed the paths taken by infinitesimally small conducting particles.

Whalley *et al.*[56] successfully coupled the thermal conduction with flow process during the ACA bonding process using PHYSICA software with simplicity of the domain geometry. As the adhesive viscosity was highly temperature dependent and a temperature gradient through the adhesive film thickness was expected to create an asymmetrical flow distribution, this flow model was improved by allowing simulation of non-Newtonian behaviour with both shear rate and temperature dependent viscosity.

Based on the force versus displacement relationship measurement of a kind of particle, Whalley *et al.* took into account the stiffness of the particles and extended Equation 2.1 as below:

$$\frac{dh}{dt}=-\frac{n}{2n+1}\left(\frac{(n+3)(F-NK(D-h)^2)h^{2n+1}}{2\pi\eta_0 R^{n+3}}\right)^{1/n} \tag{2.5}$$

Where F is the total force carried by the particles, N is the total number of particles under compression and D is the particle diameter, K is a constant which, for the particles tested, was 0.20×10^{-9}, the predicted results showed that once the particles begin to compress they did slow down further flow out of the resin, but the flow did still continue and over compression of particles would still occur, although somewhat later than predicted by Equation 2.1.

2.2.2 Mechanical and Electrical Behaviour of Conductive Particles

The electrical performance of the ACA joint is dependent on the contact status between the conductive particles and pad metallization. During the bonding process, the conductive particles are deformed and locked in a compressive state which is maintained by the shrinkage force in the adhesive matrix. The stress created in the bonding process and reliability test process was studied in some reports by using modelling technique [54][58][59][60][61][62]. However, due to the phase change of the polymer foil from viscous to solid, the effect of the adhesive matrix on the stress generation of conductive particles during the bonding process was usually ignored.

Buratynski *et al.* [58] modelled the transient heat flow occurring during the curing process and the resulting residual stress. These models provided some extremely valuable insights, but assumed that the adhesive flow had completely finished and that all of the assembly force is therefore carried by the conductive particles before resin curing commences.

Wu *et al.* [59] simulated the stress generation during the bonding process using FEM, it was reported that both for rigid and deformable particles, significant stress was built up at the interface between the two contacts, as shown in Figure 2.6. This offered a useful insight into the stress distribution around the conductive particle during the bonding process, but only a very simplified finite element analysis of a particle embedded in a bonding system was used, and the effect of the adhesive matrix on the mechanical response was neglected in this research.

Pinardi *et al.* [60] and Wu *et al.* [61] made a complete analysis of the effect of bump height on the stress and strain distribution in the ACA joints during the compression, cooling process and thermal cycling test. The results showed that the residual stress was larger on rigid substrates than on the flexible substrate after bonding. The thermal stress increased with the thickness of the bump, also large strains were found with thicker bump. In these two papers, the particle was considered as infinitely small and ignored in the research.

initiation and propagation. Moreover, the stress concentration was located at the edge area especially for the gold coating layer.

Some theoretical analysis was focused on the relationship between compression and the electrical conduction of ACAs. Williams *et al.* [63] analyzed the contact area and resulting contact resistance for a solid metal sphere on a yielding substrate and explored the effect of the conductor particles on the post assembly elastic properties of the adhesive. Williams *et al.* [64] then used this analysis to explore the effect of assembly pressure and contact particle size and density on conductivity. Yim *et al.* [65] presented analytical and FE based models of the contact resistance for both solid and polymer cored spheres and reported an increase in contact resistance due to over compression, particularly for polymer cored conductor particles. All of these studies assumed uniform compression of the adhesive, although Shi *et al.* [66] extended the analytical models of conductivity to include the size distribution of the particles, single particle conduction and multi particles conduction were both studied. Chin *et al.* [67] reviewed the existing approaches to predict the contact resistance of ACA assembly and the discrepancies among these models between the model prediction and experiments were highlighted. Määttänen *et al.* [68] calculated the particle resistance as a function of particle deformation degree using a conduction model for the metal coating polymer particle. It was found that the resistance was independent of the particle size, but depended on the resistivity of the particle, the thickness of metal layer and the degree of deformation as shown in Figure 2.9.

Dou *et al.* [69] further concluded that the greater the level of particle transformation, the thicker the metal coating layer and the greater the resin diameter, the lower the particle resistance was, according to the numerical analysis of the Ni/Au coated polymer particles. It showed that the ACF particle resistance was determined by the particle transformation and the particle geometries; however it was more sensitive to the transformation and the nickel layer thickness than the resin diameter and the gold layer thickness.

$$\frac{\partial C}{\partial t}=D\left(\frac{\partial^2 C}{\partial x^2}+\frac{\partial^2 C}{\partial y^2}+\frac{\partial^2 C}{\partial z^2}\right) \tag{2.6}$$

Where D is the coefficient of moisture diffusion, C is the moisture concentration.

When the temperature changes in an assembly which is made of more than one material, stresses build up due to the CTE mismatches in the materials. Similarly, when moisture absorption takes place in an ACF assembly, stresses also build up due to the mismatches in coefficient of moisture expansion (CME) or variations in moisture content. These are called hygroscopic stresses. Assuming that the mechanical, thermal, and moisture induced strains are independent of each other, then the mechanical strain is calculated as the total strain less the thermal strain and the hygro strain [12]. The calculation can be expressed as:

$$\varepsilon^{mechanical}=\varepsilon^{total}-\varepsilon^{thermal}-\varepsilon^{hygro} \tag{2.7}$$

According to the constitutive relations between the strain components and the corresponding stress components, for the thermal-hygro-elastic analysis, the stresses can be calculated as:

$$\sigma_{jk}=\lambda(\varepsilon_{11}+\varepsilon_{22}+\varepsilon_{33})\delta_{jk}+2G\varepsilon_{jk}-\frac{E}{1-2\mu}(\alpha\Delta T)\delta_{jk}-\frac{E}{1-2\mu}(\beta C)\delta_{jk} \tag{2.8}$$

Where μ and E are the Poisson's ratio and the Young's modulus respectively, β is the CME, α is the CTE, ΔT is the temperature change (thermal load), and C is the moisture concentration. λ and G are known as the Lamé constant and shear modulus which are directly related to the Young's modulus and Poisson's ratio:

$$\lambda=\frac{E\mu}{(1+\mu)(1-2\mu)}\ ,\quad G=\frac{E}{2(1+\mu)}$$

Wei *et al.* [11] studied the moisture diffusion and moisture induced stress inside an ACF assembly under 121°C, 100%RH, 2atm condition. A 3D transit moisture

2.3 Summary

A literature review has been presented in this Chapter. The recent research achievements in this area are summarized into two areas, computer modelling and experiments, in order to give a clear summary of state of the art. There are plenty of papers published in this research area so far and most of them are related to the reliability performance of ACA assemblies.

Although much work has been done, there are still some areas which are not fully understood and some questions still remain. One of the limitations of previous modelling research is mostly using the 2D models due to the difficulties caused by the multi-scale nature of the ACF package. In some cases, 3D models were built, but the structure of ACF joint was simplified. In this PhD research, a 3D macro-micro modelling technique is developed which enables a more detailed 3D modelling analysis of an ACF package than previously. By using this technique, the failure mechanism of an ACF flip chip on flex substrate in an autoclave test environment is studied.

The issue of SMT-compatibility is attracting more and more attention in the electronic industry. Having the mixed board technologies containing both ACFs and solders on the same substrate has a number of advantages. The challenge and concern for industry is the ability for the ACF materials to survive the high solder reflow temperatures. By using both computer modelling and experimental techniques, the effect of solder reflow temperature on the reliability performance of ACF assemblies are analyzed in this research and in particular, the impact of moving from tin-lead soldering to lead free soldering on this combined technology is demonstrated.

Chapter 3

Flip Chip Technology

In this Chapter, the flip chip technology used for IC packaging is introduced and compared with other traditional technologies such as wire bonding and tape automated bonding (TAB). The materials used for the flip chip interconnection, ranging from metal alloys to conductive adhesives are introduced and compared with each other. Finally, The concepts of reliability and failure analysis of electronic products are discussed and the applications of ACFs in LCDs and disc drives are presented.

3.1 Introduction

Microelectronics devices are the basis of all modern electronic products. Since the invention of the transistor in 1947, electronic products began shifting from vacuum tubes to transistors in the 1950s, and to ICs in the 1960s. The first IC which incorporated two transistors and a resistor was developed by Jack Kilby in 1959. Driven by the functional and performance requirements of modern and future electronics, continuous developments in reducing the size of the transistors are allowing the progressive integration of many transistors in a single semiconductor chip. Figure 3.1 illustrates the famous Moore's Law which predicts that every 18 months chip makers will double the number of transistors that can be crammed into a unit area of a silicon wafer. To date, developments in the semiconductor industry have been accurately predicted by this Law [1][2].

are that additional wafer processing steps are required for bumping and the packages size tends to increase with larger I/O counts.

3.2.3 Flip Chip

One of the significant developments to improve cost, reliability and productivity in the electronics packaging industry have been the advancement of flip chip technology which was firstly introduced for ceramic substrates by IBM in 1962 [73].

Flip chip interconnection is the connection of an IC to a carrier or substrate with the active face of the chip facing toward the substrate. Electrical connection is achieved through conductive bumps built on the surface of the chips and substrate pads. During the mounting, the chip is flipped onto the substrate or carrier with the bumps being precisely positioned on their target locations. In flip chip technology, the whole area of the chip can be used for connecting rather than just the periphery, so that more connections can be achieved on the same size chip compared with wire bonding and TAB.

The flip chip process using solders consists of four steps: forming the solder bumps, placement of the chip onto the substrate, reflow process to attach the bumped die to substrate, and completing the assembly with an adhesive underfill as illustrated in Figure 3.4. In the flip chip assembly process, underfill materials are applied to help meet the reliability requirements. They protect the bumps from moisture or other environmental chemicals, and provide additional mechanical strength to the assembly. Furthermore, the most important purpose to use underfill, particularly with solder bumps connections on large die onto organic substrates is to compensate for the thermal expansion differences between the chip and the substrate [74]. Since most of the low-cost substrates are plastics which have a large CTE (20-30 ppm/°C) compared to Silicon (about 3 ppm/°C). Such a CTE mismatch can generate a large shear strain in the solder balls. The underfill serves as a compliant buffer reducing the shear strain of the solder balls by coupling the thermal mismatch into bending of the substrate, resulting in a significant improvement of the fatigue life of the solder balls [76].

from a crystalline silicon wafer, the substrate materials can be flex, glass, ceramic, or organics such as FR4 etc. With the development of IC packaging technology, the materials to form the joints become versatile ranging from solder alloys to conductive adhesives.

3.3.1 Solder Alloys

There are two main kinds of metal alloys used in IC packaging including traditional tin-lead solder, and recently developed lead-free solder. The latter material is attracting more and more attention in the electronics packaging community due to the environmental concerns of using lead.

3.3.1.1 Tin-Lead Solder

Tin-lead solder (mostly Sn63/Pb37 or Sn60/Pb40) has been used as the interconnect material in the electronics packaging industry for more than 50 years. Up until now, it has been the main material used for the interconnection although a range of possible alternatives have been investigated. The function of the solder in the interconnection is to join two metal surfaces by alloying with their surfaces to achieve electrical conduction and mechanical support. Solder is always used with flux, the function of the flux is to remove the oxidized layer of the surfaces to be soldered and prohibit the metal from oxidation during the soldering process, and thereby improving the wetting ability of the solder alloy on the metal surfaces. There are many types of solder and flux, but both must be suited to the metals to be soldered together and to each other. One of the most popular tin-lead solders is Sn63/Pb37, which is called "eutectic," since it can pass directly from solid to liquid without a pasty stage and therefore can flow very easily. Most of the surface mount components are soldered with eutectic solders.

3.3.1.2 Lead-Free Solder

It is known that lead is a harmful metal to the environment. Lead and its compounds are ranked among the top 10 hazardous materials and it is also the number one environmental threat to children [77]. Environmental pressures are forcing changes on the world market for electrical and electronic products which will result in a dramatic reduction in the use and possible long term elimination of lead based solders. In Europe the Restriction of Hazardous Substrates (RoHs) Directive [78] has banned the use of lead from most consumer products from 1st July 2006. Recycling and reuse legislation such as the Waste from Electrical and Electronic Equipment (WEEE) Directive [79] and the End of Life Vehicles (ELV) Directive [80] will make it more difficult and expensive to use exempt materials.

The impending ban on lead requires more research on lead-free solders, and increasing attention within the semiconductor and electronics industry is focusing on lead-free solder manufacturing. Nowadays, the reliability performance of lead-free solders has been a major concern to the industry since the lead in the solder can help reduce the surface energy of tin-lead solder, increase the wet-ability on the metal, improve the ductility of the solder paste and decrease the brittleness. Therefore, once the lead is taken out of the solder, several problems arises, such as poor wet-ability, higher melting temperature, lack of long-term reliability data and both tin-whisker and tin-pest risks due to the higher tin content [81][82].

Particularly, the changing from lead to lead-free will have a very significant impact on the manufacturers of flexible circuit boards and many manufacturers who assemble them. Flexible circuits are a rapidly expanding sector of the electronics market with an increasingly wide range of applications. The problem results from the fact that flexible circuit boards are relatively sensitive to temperature due to their base material (polymers) e.g. continuous service temperature: polyimide about 177°C, polyester about 74°C, this make them a particular concern during the change from tin-lead solder (e.g. melting point 183°C) to the high melting point lead-free solders (e.g. melting point of Sn/Ag/Cu 217°C) with the resultant increase in processing temperature of 20°C to 50°C.

Although it is now widely agreed that there is no drop-in replacement for the standard Sn/Pb solders which are currently used worldwide, a range of possible alternatives have been investigated. Some consensus have developed for using one family of alloys based on tin, silver, and copper (SAC) alloys. These are mainly tin, typically 3%~3.5% silver and a small amount of copper with melting points around 210°C, which is about 30°C higher than that of traditional lead-containing counterparts. Other alloys under consideration are the tin-copper eutectic which has a lower material cost but higher melting point of 221°C. Also of interest for flexible circuits are lower melting point solders such as tin-silver-indium or tin-zinc, but the cost of indium and corrosive nature of zinc needs to be evaluated. A summary of the melting points of tin-lead solders and some lead-free solders are listed in Table 3.1. In general, the lead-free soldering is technologically possible, but many key issues have to be solved, both scientifically and industrially.

Table 3.1: Lead and Lead-free solder alloy under study [83]

Solder Alloys		
Composition	Solidus (°C)	Liquidus (°C)
62Sn36Pb2Ag (Sn62)	179	Eutectic
63Sn37Pb (Sn63)	183	Eutectic
Some Proposed Lead-Free Alloys		
86.9Sn10In3.1Ag	204	205
91.8Sn3.4Ag4.8Bi	211	213
96.2Sn2.5Ag0.8Cu0.5Sb	215	217
95.5Sn3.8Ag0.7Cu	217-218	Eutectic
95.5Sn3.9Ag0.6Cu	217-218	Eutectic
High Melting-Point Alloys		
95Pb5Sn	308	312
90Pb10Sn	275	302

3.3.2 Electrically Conductive Adhesives (ECAs)

Different kinds of adhesives have been used in electronics packaging for decades such as the hybrid, die-attach and display assembly. Besides traditional sealing, a growing interest has been observed within the electronics industry in other kind of functions, such as the interconnection material. The main advantages of using adhesives as the connection materials compared with traditional tin-lead solders include:

- Fine-pitch capability especially when using ACAs for flip-chips;
- Low temperature processing capability. The bonding temperature is much lower than the reflow peak temperature of the soldering process;
- Flexible and simple processing, and low cost.

Basically, there are two different types of ECAs used in electronic packaging: conductive adhesives and non-conductive adhesive. The conductive adhesives include anisotropic conductive adhesives, and isotropic conductive adhesives (ICAs) that have different electrically conductive functions. Each of these adhesives will be discussed in the following sections and in particular the application of these materials in LCD assemblies will be introduced.

3.3.2.1 Isotropic Conductive Adhesives (ICAs)

Isotropic conductive adhesives are typically thermosetting polymers filled with conductive particles. The most common material system is epoxy filled with silver flake particles. They become conductive in all directions upon curing, yielding an electrically functional interconnection. ICAs are applied in the same way as conventional solder paste, but cured rather than reflowed. There is no self alignment effect during the curing since the adhesive does not have the high surface tension as solder alloy. Therefore, component placement requires more accuracy than with solders. The amount of ICA used should be less than the solder paste to prevent bridging effect. A typical structure of an ICA flip chip is shown in Figure 3.5a.

ICAs have been evaluated as potential replacements for lead-containing solders. These adhesives are being used to some extent in LCD applications due to the low processing temperature. However, there is not much work reported that tries to establish a fine pitch ICA flip chip technology, and up until now the use of ICA for flip chip is limited mainly to the assemblies of large contact area components such as chip capacitors and resistors [83]. ICAs are normally screen or stencil printed onto the circuit pads in order to obtain isolation between the adjacent pads. For fine pitch applications, this process is limited for two reasons. Firstly, printing paste at fine pitches is difficult without applying so much adhesive that shorts adjacent traces during assembly. Secondly, the small amount of adhesive deposited on the contact pads, coupled with the very high conductive filler content, lowers the adhesive bond strength.

3.3.2.2 Anisotropic Conductive Adhesives (ACAs)

In the last few years, another type of adhesive that is conductive in one direction only has attracted more and more attention. These are referred to as anisotropic conductive adhesives which can be obtained either in films or pastes. Conventional ACA is an adhesive consisting of conductive particles dispersed in an adhesive matrix. These particles can be pure metals such as gold, silver, or nickel, or metal-coated particles with plastic or glass cores. The volume fraction of particles is well below the percolation threshold with the particles typically ranging from 3-15μm in diameter. ACAs provide electrical as well as mechanical interconnections between conductive pads on parts to be assembled. The conductivity of these materials is restricted to the vertical direction (perpendicular to the plane of the board) with electrical isolation provided in the plane direction. Due to the anisotropic conduction, ACA can be deposited over the entire contact region, and thus significantly facilitates the material application. The low conductive filler content can also improve the adhesive bond strength to help achieve the robust interconnects. The most significant advantages of using ACAs are the capability of fine pitch connections and low processing temperature; interconnections with pitches of 100μm or less have been demonstrated with these materials [84][85]. A typical ACA connection is shown in Figure 3.5 b.

The use of ACAs in LCD products has stimulated significant interest since the last decade. The low processing temperature of ACA is one of the primary reasons for its widespread use for LCD drive attachment. In addition, it is supporting a fine pitch attachment process due to the lack of solder bridging or smearing of conductive adhesive. Using an ACA simplifies the mounting process, as there is no need for precise placement of the adhesive, and it is lead-free. However, the danger for damaging the ITO contact pads is particular concern when using chips with hard electroless nickel/gold (Ni/Au) bumps during the thermo-compression [84].

3.3.2.3 Non Conductive Adhesives (NCAs)

The function of non-conductive adhesives is to provide a mechanical connection between the bumps on the chip and corresponding pads on the substrate. This mechanical connection provides the needed conductive paths. Instead of introducing new conductive particles into the system, the NCA bonding method relies upon direct electrical contact between the two conductor surfaces as illustrated in Figure 3.5c. With mechanical pressure, a "metal to metal" contact is created and the contact points are responsible for the transport of electrical current. The epoxy filled cavities supply the adhesive forces which are needed to keep the materials together. Once the connections are made, the shrinkage force in the cured adhesive is responsible for the compressive force which is needed to maintain the electrical contacts.

Conductive joining with NCAs provides a number of advantages compared with ICA or ACA technologies. NCA joints avoid short-circuiting and they are not limited by particle size or distributions. Further advantages are cost effectiveness of the adhesives and ease of processing. However, the reliability and failure mechanisms of NCA joints are still not well understood; when two nominally flat surfaces are forced into contact, they meet only in a limited number of small areas, and the co-planarity of the metallization will affect the connection quality significantly. There are a few papers [88][89][90] that have studied the reliability performance of NCA under different testing conditions.

3.4 Reliability Testing

ACAs are becoming promising interconnection materials in electronics packaging and even thought of as one of the best alternatives to the traditional tin-lead solders in the future. However, the main challenge with ACA materials is reliability. As a result, more and more research activities are involved in this area , dedicated to improving the reliability performance of ACA components under variable testing conditions such as thermal cycling, and temperature/humidity test.

3.4.1 Reliability and Failure

The term reliability is defined as the ability that an item can perform its intended function for a specified interval under stated conditions [92]. In classical reliability, a single product, unit or component is generally considered to have two states, operational and failed. A failure occurs when an item does not perform a required function. The idealized bathtub curve is shown in Figure 3.6, which represents three phases of product hazard rates.

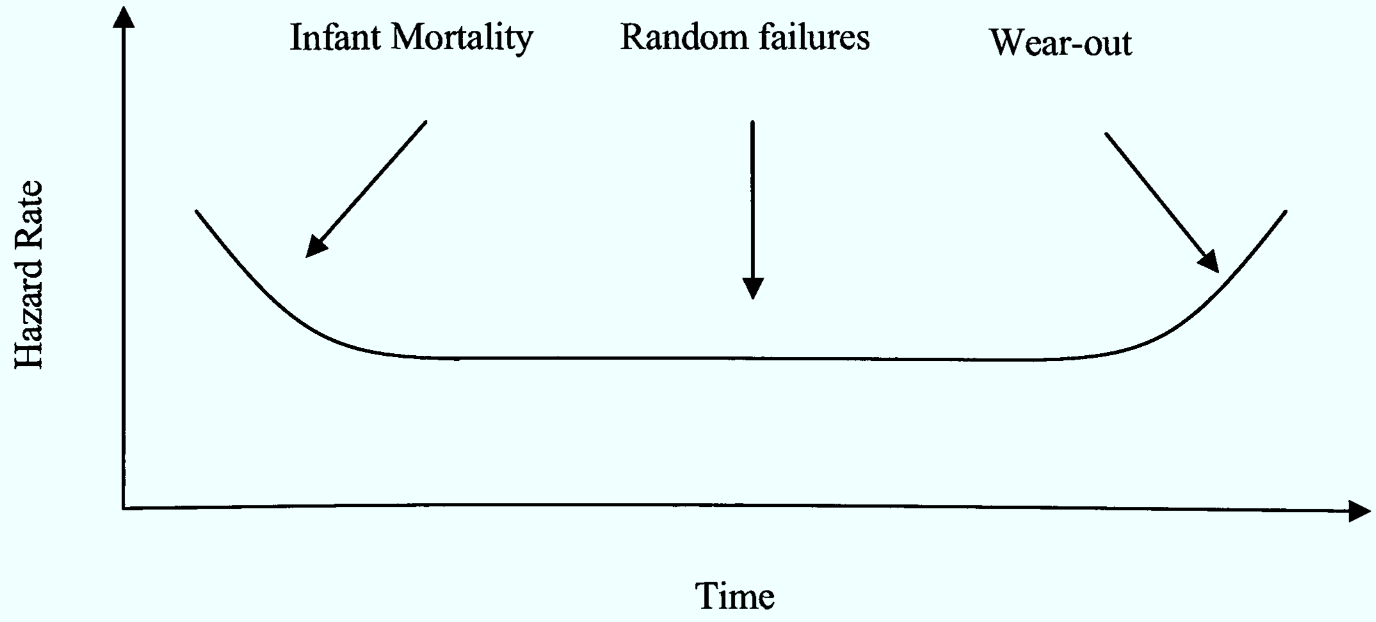

Figure 3.6: Idealize bathtub curve

The first phase, often called "infant mortality" represents the early life of the product when manufacturing imperfections or other initial failure mechanisms may appear. The hazard rate decreases during this time as the product becomes less likely to experience failure from one of these mechanisms. The second phase, sometimes called "useful life" represents the majority of the product operating time. During this period, the hazard rate of the product appears to be constant (constant failure rate). The third phase, often called "wear-out" occurs near the end of the expected product life and often involves failure mechanisms caused by cumulative damage. Electronic components are subject to wear-out due to electro-migration, material degradation and other mechanisms. Weibull, lognormal or other statistical distributions can be used to describe hazard rates during both infant mortality and wear-out.

3.4.2 Reliability Test and Standard

Reliability prediction can be carried out based on test data, stress and damage models or reliability handbook. Reliability tests can be divided into non-accelerated test and accelerated test which are introduced in the following sections.

3.4.2.1 Non-Accelerated Test

The traditional approach to reliability evaluation involves tests carried out within the products 'expected environment' or using actual operational conditions. In these tests, there is no attempt to relate the test temperature, humidity, voltage or other environmental stimulus to an additional test level that will increase the hazard rate, thereby reducing the test time. When analyzing test data, it is important to determine a distribution that provides a good fit to the data and is representative of the failure mechanism type. A good fit is important so that the distribution parameters can be used to extrapolate behaviour, or predict the reliability beyond the period over which the data is generated. There are two kinds of non-accelerated tests which are used to predict the data for reliability analysis, manufacturing tests and actual tests.

3.4.2.2 Accelerated Test

The purpose of accelerated testing is to verify the life-cycle reliability of the product within a short period. Thus, the goal in accelerated testing is to accelerate the damage accumulation rate for relevant wear-out failure mechanisms. There are two common forms of accelerated life testing, which are (1) eliminating "dead time" by compressing the duty cycle and (2) reducing the time-to-failure by increasing the stress levels beyond what is expected in the life-cycle. The latter can be run by enhancing a variety of loads such as thermal loads (e.g. temperature, temperature cycling, and rates of temperature change), chemical loads (e.g. humidity, corrosive chemicals like acids and salt) electrical loads (e.g. steady-state or transient voltage, current, power) and mechanical loads (mechanical deformation, vibration and shock/impact).

In the electronic industry, when life cycle reliability testing is the primary purpose, test types such as Highly Accelerated Stress Testing (HAST), Highly Accelerated Stress Screening (HASS), Highly Accelerated Life Testing (HALT) are specified. The test procedures are normally carried out according to the standards of Electronic Industries Association (EIA) [93], Joint Electronic Device Engineering Council (JEDEC) [94] and various Military Standards test handbook.

HAST also stands for "Highly Accelerated Temperature/Humidity Stress Test". It was developed as a shorter alternative to Temperature Humidity Bias (THB) testing in which 85°C/85%RH condition is always used. If THB testing takes 1000 hours to complete, HAST results are available within 96~100 hours. Because of this, the popularity of HAST has continuously increased in recent years. HAST test which is also known as the autoclave or pressure cooker test (PCT) uses a high temperature over 100°C, high relative humidity (RH) about 85%, under high atmospheric pressure conditions (up to 4atm).

3.4.3 Failure Models

In many cases, the stress and damage models are combined to form a single model which is referred to as a failure model. Examples of conditions that are known to induce failures include, but are not limited to, a temperature cycle, a sustained temperature exposure, a repetitive dynamic mechanical load, a sustained electrical bias, a sustained humidity exposure, and an exposure to ionic contamination. Examples of damage include exceeding a material strength, reduction in material strength, removal of material, change in material properties, and growth of a conductive path or separation of joined conductors [92].

Failure models may be classified as overstress and wear-out. Models for overstress calculate whether failure occurs based on a single exposure to a defined stress condition. For an overstress model, the simplest formulation is comparison of an induced stress versus the strength of the material. Die fracture, pop-corning, seal fracture, and electrical overstress are examples of overstress failures. Models for wear-out failures calculate an exposure time required to induce failure based on a defined stress condition. Fatigue, crack growth, creep rupture, metallization corrosion and electro-migration are examples of wear-out mechanisms. In the case of wear-out failures, damage is accumulated over a period until the item is no longer able to withstand the applied load. Therefore, an approximate method combining multiple conditions must be determined for assessing the time to failure.

3.5 Applications of ACF Flip Chips

Typically, flip chip on flex (FCOF) using ACF is being used in the flat display, smart card and disk drive etc. As examples, the applications of ACF flip chips in LCDs and disk drives are introduced in the following sections.

3.5.3 Limitations for Further Applications

Currently, the devices assembled using ACAs are widely used in applications where the fine pitch connection or low processing temperature are required which can not be fulfilled by the traditional soldering. However, the application of ACAs is still limited in some specific areas. The limitations for the further applications are summarized below.

(1) Lack of reliability data: ACA is a new material compared to the traditional tin-lead solders, the reliability data is not well known and the failure mechanisms not well understood, especially in high humidity environments.

(2) Today, tin-lead solders are still the main connection materials used in the electronic industry; the facilities used for tin-lead soldering can also be used for lead free soldering. However, these facilities can not be used to assemble ACA components since the procedures of the two technologies, ACAs and soldering, are completely different.

(3) During the bonding process, the adhesive does not have the self-alignment capability as solders. Therefore, there is higher requirement for alignment accuracy when working with ACAs than working with solders. Also, ACA joints are formed under mechanical forces, the connections between the particles and metal pads are not as strong as the solder joints which are formed under physical, chemical reactions.

(4) The compatibility of the ACA assembly process with traditional soldering technology. The bonding temperature of ACAs is much lower than the peak reflow temperature. Therefore, there is a reliability issue when the ACA assemblies pass through the solder reflow process.

Any research that generates the reliability data or helps understand the above issues is deeply welcomed by the electronics packaging industry. It is also the main motivation for this research.

Currently, ACA is gaining wide acceptance among Asian end-users and semiconductor packaging houses. Its relatively slower acceptance in the United States and Europe may reflect Asia's 30 years of favourable experience with ACA in displays [98]. However, the packaging and cost advantages of ACA cannot be long ignored. Particularly in the hypercompetitive semiconductor arena, where cost, functionality, and reliability are being driven to new levels, ACA represents a bright future for middle and high-end manufacturing. As I/O counts become higher, more and more IC designers and users may find that fine-pitch, small-package, high-reliability ACA is their best choice.

3.6 Summary

In this Chapter, flip chip technology which is now popular within the electronics packaging is introduced and compared with traditional wire bonding and TAB technologies. The connection materials used in flip chips ranging from the solder alloys to conductive adhesives are presented.

To date, tin-lead solders are still the main connection materials used in flip chips due to the available long term reliability data and facilities. However, the harmful effect of the lead on the environment is becoming a serious concern for the industry and customer. The lead-free solders and electrically conductive adhesives are being investigated as the possible alternatives to traditional tin-lead solders. The study on the lead-free solders is extensive since the facility for the tin-lead solders can also be used for lead-free solders and the soldering technology is so mature. However, the wide application of lead-free soldering is still limited due to some difficulties which are caused by taking the lead out of the solder alloy that includes the poor wetting performance and high reflow temperature.

Conductive adhesives are being popularly used in the electronic industry especially in fine pitch and low temperature applications where the tin-lead solders are limited to fulfil the requirements. Among them, ACAs are the most popular ones used in flip chips currently since they have potential for fine pitch connections due to the anisotropy in electrical conduction. However, the reliability performance and the compatibility with soldering technologies are the major concerns with ACA assemblies which will be addressed in the following Chapters 4, 5 and 6.

Chapter 4

Reliability of ACFs for Flip Chip on Flex Applications: An Experimental Study

This Chapter details the experimental work undertaken to complement the modelling efforts. Data was gathered on both the assembly process and reliability testing for ACF materials. The effect of bonding parameters on the electrical performance of ACF assemblies was studied. ACF components were also subjected to a solder reflow profile, this is important to characterise the behaviour of these ACF bonds to subsequent surface mount assembly for other solder joint components on the same board.

For reliability testing, the assembled ACF components were subjected to humidity and temperature environments. An autoclave test at 121°C, 100%RH and 2atm condition was used. Two sets of samples, with and without reflow treatment, were tested in order to examine the effect of solder reflow on the reliability performance of ACF assemblies.

4.1 Introduction

Soldering as a mature joining method has been used for many years in electronics packaging. It is the lowest temperature metallurgical joining method used with metals and plastic materials [6]. For many years, the reliability of solder joints has been

ability of the ACF materials to survive the high solder reflow temperatures which are much higher than the temperature required to bond and cure the ACF material [20][45].

Although the ability of ACF to withstand multiple solder reflows is considered as the major milestone in its acceptance within the semiconductor packaging industry [98], there has been very little research undertaken in this area. The work presented here was one of the first studies in this area.

Compared with the traditional solder assembly process, the ACF assembly process is simplified since there is no need to use flux, stencil printing and a reflow oven. However, the selection of the bonding parameters is crucial and the following issues must be addressed in any ACF bonding process:

(1) Sufficient conductive particles must be trapped between the pads on the substrate and the die. This is to guarantee enough electrical contact with both conductor surfaces. Care must be taken to ensure that not too many particles are present as this can lead to short circuiting between adjacent pads.

(2) For the ACFs made with metal coated polymer particles, the amount that the particle deforms is important. The bonding process determines the contact area between the conducting particle and the die/substrate pads. This is important as a smaller area leads to greater contact resistance.

(3) The curing degree of the adhesive and the residual stress state after assembly can significantly influence the reliability of the ACF interconnections under hash testing conditions.

Therefore, the combination of the bonding parameters needs to be designed to achieve the best performance of the adhesive joints where the optimum deformation of the conductive particles and the proper curing degree of the adhesive matrix are achieved.

4.2 Experimental Design

Figure 4.2 illustrates the process undertaken in the experimental work which consists of the following four steps:

(1) The chips were first bonded to the substrate using ACFs and after this the joint resistance was measured.

(2) Some of the bonded samples were passed through a solder reflow oven and the joint resistance was again measured.

(3) Two sets of samples, with and without reflow treatment, were put into a pressure cooker for reliability analysis.

(4) Finally failure analysis was conducted to find out the root cause of the failures and the measured increases in joint resistance.

Using the above methodology allowed us to investigate the effects of (a) bonding parameters, (b) solder reflow temperature and (c) moisture absorption on the reliability performance of ACF materials and assemblies.

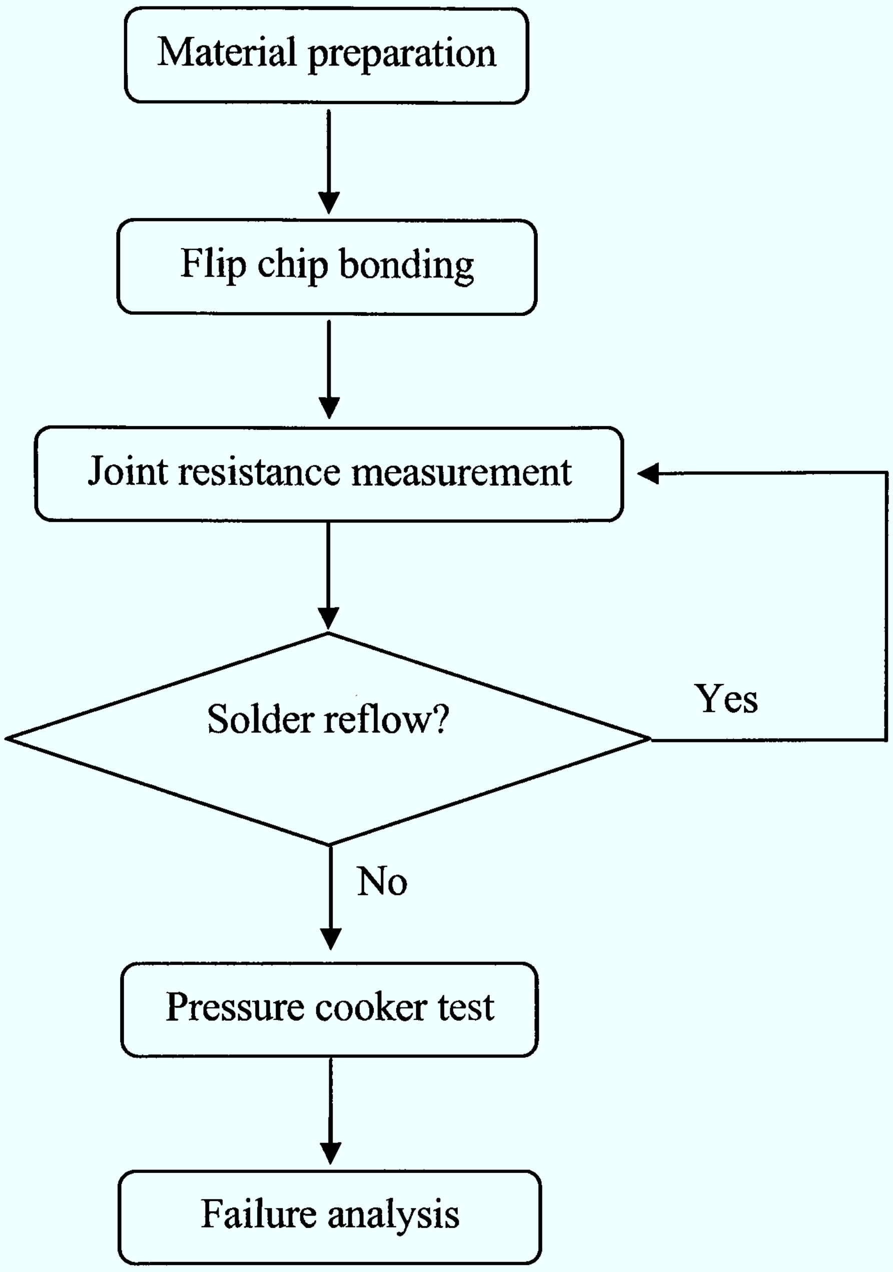
Material preparation
Flip chip bonding
Joint resistance measurement
Solder reflow?
Yes
No
Pressure cooker test
Failure analysis

Figure 4.2: The flow chart of the experimental procedure

4.2.1 Materials

Three materials were used in these experiments. These are the silicon die, polyimide substrate, and a commercial ACF. The specifications of each material are available and detailed in the following sections.

the capability for fine pitch interconnections. The detailed specifications provided by the manufacturer are summarised in Table 4.1.

Table 4.1: Specification of the ACF used in this experiment

Description	
Thickness (μm)	35
Structure	Single layer with particles
Conductive particle	Ni/Au coated resin ball
Insulating layer	Yes
Particle diameter (μm)	3.5
Tg (°C)	131
Density of conductive particles	3.5 million/mm^3

The conductive particles are polymer balls with Ni/Au coating. The structure of the ACF material and the particles are shown in Figure 4.5. ACFs are normally stored at low temperature, and subjected to ambient temperature several hours prior to the bonding process.

The recommended bonding conditions were provided by the supplier. However, bonding conditions differ depending on the chip size and bump pattern. A detailed experimental design was therefore established to investigate the best bonding conditions for new ACF applications. The parameters investigated were (a) bonding pressure, (b) bonding temperature and (c) bonding time. These are listed in Table 4.2.

4.2.2 Flip Chip Bonding Process

The assembly process using ACFs consists of three steps: (1) Pre bonding, (2) Alignment and (3) Final bonding. The flip chip bonding process using the ACFs made with metal coated polymer particles is illustrated in Figure 4.6.

(1) Pre bonding: The transparent layer on the surface of the supplied ACF is removed and the ACF is laminated onto the surface of the substrate. Then a pressure of 0.18MPa is applied over the bonding area for a few seconds at 90°C. The separator layer is then removed.

(2) Alignment: The chip is then aligned to the substrate by using the marks on the chip and substrate. Since the ACF is mainly used for fine pitch applications, there is always significant requirement for alignment accuracy.

(3) Final bonding: Heat and pressure are now applied at the back side of the chip which cures the ACF. Before cure takes place the ACF material is soft and can flow between the bond pads allowing the conductive particles to move and distribute evenly throughout the ACF joints. When the curing process is completed, the ACF becomes hard. The deformed particles are then trapped between the pads and this creates the anisotropic electrical contact between the chip and the substrate.

4.3.1 Bonding Conditions

Different bonding parameters were used. Twelve sets of ACF assemblies were bonded in order to compare the joint resistance. The baseline bonding parameters were Bonding Temperature (200°C), Bonding Pressure (86.2MPa) and Bonding Time (10s). The subsequent solder reflow profile used for the tin-lead solder had a peak temperature of 210°C.

4.3.1.1 Bonding Pressure

Figure 4.11 details the average results from twelve assemblies analysed for joint resistance and bonding pressure. The vertical bars showing the standard deviation of the results for each bonding pressure value. In these experiments, the bonding temperature and bonding time were kept constant at 200°C and 10s respectively.

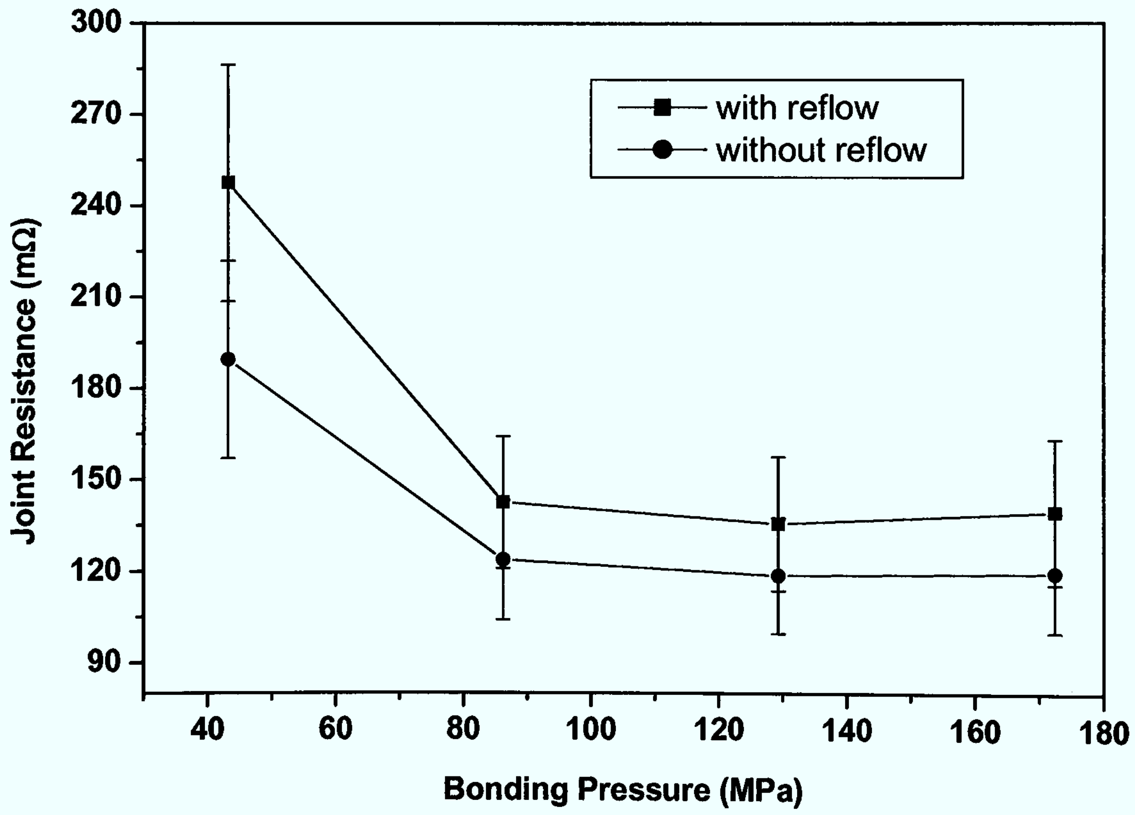

Figure 4.11: Variation of joint resistance with bonding pressure

For the samples without the reflow treatment, the mean values of the joint resistances decreased as the bonding pressure increased from 43.1 to 86.5MPa. After this the joint resistance remained constant around 120mΩ. A possible explanation for this is that the small bonding pressure could not deform the particle and the contact area was too small to achieve a lower contact resistance. Compared to these as-bonded samples, the joint resistance of the samples that have passed through a reflow process were higher. However, the tendency of the profile of the joint resistance versus bonding pressure was similar in each experiment, with or without reflow process.

After the reflow process, the mean values of the joint resistances of Chip on Flex (COF) assemblies increased by 20 to 60mΩ compared with the corresponding non-reflowed ones. The joint resistance was particularly higher for the samples bonded at lower or higher pressures.

Deformation of the conducting particles is held by the shrinkage forces in the adhesive matrix. Therefore, during the reflow process the expansion of the adhesive may cause a reduction of the holding force and thus reduced the contact area between the conductive particles and metal pads as the assembly heats up. Contact resistance increased the most when the using the lowest bonding pressure, 43.1Mpa. When using a high bonding pressure the contact resistance change after the reflow process was not as severe. This is probably due to the fact that these over deformed particles were firmly held by the cured adhesive. However the worse reliability performance may be expected in this case as there is a high probability that some of the particles could be crushed during the bonding process.

The big error bars, shown in Figure 4.11, when the ACF is bonded at 43.1Mpa, also indicate that the electrical performance of these samples was not as stable as when the sample was bonded at higher pressures. It is also noticed that the stability of the electrical contact in the reflowed samples was reduced compared to the corresponding non-reflowed ones.

In order to prove the effect of the bonding pressure, optical photos were taken on samples using transparent glass substrates as the bonding medium. Figure 4.12a shows the ACF joints bonded at lower bonding pressure. The particles captured between the

bumps and the pads, hence, the contact areas between the particles and the bump/pad are not big enough for stable conduction resulting in higher contact resistances.

After the reflow treatment, the joint resistances increased by 10mΩ to 60mΩ compared to the corresponding as-bonded samples. The trends between the joint resistances versus the bonding temperature of the COF samples with and without reflow process are similar. It is noticed that the increase of the resistances due to the reflow treatment was higher for the samples bonded at lower or higher temperature. This indicates that by using the proper bonding temperature the effect of subsequent high temperature reflow process could be reduced. The error bars, in Figure 4.13, from the samples bonded at the 140°C and 220°C temperature are bigger than the other bonding temperature. This illustrates that the electrical performance of these samples were not as stable as the samples bonded at temperatures of 160°C, 180°C and 200°C.

4.3.1.3 Bonding Time

Figure 4.14 shows the relationship between the joint resistance and bonding time at constant bonding temperature (200°C) and bonding pressure (86.2MPa). The results show the mean value of the joint resistance, with the error bars indicating one standard deviation variation.

When the bonding time was less than 10s, the mean joint resistance of COF samples decreased as the bonding time was reduced. For the COF samples with reflow treatment, the similar curve was obtained except an averaged increase of 20mΩ to 30mΩ in joint resistance. It is suggested that sufficient bonding time is required to achieve the good electrical performance of ACF joints since the adhesive may not be cured properly in a short time bonding. The electrical contact in the reflowed ACF joints are not as stable as the corresponding non-reflowed ones which is reflected by the length of the error bars.

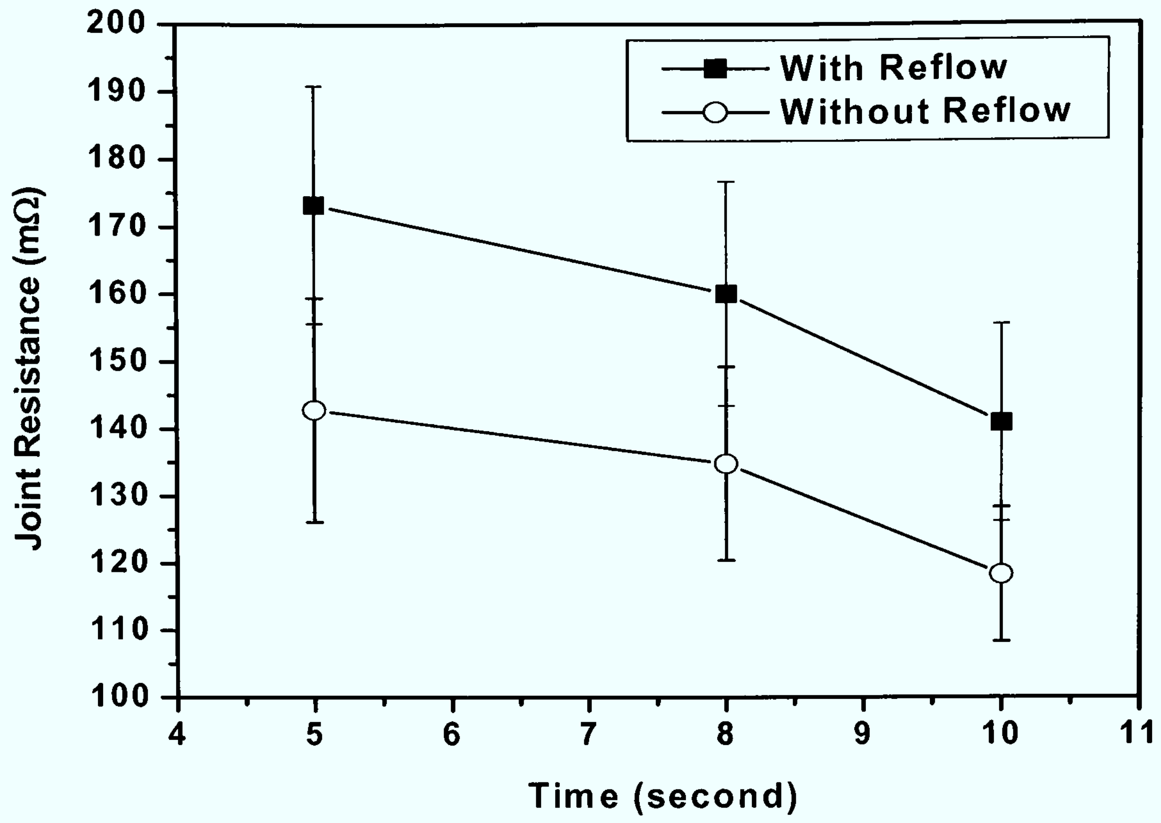

Figure 4.14: Variation of joint resistance with bonding time

4.3.2 DSC Test Results

For the epoxy based ACFs, when the temperature increases, the ACF melts and transforms into a low viscosity liquid. It then cross-links to form the three dimensional crystallized structure which contributes to its stable physical properties [48]. The density of the cross-linkage can be indicated by the degree of adhesive cure that has taken place. This degree of cure plays an important role in determining the reliability performance of the final ACA joints. A minimum cure degree is required to provide a certain level of mechanical and electrical performance. When the material is not fully cured it will be too soft to restrain the conductive particles in place and hence these particles may easily loose contact with the metal pads.

The degree of cure in a conductive adhesive can be examined by using a Fourier Transform Infrared Spectrophotometer (FTIR) or Differential Scanning Calorimeter (DSC) [37][92][95]. In these publications it was shown that the degree of cure in the ACA joints was very dependent on bonding temperature.

In this research, the degree of cure in the ACF was examined using a Modulated DSC instrument (by TA Instruments, Model 2910). Both the heat capacity of endothermic and the exothermic transitions were measured for a particular test sample. This provides quantitative information regarding the enthalpic changes during the cure process.

Three kinds of samples were prepared for the DSC test, including:

(1) Raw ACF: In this case the ACF material was not cured or sent through a subsequent reflow process

(2) Cured ACF: In this case the ACF material was cured at the bonding temperature of 200°C for 10 seconds.

(3) Cured and Reflowed ACF: In this case the ACF was cured at the bonding temperature of 200°C for 10 seconds and then subjected to a tin-lead solder reflow process.

For the cured samples detailed in (2) and (3) above, these were prepared as follows: firstly, the ACF material was placed onto a glass substrate and then the cover film was peeled off. After the pre-bonding process (where the assembly ws subjected to 100°C temperature), the separator layer was peeled off. Then an aluminium foil was put on the surface of the ACF to avoid adhesion of ACF with the flip-chip bonding head. This glass/ACF/Aluminium-film assembly is then subjected to the usual cure temperature process with the parameters of bonding temperature, pressure and time as detailed above. Sample (3) above, was then subjected to a lead-based solder reflow process which had a peak temperature of 210°C. Before the DSC test, the aluminium foil was taken off the ACF carefully, and then the ACF was peeled off the glass substrate to provide the samples for the DSC tests.

After each test, some of the samples were cross sectioned and then examined using a Scanning Electron Microscope (SEM) in order to analyse the root cause of any measured increase in contact resistance that would be due to delamination type failures.

The flip chip on flex samples used in this reliability test were bonded at 200°C, 86.2MPa for 10 seconds. Both assemblies, with and without a subsequent reflow profile, were tested. For the assemblies without a reflow treatment, results were obtained at 24, 48, 96 and 168 hours of the reliability test. For the assemblies with a reflow treatment, the results were only obtained at 24 hours after the start of the test.

4.3.3.1 Joint Resistances and Failure Rate

The joint resistances of the ACF joints were measured at 0, 24, 48, 96 and 168 hours during the test. Any joint that exhibited greater than 100% increase in joint resistance (over the time zero value) was considered to have failed. As illustrated in Figure 4.17 more than 85% of ACF joints were assessed to be failed in the first 24 hours of the test. This was for the assemblies that had not been subjected to a subsequent reflow profile.

However, visualising the joints using SEM showed that there were no open joints present after 24 hours of testing. An open joint is seen through clear delamination between the particle and the pad. 25% of the ACF joints were found to be open after 168 hours of testing.

The actual changes to the joint resistance during the autoclave test are plotted in Figure 4.18. The joint resistance increased slightly in the first 24 hours, where it doubled its value. After this it increased much further, especially over the next 72 hours. This is probably due to a number of open joints forming during this period.

4.3.3.2 Scanning Electron Microscope (SEM) Photos

Conventional optical microscopes use a series of glass lenses to bend light waves and create a magnified image, a SEM creates the magnified image by using electrons instead of light waves. Therefore, a SEM shows very detailed three dimensional images at much higher magnification than what is possible with an optical microscope. The SEM used in this research was the Philips Model XL40. The resolution of this machine is 2.5nm at 30kV and 5nm at 1kV.

Sample preparation for SEM analysis consisted of the following three steps:

(1) Epoxy Moulding: The ACF samples were firstly cut into small size and put into a mould which was then filled with epoxy adhesive and then the mould was left for several hours until the adhesive solidified.

(2) Grinding and Polishing: The moulded sample was then ground to remove material to expose the face of the sample that we wish to visualise. Care needs to be taken in this process to ensure that not too much material is removed and loose the features of interest. Once the interested surface was captured, the surface was then polished using micro powders to remove any rough surface characteristics.

(3) Gold Coating: Since SEM illuminates the surface with electrons, the sample must be able to conduct electricity. To achieve this, the sample surface was coated with a very thin layer of gold using a sputter coating machine. Finally, the samples were mounted onto a plug using a conductive tape and ready for the SEM analysis.

Figure 4.19 shows the SEM photos of an ACF joint after bonding (without reflow) and the ACF joint which had subsequently undergone 48 hours of autoclave test. Figure 4.19a, illustrates the state of the conductive particle before being subjected to an autoclave test. Clearly the particle was captured between the bump and the pad and had deformed showing good contact with the pad. However, after 48 hours pressure

cooker test, a delamination gap between the conductive particles and the metallization was clearly visible as shown in Figure 4.19b. The formation of this gap signalled a loss of the contact area and this will lead to an increase in contact resistance. Moreover, the cracks can be also seen along the interface between the adhesive and the flex substrate, and the interface between the flex and the substrate pad. The propagation of these cracks may eventually cause the total failure of the ACF joints.

In general, there are two possible causes for the increase of the contact resistances in ACF joints that have undergone the autoclave tests: debonding at ACA joints and corrosion of the metallization. Both can reduce the contact areas between the conductive particles and the metallization [9].

For the samples used in this study, the metal pads were plated with a gold layer so that the effect of electrochemical corrosion was negligible. If corrosion is negligible then the dominant mechanisms resulting in an increase in contact resistance is the loss of contact area between the particle and the pad. Moisture through hygro-swelling will enhance this process. Moreover, it not only diffuses into the adhesive layer, but it can also penetrate into the interfaces between the adhesive and the substrate/chip resulting in a reduction of the adhesion strength and even the formation of micro-cracks [9][110].

Epoxy has relatively low surface tension energy compared to Au, SiO_2 and many other materials, therefore good adhesion is usually expected when it applied to the surface of these materials [5]. However, the adhesion strength at the interface between the epoxy adhesive and the polyimide substrate is not as strong as others in this assembly due to the similar surface tension energy values of these two materials. Therefore, the interface between the adhesive and the flex is more vulnerable to water molecule attacks, and once the degradation at the adhesive/flex interface has started, water can move along the interface. When combined with the stress due to the swelling effect of the adhesive, this may cause further degradation of the interfaces.

Furthermore, high degrees of interfacial degradation in the adhesive joints can result in the presence of high water activity.

Computer modelling analysis will help provide a better understanding of the failure mechanism of ACF joint in this humid environment, these modelling results will be presented in Chapter 6.

4.3.3.3 Effect of Solder Reflow

Four samples subjected to the tin-lead solder reflow were tested for 24 hours at the autoclave test conditions stated above. The joint resistance of each ACF joint was then measured and the SEM photos were taken to show the failure information, the results were also compared with samples without reflow treatment.

The joint resistance results are shown in Table 4.3. These compare both the "as bonded" samples, i.e. not subjected to a reflow process with bonded samples that have been subjected to a reflow process. It is interesting to note that samples that were subjected to a reflow treatment show a large increase in the contact resistance and therefore will have poor reliability performance.

Table 4.3: The results to show the reflow effect

	Joint resistance (mΩ)		Open joints	
	Autoclave test (hour)		Autoclave test (hour)	
	0	24	0	24
As bonded	69.29±20.1	128.62±32.1	0	0
With reflow treatment	90.54±30.2	700.95±67.6	0	6%

For the samples without the reflow treatment, there were no open joints visualised after the 24 hours autoclave test. Only micro-cracks were detected along the interface between the adhesive and the flex as shown in Figure 4. 20a. For the samples with

According to other studies [99][100] on the water absorption and diffusion in epoxy-resin systems, moisture uptake increases with the cross-linking density (curing degree). This is because the cross linked region has a bigger free volume that can accommodate more water. This suggests that after the solder reflow process, more moisture absorption may take place with the fully (or even over)-cured ACF. Furthermore, during the solder reflow the thermal stresses inside the package due to the CTE mismatch could reduce the contact area between the conductive particles and the metallization. This may explain why the reflowed ACF joints showed worse reliability in the autoclave test.

4.4 Conclusions

This Chapter has described the flip chip bonding process using Ni/Au-coated polymer-filled ACFs and studied the effects of (1) bonding parameters, (2) solder reflow and (3) moisture absorption on the electrical/reliability performance of ACF flip chip assemblies.

The results showed that the joint resistances of ACF joints were highly dependent on the bonding parameters such as Bonding Temperature, Bonding Pressure and Bonding Time. These strongly affected the magnitude of deformation of the conductive particles and also the degree of cure in the adhesive. The quality of the final joint, as monitored through the joint resistance, was strongly influenced by all three variables and care was required to ensure that the correct combination of parameters was used.

The subsequent solder reflow treatment always causes an increase in the joint resistance. The magnitude of this increase was governed by the parameters used in the bonding process and the state of deformation of the particles and the degree of cure in the surrounding polymer matrix.

During the autoclave test, the joint resistance of the ACF joints increased. More than 85% of the ACF joints were assessed to have failed within the first 24 hours based on the failure criteria being a 100% increase in the joint resistance. However, open joints were not observed until after 48 hours of testing. The formation of delamination cracks between the conductive particles and the metallization was observed at this time. It is believed that this de-bonding process is due to absorption of moisture at the interfaces of the materials. This was the major cause of ACF failure.

Samples that had been subjected to a reflow process failed earlier in the autoclave test. This could be due to the greater degree of absorption in the reflow samples where the degree of cross linking in the polymer material was greater. The work outlined in this Chapter has contributed to one journal paper [126], and a number of international conference papers [129][133][136].

Chapter 5

Modelling of the Effect of Solder Reflow on ACF Performance

Experimental studies in Chapter 4 revealed that the solder reflow process had a substantial effect on the electrical and reliability performance of ACF flip chip assemblies. The change from tin-lead solder to lead-free solder results in an extra 20-50°C increase in the reflow peak temperature. This could damage the flip-chip assembly and the ACF materials. In this Chapter, the performance of ACF assemblies is further studied using computer modelling techniques. A parametric analysis investigates the impact of adhesive material properties (CTE and Young's modulus) and geometrical height of the bump (or pad on the silicon die). This analysis shows that the CTE of the adhesive matrix is proved the most important design variable in minimising the damage in the assembly when subjected to higher reflow temperatures. These modelling results are compared with the experimental findings in Chapter 4.

5.1 Computational Modelling

The software package PHYSICA was employed to investigate the primary cause of the failures observed in the experiments. This work focused on modelling the thermally induced stress in the ACF joints as they passed through the solder reflow process.

particle are accounted for by assuming a lower Young's modulus but a higher initial yield strength than that of the bulk material [54]. For example, the yield strength of the gold coating layer is assumed to be 190Mpa.

Table 5.1: Material characteristics used for this simulation

Material	Young's modulus (MPa)	Poisson's ratio	CTE (ppm/K)
Chip	131700	0.3	2.7
Substrate	4000	0.3	20
Nickel	205519	0.3	13.14
Copper	132400	0.34	16.7
Gold	77000	0.3	14.2
Polymer in particle	1600	0.4	70
Adhesive matrix	1600	0.4	133

5.1.3 Modelling Results

The deformation and normal stress distribution at the peak reflow temperature of 210°C is presented in Figure 5.4. The deformation is magnified by 15 times in order to provide clear information. It shows that the adhesive matrix, which has a high CTE value, expands much more than the tiny conductive particle. Higher stress is also identified around the particle where the stress in the coating layer is the highest. Along the interface between the conductive particle and metal pad, the highest stress is identified along the outer edge of the contact interface. This area could be the weakest point and a location for interfacial delamination.

The plastic strain distribution is shown in Figure 5.5, where the coating layers undergo plastic deformation and strain which are highest along the coating/adhesive matrix interface. These plastic strains are much less at the particle pad interface.

after the cure process which results from a temperature drop of 190°C to 25°C. These stresses will maintain good contact between the particles and their surroundings. Now during the reflow process these bonds can be broken due to materials swelling and this will result in loss of electrical contact in the Z-axis direction [110] which can become permanent eventually at the end of the reflow process.

Owing to the CTE mismatch between different materials in the ACF joint, the contact regions will be subject to tensile stresses at the peak reflow temperature and the loss of contact area in the connections may occur if the stresses at the interface between the particle and the pad are high. This loss of the contact area will result in an increase in the contact resistance. In time this will lead to electrical failures.

5.1.4 Parametric Study

In order to understand how material properties and geometric changes affect the stress levels in the ACF flip chip assemblies during a solder reflow, a detailed parametric analysis was carried out.

In the experimental work, contact resistance was used to characterise failure of the ACF joint. This depends on the contact area between the conductive particle and the pad surface. When tensile stresses occur at this interface there is a high probability that delamination will occur and contact resistance will increase. In this modelling work, the effect of (a) Adhesive CTE, (b) Adhesive Young's modulus and (c) bump height on the reliability of the ACF interconnections is discussed based on the stress levels at the particle/pad interface.

5.1.4.1 Effect of the CTE of the Adhesive Matrix

The CTE of the adhesive matrix is 133ppm/°C which is much higher than the CTE of the conductive particle and other metal materials. During a temperature cycle, this large CTE mismatch between different materials can induce high stresses inside the ACF flip chip assembly. This may reduce the reliability performance of the ACF joints. Previous research work [23] revealed that ACA materials with low CTE could significantly enhance thermal cycling reliability of ACA interconnections. To prove this, models with different CTE values were analyzed. The values of the normal stress σ_{yy} at the interface between the particle and the pad were recorded at the peak reflow temperature of 210°C. These results are shown in Figure 5.6. The abscissa represents the distance from the centre of the interface to the out edge of the contact area. It is found that the CTE of the adhesive matrix has a strong impact on the stress at the interface. The interfacial stress increases with an increase in the CTE of the adhesive matrix. Therefore the reliability of the ACF assembly will be enhanced when using an adhesive with a lower CTE.

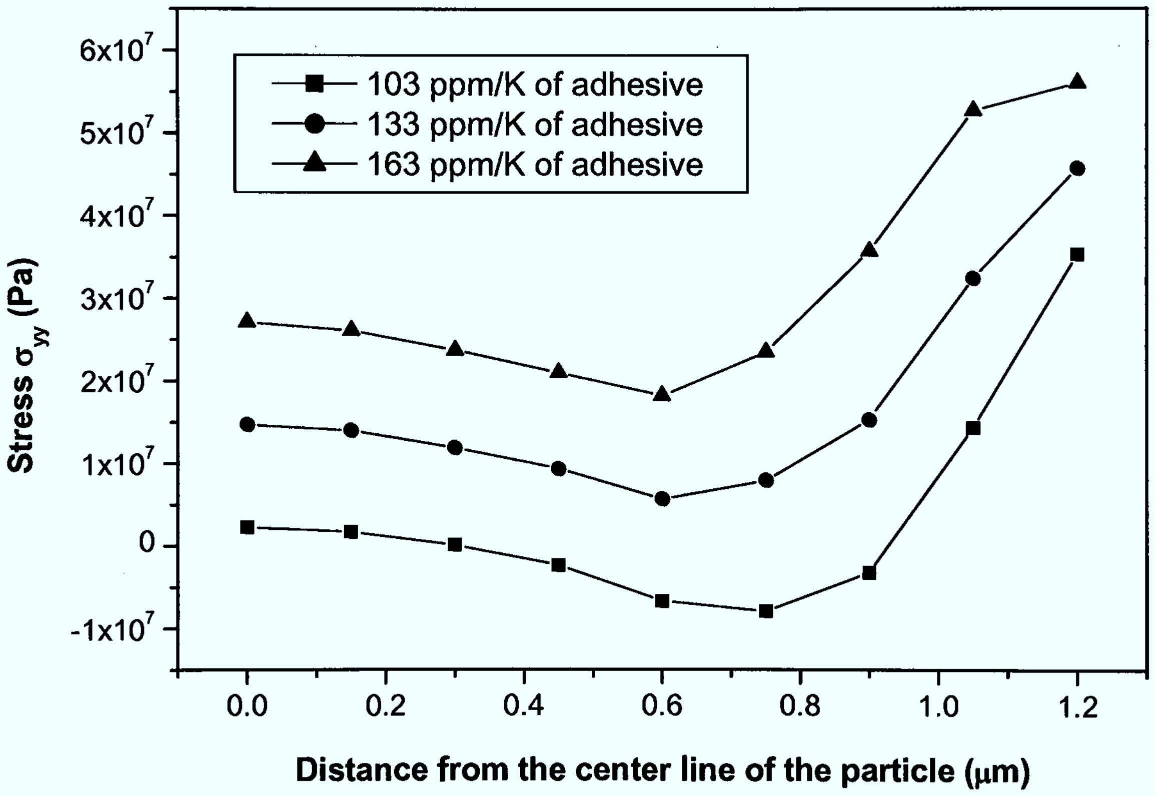

Figure 5.6: The relationship between the interfacial stresses and the CTE of the adhesive matrix

5.1.4.2 Effect of the Young's Modulus of the Adhesive Matrix

The effect of the Young's modulus of the adhesive matrix was also studied. The values of the normal stress σ_{yy} at the interface between the particle and the pad at peak reflow temperature are shown in Figure 5.7. Clearly we can see that the interfacial stress σ_{yy} decreases firstly and then increases, reaching its highest value at the point where the particle, adhesive and metal pad meet. This is a potential location of initiation of delamination. In general the stress magnitude at this location is lowered with an increase in the Young's modulus. Therefore reliability of the ACF assembly can be enhanced when using an adhesive with a higher Young's modulus.

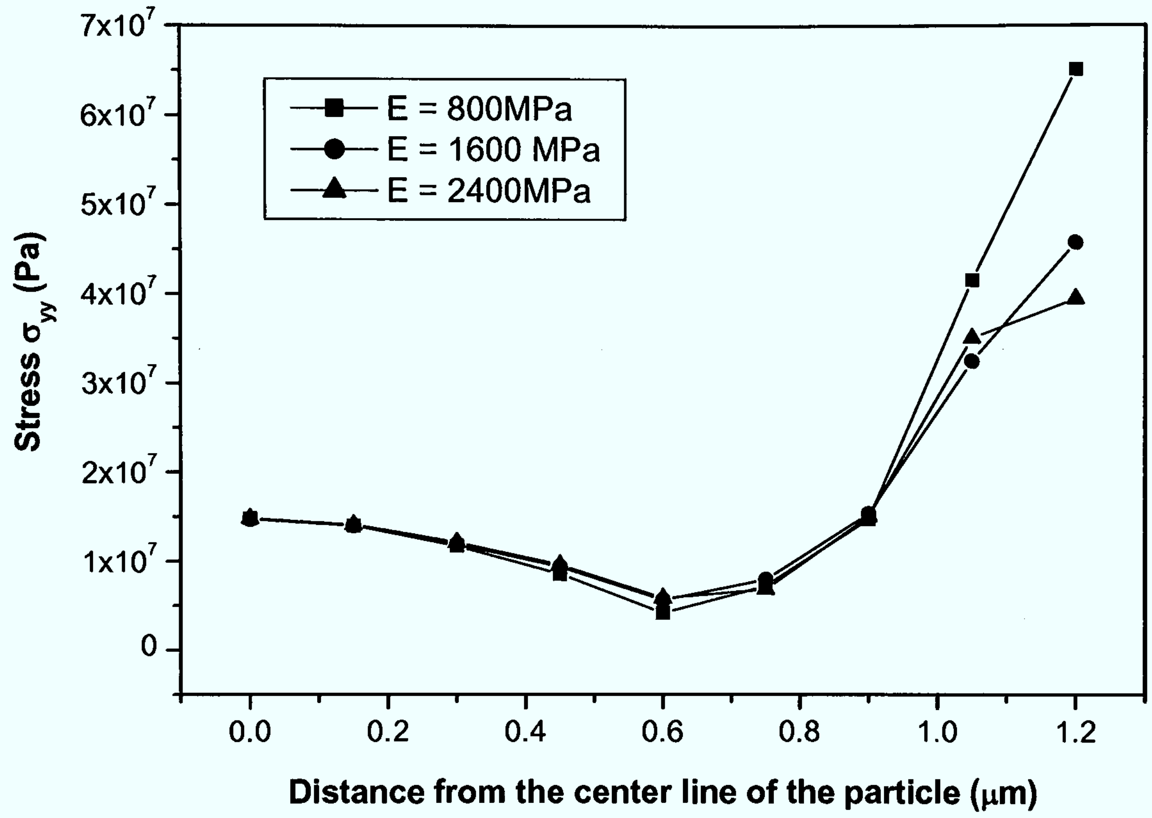

Figure 5.7: The relationship between the interfacial stress and Young's modulus of adhesive matrix

5.1.4.3 Effect of the Bump Height

Three different bump heights were analyzed to investigate their effect on the stress predictions. The distance between the chip and the substrate is dependent on the bump height, pad height and the deformed particles. Therefore, with a bigger bump height more adhesive will be in place between the chip and the substrate.

The stress values at the interface between the particle and the pad with different bump heights is shown in Figure 5.8. It can be seen that the tensile stress at the interface between the conductive particle and the pad metallization increases when the bump height increases. This conclusion contradicts what has been observed in solder based flip chips but corroborates well with experimental results for ACF joints [60][61].

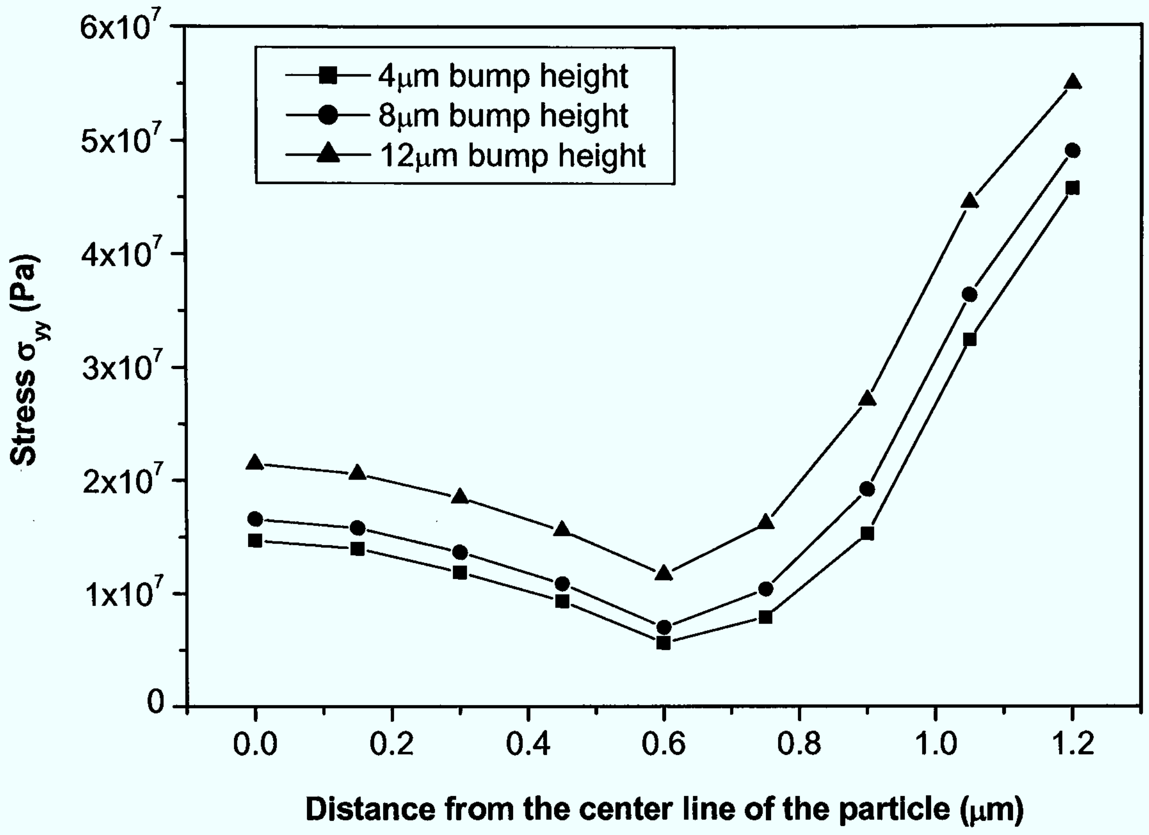

Figure 5.8: The relationship between the interfacial stresses and the bump height

In order to prove the modelling results, two sets of ACF assemblies were bonded with (a) a chip with Ni/Au bumps and (b) a chip with Au bumps. Both of these were subjected to the solder reflow profile. Owing to the different processing technology, the chips used have different bump heights, about 17μm for Au bump and 4μm for Ni/Au bump. The height of Cu/Ni/Au pad on the substrate is about 17μm. The joint resistance for both kinds of ACF assemblies was measured before and after a tin-lead solder reflow. The results are listed in Table 5.2.

For the assembly with Au bumps, the joint resistance was about 25mΩ, this value increased by more than 100% after solder reflow. For the assembly bonded with Ni/Au bumps, the joint resistance only increased by 18% after the solder reflow process.

conductive particles. Also gold does not suffer from oxidation as easily as nickel. Currently, world wide efforts are focused on the development of Ni/Au bumping technologies due to the cost concerns of gold and the complexity of gold bumping technology.

As shown in Figure 5.1, if the distance between the chip and the substrate is defined as H, and the coefficient of thermal expansion of ACF matrix in the Z direction is α, then during the temperature rise of the reflow process, the expansion of the adhesive matrix in the Z direction, ΔH can be approximated by:

$$\Delta H = H \times \alpha \times (T_2 - T_1) \tag{5.1}$$

where T_1 is room temperature and T_2 is the peak temperature of the reflow process. In this case, the expansion of the adhesive matrix in the Z direction for ACF assemblies with Au bump is nearly twice that of ACF assemblies with Ni/Au bump for the same reflow profile. Therefore, higher thermal stress in the Z direction was accumulated for ACF assemblies with Au bump. This higher stress will try to lift the chip from the substrate and result in a high probability of loss of contact areas between the particle and pad surfaces.

Clearly from the experiments we can see that the design with the higher bump height also has greater change in contact resistance. This matches the results obtained from the modelling results above.

5.2 Sensitivity Analysis

This section discusses the results from a sensitivity analysis. This technique allows us to fully characterise the sensitivity of the reliability of the ACF assembly to small changes in particular design variables.

The design variables under investigation are (a) Adhesive CTE, (b) Adhesive Young's modulus and (c) the bump height. In this study, finite element calculations were undertaken for different combinations of these design variables and using statistical techniques a response surface (RS) was established that related reliability to these design variables. This response surface is a polynomial and reliability is characterised based on the magnitude of tensile stress at the point where the adhesive, particle and metal pad meet which is taken as the design response of interest.

Normally design variables of interest have different units of measurement rendering a direct comparison of the parameter variation difficult. The sensitivity analysis in such cases requires dealing with the above issue in a certain way. The best way is to consider a RS model developed as a polynomial approximation in a normalized design space. In the normalized design space the lower limits of the design variables correspond to -1, and the upper limits to +1.

5.2.1 Scaled and Un-scaled Design Points

When dealing with experimental designs, it is often convenient to scale the design variables with respect to their upper and lower limits (i.e. the maximum and the minimum values). One of the common ways to do this is as follows [102]:

$$x_i = \frac{z_i - (\max[z_i] + \min[z_i])/2}{(\max[z_i] - \min[z_i])/2} \qquad \mathrm{i} = 1,\ldots,\mathrm{N}$$

where z_i is natural (i.e. un-scaled) design variable, x_i is scaled design variable, and N is the total number of points (i.e. simulation results) in the experimental design. When the maximum and the minimum are taken over all the values of the particular design variable (over all the points in the experimental design), each design variable scaled in such a way assumes that values are between -1 and 1.

In this study, the chosen polynomial order for the RS approximation is a full quadratic with mixed linear terms. The number of design variables is three. The construction of such a polynomial approximation requires the estimation of 10 unknown coefficients. To build the RS model and to find the values of these coefficients, at least 10 or more experiment points are required.

Design of experiments (DOE) was performed to identify these sets of design points at which the finite element analysis was undertaken to provide the stress predictions for the ACF flip chip assemblies at different combinations of design variable values. The DOE method exploited here is the "Latin Hypercube" with 15 experiments. The 15 set of design variables predicted from the DOE analysis are listed in Table 5.3.

Table 5.3: Scaled values of the design variables

	Variable 1	Variable 2	Variable 3
1	1.0	1.0	1.0
2	1.0	1.0	-1.0
3	1.0	-1.0	1.0
4	1.0	-1.0	-1.0
5	-1.0	1.0	1.0
6	-1.0	1.0	-1.0
7	-1.0	-1.0	1.0
8	-1.0	-1.0	-1.0
9	1.0	0.0	0.0
10	-1.0	0.0	0.0
11	0.0	1.0	0.0
12	0.0	-1.0	0.0
13	0.0	0.0	1.0
14	0.0	0.0	-1.0
15	0.0	0.0	0.0

The un-scaled values of these design variables were calculated and listed in Table 5.4. In total 15 sets of simulations were conducted using these design variables. The stress values at each DOE design location were predicted and used to establish the response surface and to undertake the required sensitivity analysis.

Table 5.4: Un-scaled values of the design variables and response of interest

	Design variables			Stress (MPa)
	Young's modulus (MPa)	CTE of adhesive (ppm/°C)	Bump height (μm)	
1	2400	163	12	270
2	2400	163	4	243
3	2400	103	12	128
4	2400	103	4	109
5	800	163	12	419
6	800	163	4	375
7	800	103	12	198
8	800	103	4	162
9	2400	133	8	183
10	800	133	8	281
11	1600	163	8	307
12	1600	103	8	138
13	1600	133	12	242
14	1600	133	4	213
15	1600	133	8	222
Lower bound	800	103	4	
Higher bound	2400	163	12	

lead-free solder materials. The values of the normal stress σ_{yy} at the interface between the particle and the pad at the three peak temperatures are shown in Figure 5.12. The abscissa represents the distance from the centre of the interface to the out edge of the contact area between the particle and metal pad. It shows that the stress σ_{yy} decreases firstly and then increases, reaching its highest value at the interface between the particle and adhesive matrix.

The stress also increases as the peak temperature increases. In fact, about 50% of the stress variation is observed when the peak temperature changes from 210°C to 260°C. This shows that the peak temperature may have a great influence on the reliability of the ACF interconnections, especially for the lead free soldering process in which the peak temperature is much higher.

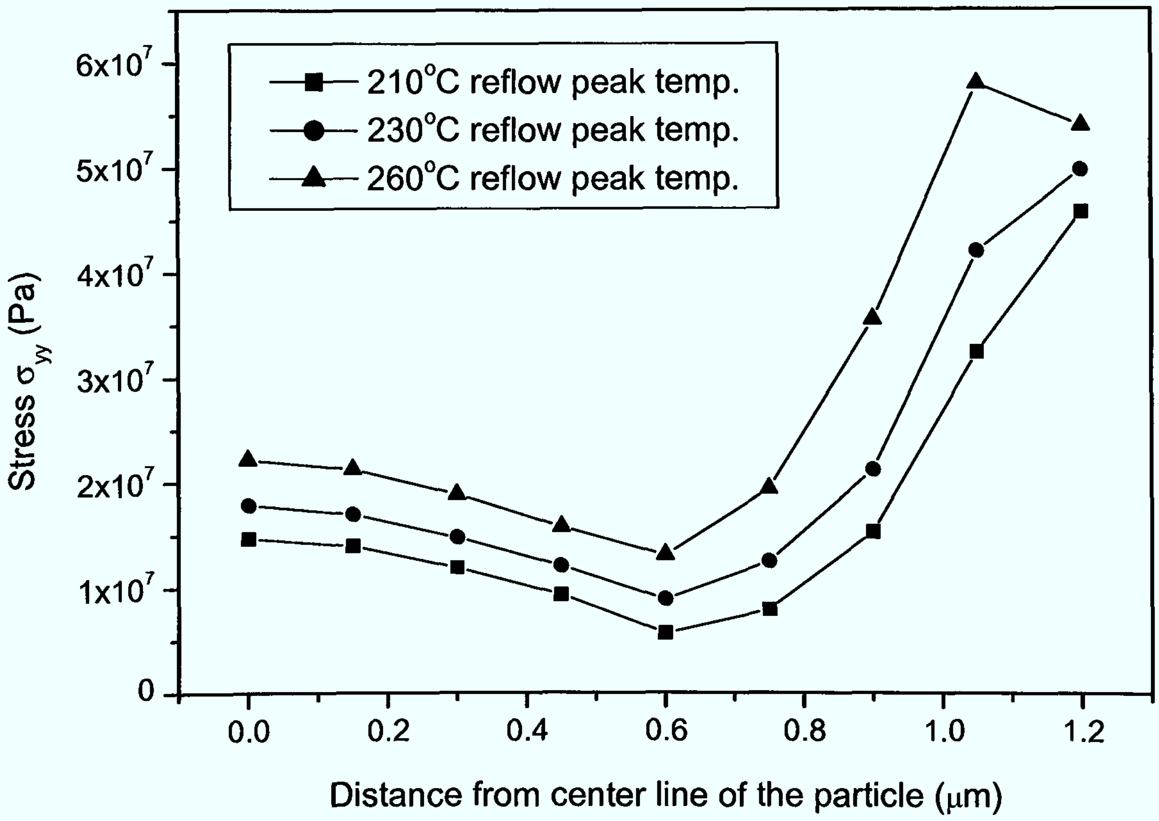

Figure 5.12: Relationship between the interfacial stress and the peak reflow temperature

The effect of the peak temperature on the reliability performance of ACF joint was also studied experimentally. The joint resistance was used as the indicator and measured using the four-point probe method which is shown in Figure 4.9, Chapter 4. Also the SEM photos of the interfacial area between the conductive particle and the pad metallization were taken to illustrate the failure information.

The reflow profile conditions and the related joint resistance test results are summarized in Table 5.5. Three sets of ACA assemblies with Ni/Au bumps were used in this experiment. When the peak temperature was 210°C, no open joints were found and the joint resistance increased by 23mΩ after the reflow process. When the peak temperature was 230°C, 5% of joints were open, and the joint resistance variation increased to 29mΩ. When the peak temperature was 260°C, nearly 40% joints were found open, and the joint resistance increased by 60mΩ. In conclusion, the peak reflow temperature has a substantial effect on the electrical performance of the ACF samples.

Table 5.5: Joint resistance with different peak temperature of reflow profile

No	Peak temperature (°C)	Time up melting point (s)	No. of test joints	Electrical Resistance (mΩ) Mean Value (Standard deviation)		No. of open joints
				Before reflow	After reflow	
1	210	60	53	124 (24)	147 (31)	0
2	230	60	36	126 (28)	155 (41)	2
3	260	60	48	123 (26)	183 (55)	16

It is clear that the conductive particles deformed very well and had a good contact with conductive metallization surfaces before the reflow process, as shown in Figure 5.13a. Although it should be noted that no delamination was found after the reflow process with peak temperatures of 210°C and 230°C, the contact area between the particles and conductive metallization surfaces decreased to some degree and this can be attributed as the main reason for the increase of contact resistance after reflow.

Based on both modelling and experimental results, the solder reflow process shows substantial effect on the electrical performance of COF samples, especially when using a lead-free solder reflow process which has a high peak temperature. The material property of the adhesive matrix and the geometry design of the flip chip can offer solutions to decrease this effect and enhance the reliability performance of ACF flip chip assembly during the reflow process.

5.4 Conclusions

In this Chapter, the effect of the solder reflow process on the reliability of ACF interconnection was studied using computer modelling. Design variables such as (a) Adhesive CTE, (b) Adhesive Young's modulus and (c) bump height were investigated to see their effect on the stresses formed within the joints. These predictions and trends were validated with experimentation.

Due to the CTE mismatch of the materials in the ACF flip chip, the stresses at the interface between the particle and its surrounding materials were significant. These were at their highest magnitude at the interface between the particle and the adhesive matrix. Through a detailed parametric analysis, it was found that the interfacial stresses increased when the CTE increased, the bump height increased and finally when the Young's modulus decreased. Sensitivity analysis showed that the most important design variable was the CTE of the adhesive.

The interfacial stresses also increased with an increase in the peak reflow temperature. For the same ACF materials, the expansion of the adhesive matrix in the *Z*-axis direction was related to the original distance between the chip and the pad which was proved in the experiments by using different bump chips.

The work in this Chapter has contributed to one journal paper [127] and a number of international conference papers [132][133][133].

Chapter 6

Hygro-Mechanical Analysis of an ACF Assembly in Autoclave Test

This Chapter presents modelling results for the autoclave test of flip-chip bonded components onto flexible substrates using ACF materials. These models exploit a multi-scale modelling approach known as three-dimensional macro-micro or global-local modelling technique. In this technique the relevant physics, temperature, moisture and stress, are modelled both at the ACF particle level and at the package level.

This Chapter starts with a discussion of the macro-micro modelling methodology adopted in this study. This is firstly illustrated for a study of a solder joint to demonstrate the efficiency and accuracy of the macro-micro modelling technique implemented in an in-house code PHYSICA. The moisture diffusion and moisture induced stresses within an ACF flip chip assembly when subjected to the autoclave test are predicted using these techniques.

The modelling results from this study are then compared with the experimental results presented in Chapter 4. Possible failure mechanisms for the ACF assemblies are then discussed. Parametric studies detail the sensitivity of package reliability to design variables such as the package geometry and properties of the materials used.

6.1 Introduction

Moisture is one of the most important factors that can affect the reliability of ACF components. Previous studies have revealed that the reliability of ACF components is strongly affected by moisture, which is predominantly considered as the most important factor of ACF component failures [8][9][10][11][12][13].

Previous modelling work [10][11][12] has been mostly limited to the analysis of simplified 2D models. Three dimensional models have focused on the micro-domain and ignored the global effects at package level, or they have modelled the whole package and used gross assumptions at the micro interconnect level [48][49][61][62]. The recognised difficulty here is that due to the vast range of length-scales in an ACF flip chip assembly, and the large number of conductive particles, an 'exact' model which includes all the particles and interconnections is simply not achievable with today's computer technology.

In this study, a 3D macro-micro modelling method is used to overcome the difficulty caused by the multi-length-scale nature of this problem and to enable a more detailed 3D representation and analysis of an ACF flip chip assembly. Two models: the macro and micro models, with different mesh sizes were built. The macro model was used to predict the overall behaviour of the whole package under moisture conditions. The displacement obtained from this global model was then used to set the boundary condition of the micro model so that the detailed stress analysis in the region around the conductive particle and between the pads can be undertaken.

6.2 Computer Modelling Technique

The experimental work presented in Chapter 4 proved that moisture absorption had a large effect on the reliability performance of ACF interconnections. In order to better understand the role that moisture plays on the reliability performance of ACF assemblies, a 3D modelling analysis of an ACF flip chip when subjected to an autoclave test was conducted.

6.2.1 Challenges in Modelling the ACF Assembly

The ACF flip chip assembly consists of the silicon chip, polyimide substrate and ACF bonding material. The diameter of the conductive particles in the ACF material is around 3.5μm and the thickness of the particle metallization is about 50nm. The die is 11mm in its length, this means that the ratio of the two is approximately 1:200,000!! In addition, there are thousands of conducting particles in a typical ACF material used to bond a flip chip component to a substrate. This means that an 'exact' model which includes all the particles and interconnections would require millions if not billions of mesh elements to be used in a finite element model. This is simply not achievable with today's computer technology. Therefore, a 3D macro-micro modelling technique is required in order to provide the ability to accurately model the behaviour of the conductive particles during the autoclave test. This is the first time that such a technique has been used in this context.

6.2.2 Macro-Micro Modelling Technique

The macro-micro modelling analysis, also referred as global-local, or sub-modelling analysis, is defined as "a procedure to determine the detailed local stress states for specific regions using information obtained from an independent global stress analysis" [103].

The global modelling allows us to study the overall effect of the entire structure. The global mesh, although relatively coarse, should be fine enough to ensure that the critical regions can be identified. These regions are then subjected to a local modelling analysis to obtain the detailed local behaviour and stress distribution. Therefore, the local model adopts a much finer mesh that can accurately represent finer geometric features at this length scale. It should be noted that the local model is independent of the global model and its nodes need not coincide with those in the global model.

The boundary conditions applied to the local model can be obtained from the global solution with interpolation. Due to the difference in mesh refinement in the local region, there is a violation in equilibrium at the global/local boundary which can be eliminated with global/local iteration. However, in engineering practice, the initial global solution is often assumed to be accurate enough and no iteration is performed [104], therefore the present study assumes such engineering procedure.

Sub-modelling is based on St. Venant's principle, which states that if a system of forces acting on a small region of a body is replaced by a different but statically equivalent system of forces acting on the same region, then such a replacement does not cause significant changes in the predicted stresses and displacements at points in the body remote from the region concerned [105][106]. It also implies that if the boundaries of the sub-model are far enough away from the stress concentration, reasonably accurate results can be calculated in the sub-model. This is the case with the sub-models used in the following analysis where the stress concentrations are located around the conductive particles.

The procedure for a macro-micro modelling analysis consists of the following four steps:

(1) Create the Global and Local Models: the global mesh refers to the mesh that models the entire structure. The local mesh refers to the mesh that models the local area of interest and is a more detailed mesh, designed to capture the local stress/strain variations.

(2) Solve the Global Model: the global model is solved and the displacement results will be used to set up the boundary conditions for the micro model.

(3) Interpolation between the Models: Interpolation of displacements from the global solution along the boundary of the local area in the global mesh is made in this step. The interpolation of data from the global mesh is necessary

because there are fewer global nodes in the global model that interface with the finer mesh for the local model at their common boundary.

(4) Solve the Local Model: the interpolated displacements are now applied to the boundaries of the local model, and the problem is consequently solved.

This modelling technique is thought to be the best approach when large-scale structures are analyzed and where the local-scale factors are crucial for the structural design of the assembly [107].

6.2.3 Interpolation of the Displacement Fields

In the finite element literature, the functions used to represent the behaviour of a field variable within an element are called interpolation functions or shape functions. Although it is conceivable that many types of functions could serve as interpolation functions, only polynomials have received widespread use since they are relatively easy to manipulate mathematically [108].

The basic ideas to use the interpolation function in the macro-micro modelling process can be illustrated by a simple example in two-dimensional space which is illustrated in Figure 6.1. Suppose that there is one element in the global mesh and its coordinates remain the same in the local mesh, but there are finer elements in the corresponding area. The question is how to solve the displacement of the nodes in the local mesh based on the known displacement of nodes in the global mesh.

In the global mesh, the displacement is solved and stored at each node in the element. In two dimensions, the simplest complete polynomial has four nodal quantities of the element. Let's assume that the polynomial for a displacement variable, *d*, is defined as:

$$d(x,y) = g_1 + g_2x + g_3y + g_4xy \qquad (7.1)$$

where x and y are Cartesian coordinates in the 2D space.

where $\mathbf{d} = \begin{bmatrix} d_1 & d_2 & d_3 & d_4 \end{bmatrix}^T$, $\mathbf{g} = \begin{bmatrix} g_1 & g_2 & g_2 & g_2 \end{bmatrix}^T$,

and

$$\mathbf{G} = \begin{bmatrix} 1 & x_1 & y_1 & x_1 y_1 \\ 1 & x_2 & y_2 & x_2 y_2 \\ 1 & x_3 & y_2 & x_3 y_3 \\ 1 & x_4 & y_2 & x_4 y_4 \end{bmatrix}$$

From Equation (7.2), we have:

$$\mathbf{g} = \mathbf{G}^{-1}\mathbf{d} \tag{7.3}$$

Expressing the terms of the interpolation polynomial Equation (7.1) as a product of a row vector and a column vector, we can write:

$$d(x, y) = \mathbf{P}(x,y)\mathbf{g} \tag{7.4}$$

where $\mathbf{P} = \begin{bmatrix} \mathbf{1} & x & y & xy \end{bmatrix}$, by submitting Equation (7.3) into Equation (7.4), we have:

$$d(x, y) = \mathbf{P}(x, y)\mathbf{G}^{-1}\mathbf{d} = \mathbf{N}(x, y)\mathbf{d} \tag{7.5}$$

where $\mathbf{N} = \mathbf{P}\mathbf{G}^{-1}$, which is called the interpolation function or shape function. This function is also used in the descritization process of finite element method, which is described in the appendices.

Finally, the displacement at the nodes in the local mesh illustrated in Figure 6.1b can be easily achieved by using Equation (7.5). In general, Equation (7.5) can also be written as:

$$d(x, y) = \sum_{i=1}^{m} N_i(x, y) d_i$$

where m is the total number of the nodes in one global element.

In the macro-micro modelling procedure, the displacements at the nodes of the global mesh are calculated first, then the displacement information from the local area in the global mesh is imported into the micro model so that the displacements of all the nodes on the boundary surface in the micro model can be calculated using the above interpolation technique. These displacements are then used as the fixed displacement boundary conditions of the local model for the detailed stress analysis.

6.3 Demonstration of the Macro-Micro Modelling Technique

In order to verify the macro-micro modelling technique implemented in PHYSICA, a thermal mechanical analysis of a solder joint was carried out. Three models were built: the macro model (coarse mesh), micro model (fine mesh) and a global model with refined mesh. The results predicted from these models were compared in order to demonstrate the accuracy and efficiency of the macro-micro modelling technique.

6.3.1 Geometry and FE Models

The structure of a greatly simplified solder joint is shown in Figure 6.2. It consists of a chip, a PCB board and a solder joint.

In order to reduce the computing time, a slice model was adopted which means that one of the plane surfaces of the materials was fixed in the Z direction and another plane surface was free to move in the Z direction. The symmetry line was fixed in Y direction and the point A on the symmetry line was fixed in the X direction. For verification purposes, three models were built as follows:

(1) The macro model with a coarse mesh. As shown in Figure 6.3a, this model has all the components of the solder joint and the mesh is coarse. It contains 372 elements and 2646 degrees of freedom.

achieved for this problem, the FE solution of a well refined mesh (a globally refined mesh) was used as the "basis" solution.

6.3.2 Material Properties

The material properties used in this simulation are listed in Table 6.1. The chip, the substrate and the copper were considered as linear-elastic materials, solder was considered as elastic-plastic material, the yield strength of solder was 30.3 MPa [109].

Table 6.1: Material characteristics used for this simulation

Material	Young's modulus (MPa)	Possion's ratio	CTE (ppm/K)
Chip	131700	0.3	2.7
PCB	4000	0.3	20
Copper	205519	0.3	13.14
Solder	132400	0.34	16.7

6.3.3 Modelling Results and Error Analysis

The contour plots of the normal strains (strain *xx*, strain *yy*) and the shear strain (strain *xy*) predicted from the macro-micro solution and the basis solution are shown in Figure 6.4 a, b, and c respectively. The first column of the results was obtained from the macro-micro models and the second column was obtained from the globally refined mesh model. It is shown that the results predicted from the macro-micro solution are very close to the "basis" solution, the strain distribution is very similar and there is only a slight difference in the value.

The relative error of the macro-micro solution at each node can be defined as

$$E_{macro-micro} = \frac{\varepsilon_{globall-refined\ solu} - \varepsilon_{macro-micro\ solu}}{\varepsilon_{globall-refined\ solu}} \times 100\,\%$$

The strains are extracted at each node in the domain of the local mesh and compared with the strain value at the corresponding location in the model from the globally refined mesh. The strain value and the error at node nearest to the centre of the solder joint are listed in Table 6.2. It is evident that the macro-micro model yields more accurate results than the global model with coarse mesh and the macro-micro model uses much less computer time than the global model with a fine mesh. For strain *xy*, which is most important strain in this model, the error is only 2%.

Table 6.2: Certain values from three models

Model	At centre of the solder joint			Number of nodes	Time (s)
	Strain *xx*	Strain *yy*	Strain *xy*		
Macro	0.44E-2	0.579E-2	-0.738E-2	882	10
Micro	0.480E-2	0.535E-2	-0.843E-2	2178	56
Global	0.536E-2	0.491E-2	-0.827E-2	5698	238
$E_{macro-micro}$	10%	9.0%	2.0%		

In order to further highlight the benefit of using the macro-micro modelling technique, the results predicted from the macro model itself were compared with the "basis" solution as shown in Figure 6.5. It is obvious that the mesh in the macro model was too coarse to capture the deformation details in the solder, so that the results were very different from the "basis" solution, both in distribution and in value.

When we use the macro-micro modelling technique, two sources of error can be identified. One is from the use of effective material properties and the other is from the implementation of the numerical scheme [107]. Since the effective material properties were not used in our modelling work, the numerical error was left as the only source of error. The use of the interpolation function and also the degree of refinement of the mesh in the macro model were the key factors in minimising this error. The mesh in the macro model must be fine enough to capture the variation of displacements at the interface but a fine macro mesh in turn increases the computational effort.

6.4 Moisture Diffusion Prediction

6.4.1 Conservation Equation in PHYSICA

The basic form of the conservation equation of a conserved quantity ϕ can be expressed mathematically by the following differential equation:

$$\frac{\partial\left(T_\phi \phi\right)}{\partial t} + div(C_\phi \underline{u} \phi) = div\left\{D_\phi grad(\phi)\right\} + S_\phi \tag{7.6}$$

Where T_ϕ, C_ϕ are the coefficients of the transient and convection term respectively, D_ϕ is the diffusion coefficient and S_ϕ is the source term.

During the moisture diffusion in solid material considered in this work, the convection term and the source term can be omitted so that Equation (7.6) can be rewritten as:

$$\frac{\partial\left(T_\phi \phi\right)}{\partial t} = div\left\{D_\phi grad(\phi)\right\}$$

If the diffusion coefficient D_ϕ is a constant in a material, the above equation can be written as:

$$\frac{\partial(T_\phi \phi)}{\partial t} = D_\phi\left(\frac{\partial\phi}{\partial x^2}+\frac{\partial\phi}{\partial y^2}+\frac{\partial\phi}{\partial z^2}\right) \tag{7.7}$$

By setting $T_\phi = 1$, substituting the moisture concentration C for the scalar variable ϕ, and replacing the general diffusion coefficient D_ϕ with the moisture diffusion coefficient D, Equation (7.7) can be used for the moisture diffusion analysis.

However, Equation (7.7) which is available in PHYSICA can not be used directly if there is more than one material in the solution domain. This is because that unlike the temperature distribution which is continuous in nature. The moisture concentration C is discontinuous at material interfaces because the saturated concentration values are not the same for different materials. This problem is illustrated in Figure 6.6. Due to the discontinuity at the interface between different materials, Equation (7.7) can not be used for moisture prediction for multi-material solution domain unless the discontinuity is removed.

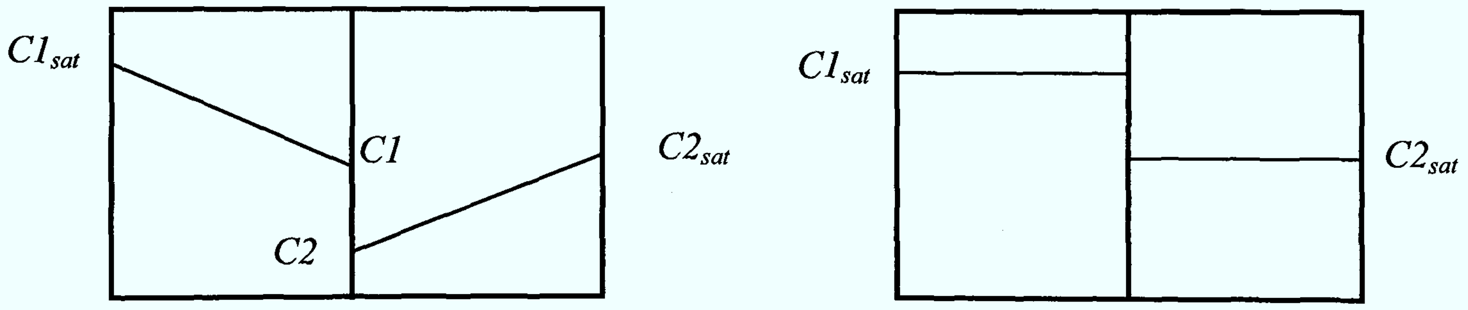

(a) Unsaturated

(b) Saturated

Figure 6.6: Moisture concentrations across bi-material interface

6.4.2 Wetness Fraction Approach

A wetness faction approach is introduced to solve the above problem [114]. A new field variable named wetness fraction, W, is defined as

$$W = \frac{C}{C_{sat}}, \quad 1 \geq W \geq 0$$

where C_{sat} is the maximum moisture concentration that can be absorbed by the material under certain temperature, the lower limit ($W = 0$) means the material is fully dry, and the upper limit ($W = 1$) means the material is fully saturated with moisture. The wetness fraction W was proved to be continuous across bi-material interface [114]. The wetness fraction profile corresponding to Figure 6.6 can be depicted as Figure 6.7.

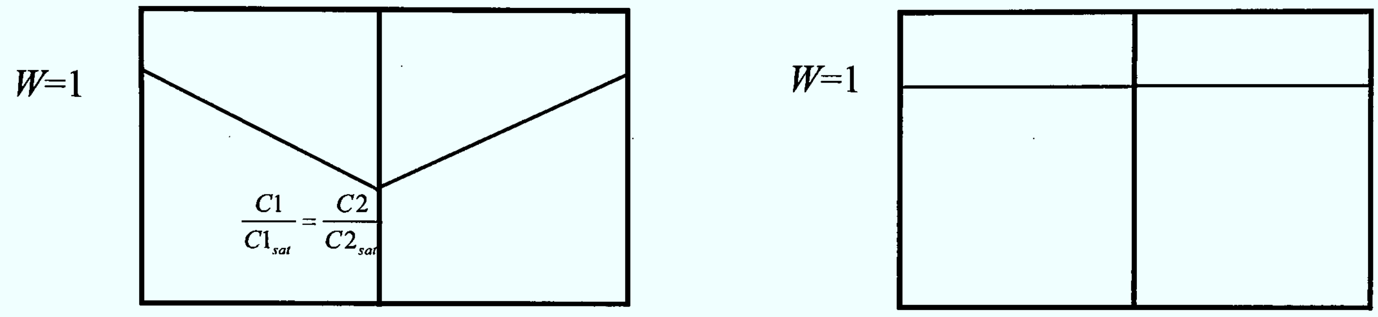

(a) Unsaturated

(b) Saturated

Figure 6.7: Wetness fraction across bi-material interface

Therefore, if we define wetness faction W as the concerned scalar variable ϕ, Equation (7.7) can be written as:

$$\frac{\partial (C_{sat}W)}{\partial t} = D\left(\frac{\partial^2 (C_{sat}W)}{\partial x^2} + \frac{\partial^2 (C_{sat}W)}{\partial y^2} + \frac{\partial^2 (C_{sat}W)}{\partial z^2} \right) \tag{7.8}$$

In a domain with only one material, C_{sat} is independent of the location and the above Equation (7.8) can be simplified as:

$$\frac{\partial W}{\partial t} = D\left(\frac{\partial^2 W}{\partial x^2} + \frac{\partial^2 W}{\partial y^2} + \frac{\partial^2 W}{\partial z^2} \right)$$

When Equation (7.8) is used to predict the wetness fraction distribution in a multi-material system, the transient coefficient T_ϕ is then defined as C_{sat} and D_ϕ is defined as the product of C_{sat} and D. Once the wetness fraction W is solved, the moisture concentration C can be easily obtained by:

$$C = C_{sat} \times W$$

This wetness fraction method was firstly introduced by Wong *et al.* in 1998 [114] for predicting the moisture absorption in an IC package. Due to the improvement in simplicity and computational efficiency, this method is becoming widely used for predicting the moisture concentration in IC packages [115][116][117][118][119]. Most importantly, the wetness fraction method enables the use of commercial thermal analysis software to model the transient moisture diffusion phenomenon in a multi-materials package. The relationship between them is shown in Table 6.3.

Table 6.3: The relationship of the thermal and moisture simulation [115]

Properties	**Moisture**	**Thermal**
Field variable	Wetness(C/C_{sat})	Temperature (T)
Density	1	ρ
Conductivity	D^*C_{sat}	k
Specific Gravity	C_{sat}	c_p

Because of the analogy between thermal conduction and moisture diffusion, the simulation of moisture diffusion process in a multi-material package can also be done using the HEAT Module in PHYSICA package. The implemented moisture prediction technique could therefore be tested by solving moisture diffusion as a typical thermal problem. In this research, the moisture diffusion analysis was predicted using the SCALAR module in PHYSICA and the moisture induced stress was predicted using EVP module, so that the thermal conduction and moisture diffusion analysis can be coupled when the thermal effect has to be taken into account.

6.5 Modelling Analysis of an ACF flip chip Assembly

In this section, the hygro-thermal mechanical analysis of an ACF flip chip assembly using a 3D macro-micro modelling technique is explained and the results of moisture concentration and moisture induced stresses are presented.

6.5.1 Geometry and Mesh Model

In order to compare the computer modelling results with the results from the experiments, a typical flip chip on flex (FCOF) assembly with an 11mm × 3mm × 1mm chip and a total of 368 Ni/Au peripheral pads was used throughout this analysis. The dimensions of the bumps were 50μm × 50μm × 20μm. The substrate was made of polyimide, 25μm in thickness and the metal pads on the substrate were made of nickel-gold plated copper. The thicknesses are 12μm, 4μm and 0.5μm for the copper pad, nickel layer and gold coatings respectively. The gold layer was neglected in the model since it is very fine in thickness. The layout of the chip is shown in Figure 6.11.

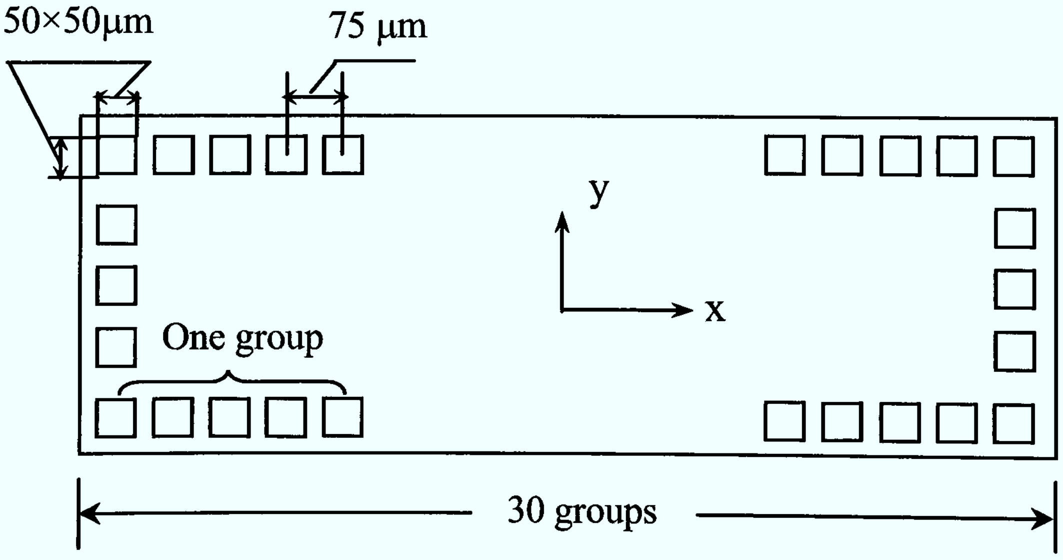

Figure 6.11: The layout of the silicon chip

The macro model of this ACF flip chip assembly is shown in Figure 6.12. In order to reduce the size of the FEA model and save the computing time, the modelled

Table 6.5: Moisture properties of the ACF and polyimide substrate

	Diffusion coefficient (mm^2/s)	Saturated moisture Concentration (g/mm^3)	CME (mm^3/g)
ACF	12.3E-6	32.3E-6	1.7E2
Polyimide	1.0E-6	16.15E-6	1.0E2

6.5.3 Modelling Results

Three groups of modelling results are presented: moisture diffusion, moisture or temperature induced stresses, and parametric analysis. The moisture diffusion was predicted using the macro model and the detailed stress analysis was carried out using the micro model. In the parametric analysis, the effects of the CME, the Young's modulus of the adhesive matrix, and the bump height of the chip on the moisture induced interfacial stresses were studied.

6.5.3.1 Moisture Diffusion

The moisture diffusion analysis was coupled with the stress analysis so that the displacement field and the moisture concentration were solved simultaneously. Figure 6.14 shows the wetness fraction at the centre of the package versus the time, it is noted that the time it took for the adhesive to be fully saturated is very much dependent on the moisture properties of the polyimide substrate. The package is not saturated in the first 50 hours of the autoclave test if we assume that the substrate does not absorb any moisture. However, the polyimide substrate does absorb moisture and the ACF package can be fully saturated within the first 12 hours of the autoclave test and the duration can be even shorter when higher moisture diffusion rate of the polyimide is used. This result implies that the moisture property of the polyimide substrate is a crucial factor in the reliability performance of the flip chip on flex in a humid environment.

6.6 Failure Mechanisms

In the past many researchers have suggested a variety of driving forces responsible for the ACF joint failures in humid environment. These include polymer expansion due to moisture absorption, the loss of the adhesion strength [8][12], the degradation of the polymer [8], and stress corrosion and oxidation of the metal particles [9]. However, no definitive conclusion was made and no direct evidence was found to pinpoint the major cause of the electrical failures in the ACF assemblies for flip chip on flex applications.

According to the modelling results reported in this research, for an ACF flip chip on a polyimide substrate, the time to moisture saturation is strongly dependent on the moisture properties of the polyimide substrate. Most of the moisture that diffuses into the ACF layer is via the polyimide substrate rather than the perimeter of the ACF layer since the polyimide substrate is very thin. The full saturation of an ACF flip chip assembly can be expected in the first 12 hours of the autoclave test. In the experiments, 85% of the ACF joints failed in the first 24 hours test when 100% increase in joint resistance was observed in these joints. However, most of the open joints were observed only after 24 hours' test and therefore a more dramatic increase in joint resistance was observed between 24 to 96 hours' test. Based on the modelling and experimental results, it can be concluded that moisture absorption rather than the temperature change was the major cause of the ACF failures during the autoclave test. However, delaminations at the material interfaces can not be seen as a catastrophic event governed by a critical water concentration only.

Lam *et al.* [40] developed a chemical kinetic model of interfacial degradation of adhesive joints and concluded that the time to failure of an adhesive joint in a humid environment was dependent on the saturation water content, stress gradient, water concentration gradient, and exponentially dependent on the peak stress in the adhesive joint. Moreover, the loss of adhesive strength was thought to correlate directly to the interfacial moisture concentration [8][28]. According to the surface energetics, the water layer can form at the interface between the polymer and the metal which decreases the adhesive strength of the interface. Small portion of moisture can also diffuse through the interfaces between the adhesive and the other materials if there was de-adhesion at these interfaces [110][119]. The remaining difficulty is that the rate at which moisture is delivered to the interface and the degradation of the mechanical properties of the adhesive due to moisture uptake are not well understood. Further experimental and modelling work is required to solve this problem.

In summary, the adhesive matrix and polyimide both absorb moisture easily. In the autoclave test, moisture absorption in these materials induces tensile stress that contributes to the joint opening. The moisture absorption and induced stress plays an important role in the ACF failures in the autoclave test.

6.7 Conclusions

The technique of computer modelling of moisture diffusion in multi-material assembly has been incorporated into the PHYSICA multi-physics modelling framework. A macro-micro modelling technique was applied in the hygro-mechanical analysis of an ACF flip chip assembly so that a more detailed analysis could be carried out.

It was found that the reliability performance of ACFs in assemblies of flip chip on flex substrate was strongly affected by moisture. During the autoclave test, moisture diffused mostly through the substrate into the ACF layer and the time to be fully saturated with water in the adhesive was strongly dependent on the moisture properties of polyimide substrate. Due to the CME mismatch in the system, higher stress was identified along the interface between the adhesive and the bump/pad. The predominantly tensile stress found at the interface between the conductive particle and the metallization reduced the contact area, while the thermal stress had the opposite effect. The parametric analysis suggested that the tensile stress at the particle/pad interface increased with the CME of the adhesive matrix and decreased with the

Young's modulus of the adhesive matrix. The interfacial stress showed slight increase with bump height. It is believed that higher stresses would cause more loss of contact area and therefore a larger increase in the contact resistance.

The work in this Chapter has contributed to one journal paper [128], a number of international conference papers [133][135][137] and one paper for a trade magazine [138].

Chapter 7

Conclusions and Further Work

This Chapter presents a summary of the major conclusions resulting from this research project and ideas for future work.

7.1 Conclusions

Driven by the desire to protect the environment, the electronics packaging industry is eager to replace the traditional Sn/Pb solder materials. Currently, there are several alternative materials being investigated which include lead-free solder alloys, conductive adhesives and non-conductive adhesives. Anisotropic Conductive Film (ACF) is a conductive adhesive which is gaining popularity for use in products such as flat panel Liquid Crystal Displays (LCD), Smart Cards and Disk Drives. This material is attractive as it is low cost and enables fine pitch connections, low processing temperature and satisfies environmental legislations such as RoHS.

However, the reliability performance of ACF, particularly in harsh conditions is a concern and it is widely acknowledged that further research is required in this area. This has been the focus of this PhD study. In particular, the PhD has investigated the effect of (i) solder reflow temperatures and (ii) moisture absorption on the reliability of this material. The methodology used in the study was based on both experimental techniques and finite element analysis.

Chapter 4 (Experiments) and Chapter 5 (Modelling) discuss the effect of Sn/Pb solder reflow on the stress magnitudes and failure modes in an ACF joint. The experimental results demonstrated that a subsequent solder reflow process has a substantial effect on the stress magnitudes around the ACF particles. It is clearly shown that the adhesive expands during the reflow process and this breaks the contact between the conducting particle and the pads on the chip and substrate. This also creates high stress levels at the interface between the conductive particle and the metal pads. The magnitude of this interfacial stress increases with the reflow peak temperature. This means that the reflow effect on the reliability performance is greater when moving from a Sn/Pb soldering process to a lead free soldering process.

Key design variables identified during this study are (i) adhesive CTE (ii) adhesive Young's modulus and (iii) bump height. The interfacial stress decreases when the CTE decreases and when the Young's modulus increases. It also decreases when the bump height is lower. Another finding is that ACF components when subjected to a subsequent solder reflow profile fail quicker than those that are not subjected to a reflow profile. The reliability test used in this case was autoclave test as discussed in Chapter 4.

The moisture effect on the reliability performance of ACF joints was discussed in Chapter 4 (Experiments) and Chapter 6 (Finite Element Modelling). The experimental results showed that moisture had a major effect on the reliability performance of the ACF joint. Here the measured joint resistance increased and some cracks were also observed around at the pad/adhesive/substrate interfaces using SEM.

A 3D macro-micro finite element modelling technique was adopted in order to couple the moisture effects at package and joint levels in much greater details than what has been undertaken before. The results show that the ACF assembly is fully saturated with moisture after 12 hours of autoclave test. The majority of moisture diffused into the ACF layer comes from the substrate side rather than the perimeter of the ACF. This is because the polyimide substrate is very thin and hence moisture can diffuse quickly through the base of the substrate. This rate of absorption is dependent on the moisture properties of the polyimide substrate which are key parameters. As expected an increase in the moisture diffusion of the polyimide accelerates the rate at which moisture propagates into the ACF significantly.

Moisture induced stress is predicted using the micro model. Here results from the macro (package) model are used for setting up the boundary condition for the micro-model. Results from the macro model show that higher stress is found at the interface between the adhesive/substrate/pad. This is the location where cracks are always observed to occur. The stress between the conductive particle and the metallization is tensile and this indicates that moisture is swelling the adhesive which tries to move the pads away from the conductive particle – hence increasing the contact resistance. The parametric analysis shows that this interfacial stress will increase when the saturation concentration (C_{sat}) increases and/or when the bump height increases. It will decrease when the Young's modulus of the adhesive increases.

In the autoclave test there are two external forces that can result in stress and failure. These are Temperature and Moisture. This study has clearly shown that Moisture is much more severe than temperature in this test. Although the debonding of ACF joints can be caused by many factors, the stresses due to adhesive swelling are significant. This was also reported by Lam *et al.* [40].

7.2 Further Work

Some possible further work is discussed from two aspects: experiment and computational modelling. The overall challenges with ACFs are summarized at the end of this Chapter.

7.2.1 Experiments

Further experimental work is required to fully understand the failure mechanisms of ACF joints when subjected to variable service conditions. This would be analysed using combination tests that combine thermal cycling, with moisture and vibration. Like all of the joint types this is a very challenging area.

This study only tested the performance of reflowed ACF joints using the autoclave test. Further work should investigate the performance of these joints when subjected to other reliability tests based on thermal cycling or vibration to fully characterise the impact of subsequent reflow profiles on joint performance and reliability.

7.2.2 Computational Modelling

Good qualitative comparisons have been made between the finite element results and the experiments in this research. A number of assumptions have been adopted in this study. Future work should aim to address the following:

(1) Characterise the effect of the Bonding Stress on the results presented here. In this research, the stress created during the bonding process was neglected for simplicity. This should be investigated in future work.

(2) Use Visco-elastic material data for the ACF matrix. In this modelling analysis the ACF is assumed to be elastic. This was due to difficulty in obtaining suitable materials data. In future as non-linear materials data becomes available this should be built into the model.

(3) Extend the Macro-Micro modelling approach to other conductive adhesive systems. The modelling technique developed for the moisture diffusion and moisture induced stress analysis can be easily applied to study other adhesive connections such as Non-Conductive Adhesive and Isotropic Conductive Adhesive joints.

7.2.3 Future Challenges with ACAs

Based on the literature review, more research is required in the future in order to achieve wider usage of ACAs. The overall challenges with this material are concluded as follows:

- High frequency behaviour. High frequency modelling is necessary to understand the high frequency characteristics of flip chip interconnections using ACFs [121]. This is especially the case at the frequency range beyond 20GHz. The maximum current carrying capability at high frequency after exposure to various environmental tests needs to be understood.

- The co-planarity effect of the substrate on the ACA joint reliability. Generally, there are two kinds of bonding tolerance in ACA packaging. This can be (i) in-plane misalignment between the chip and the substrate, which may be translational or rotational, and (ii) co-planarity variations between the joint planes. Experimental research on the in plane misalignment of components in ACA assemblies had been carried out in previous research [123]. However, to our knowledge, there has been no previously reported detailed research into the effects of co-planarity variations. Bad co-planarity ACA packaging can be caused by the rotated chip alignment, distorted components and different height pads [124].

- Life time prediction models of ACA joints. Various aspects of the processing, manufacturing, thermal, mechanical and electrical performance and reliability testing data of the ACA material have been examined. However, there are today no methods available that can be used to predict ACA joint life. This is because many of the failure mechanisms that are not well understood [125].

Appendices

These appendices detail both the theory of mass diffusion and solid mechanics. The manner in which a material behaves is discussed and the governing mathematical equations for elasticity, plasticity and rate dependent material behaviour are outlined. The discretisation of these mathematical equations, over a computational mesh using the finite element method, is then discussed. Finally, the PHYSICA multi-physics software framework is presented and demonstrated through the analysis of a Liquid Crystal Display (LCD).

A. Differential Equation of Diffusion

Diffusion is the process by which mass is transported from one part of a system to another as a result of random molecular motions. The mathematical theory of diffusion in isotropic substances is based on the hypothesis that the rate of transfer of diffusing substance through a unit area of a section is proportional to the concentration gradient measured normal to the section, i.e.:

$$F = -D\frac{\partial C}{\partial x} \tag{A.1}$$

Where F is the rate of transfer per unit area of the section, C is the concentration of diffusing substance, x is the space co-ordinate measured normal to the section, and D is called the diffusion coefficient and can be reasonably taken as constant in most cases [111]. The fundamental differential equation of diffusion in an isotropic medium which is known as the Fick's second law of diffusion can be derived from Equation (A.1) as follows.

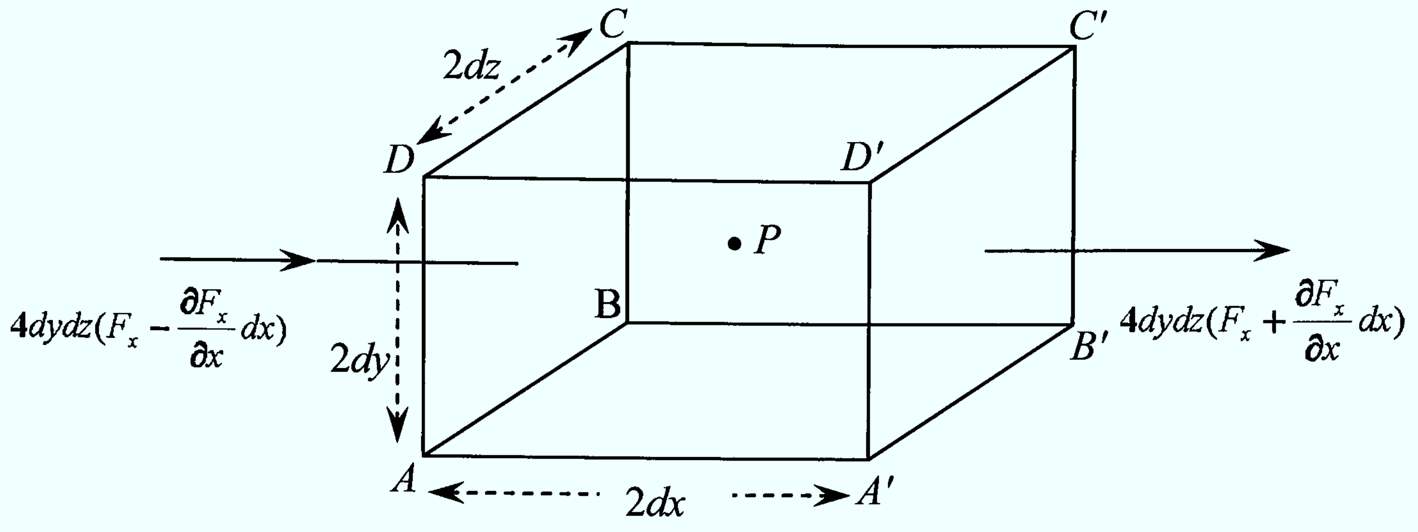
C
C'
2dz
D
D'
P
B
B'
$4dydz(F_x - \frac{\partial F_x}{\partial x}dx)$
$4dydz(F_x + \frac{\partial F_x}{\partial x}dx)$
2dy
A
2dx
A'

Figure A.1: Element of volume

Consider an element of volume in the form of a rectangular parallelepiped whose sides are parallel to the axes of coordinates as shown in Figure A.1, the contribution to the rate of increase of diffusing substance in the element from the face *ABCD* to *A'B'C'D'* is equal to

$$-8dxdydz\frac{\partial F_x}{\partial x}$$

Similarly from the other faces we obtain:

$$-8dxdydz\frac{\partial F_y}{\partial y} \text{ and } -8dxdydz\frac{\partial F_z}{\partial z}$$

Since the rate at which the amount of diffusing substance in the element increases is also given by $8dxdydz\frac{\partial C}{\partial t}$, hence we can get:

$$\frac{\partial C}{\partial t}+\frac{\partial F}{\partial x}+\frac{\partial F}{\partial y}+\frac{\partial F}{\partial z}=0$$

If the diffusion coefficient is a constant in a material, the above equation can be written as follows which is known as Fick's second law of diffusion:

$$\frac{\partial C}{\partial t} = D\left(\frac{\partial^2 C}{\partial x^2} + \frac{\partial^2 C}{\partial y^2} + \frac{\partial^2 C}{\partial z^2}\right) \tag{A.2}$$

The moisture uptake in one material can be predicted by using the above equation [11][12][114]. When used for moisture prediction, C (g/mm^3) is the moisture concentration which describes how much moisture is absorbed in the material; D (mm^2/s) is the coefficient of moisture diffusion which describes how fast the mass diffuses.

The general transport equation for a scalar variable ϕ can be expressed as:

$$\frac{\partial\left(T_\phi \phi\right)}{\partial t} + div\left(C_\phi \underline{u}\phi\right) = div\left\{D_\phi grad\left(\phi\right)\right\} + S_\phi \tag{A.3}$$

where T_ϕ, C_ϕ are the coefficients of the transient and convection term respectively, D_ϕ is the diffusion coefficient and S_ϕ stands for the source term. ϕ could stand for any physical quantity that obeys the transportation law.

Each of the terms in the general conservation equation represents a different phenomenon or aspect of quantity transportation. The first term on the left side of Equation is the transient term and the second is the convection term. On the right side of the equation, there are the diffusion term and the source term respectively. Depending on the nature of analyzing process, all or just some of these terms will exist in the equation to govern the corresponding physical phenomenon.

When ϕ stands for the temperature in the heat transfer equation, the equation governing the heat transfer phenomenon can be written as:

$$\frac{\partial(\rho c_p T)}{\partial t} + div(\rho c_p \underline{u} T) = div(k grad(T)) + S_\phi \tag{A.4}$$

where ρ is the density, c_p is the specific heat, k is the thermal conductivity and the conserved variable is temperature T. If without the convection and source terms, Equation (A.4) can be written as:

$$\frac{\partial(\rho c_p T)}{\partial t} = div(k grad(T))$$

or

$$\frac{\partial(\rho c_p T)}{\partial t} = k\left(\frac{\partial^2 T}{\partial x^2} + \frac{\partial^2 T}{\partial y^2} + \frac{\partial^2 T}{\partial z^2}\right) \tag{A.5}$$

Considering the analogy of the Equation (A.5) with Equation (A.2), the heat governing Equation (A.5) can be used for the moisture prediction in one material based on the transformation of the transient and diffusion coefficients as listed in Table A.1.

Table A.1: The relationship of the thermal and moisture simulation

Properties	**Moisture**	**Thermal**
Field variable	Concentration (*C*)	Temperature (*T*)
Density	1	ρ
Conductivity	*D*	*k*
Specific Heat	1	c_p

B. Material Behaviours

The material behaviours in solid mechanics can be classified into three categories, material linearity, rate independent material non-linearity and rate dependent material non-linearity. Some of the most important cases are described for each category in the following sections.

B.1 Elasticity

An elastic material returns to its original shape when external forces that deformed it have been removed. The material can be classified as both linear and non-linear. With a linear elastic material, the strains and displacements produced are all directly proportional to the applied forces. The general form of the constitutive equation that describes a linear elastic material is:

Stress = E × Strain,

Where E is a constant and called Young's modulus or the modulus of elasticity of the material. Most metallic materials, when subjected to sufficiently small strains, exhibit linear elasticity [105][139].

Non linear elasticity is defined when the stress is not linearly related to the strain, in this case the deformation is still recoverable and the material returns to its original shape and no energy is lost from the system.

B.2 Plasticity

When a material deforms plastically its does not return to its original shape when the external forces are removed. The material remains permanently deformed and energy, generally in terms of heat is lost in the system. The stress at which plastic deformation begins is called the yield point. At stresses below this yield point the material will deform elastically. When the stress is above this threshold, a combination of elastic and plastic deformation occurs. Most engineering materials in solid mechanics exhibit elasto-plastic behaviour. Figure B.1a illustrates the stress-strain behaviour for an elastic, perfectly plastic material and Figure B.1b for an elastic, linear work-hardening material. Work hardening, *i.e.* strain hardening, is an increase in mechanical strength due to plastic deformation.

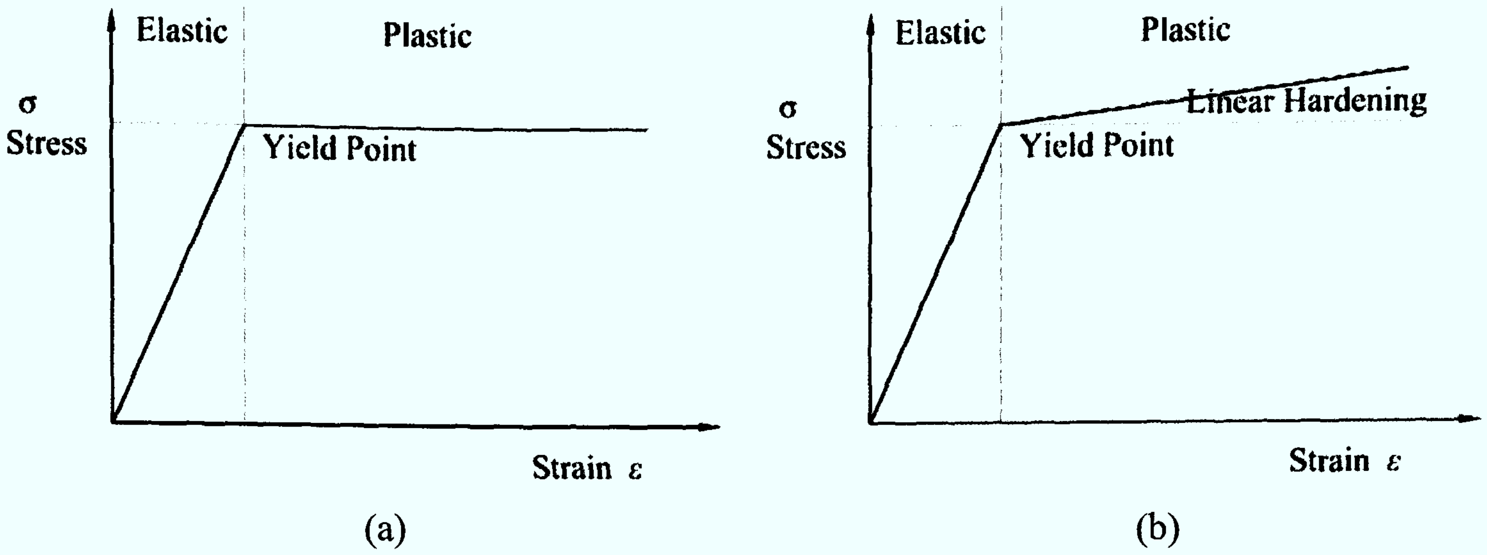

Figure B.1: Plastic material behaviour. (a) Elastic, perfectly plastic and (b) elastic, linear work hardening

B.3 Rate Dependent Material Behaviour

Both of the above descriptions of material behaviour have ignored the effect of time or the rate at which a force is applied to a material. This will affect the stress-strain behaviour of the material both during elastic and plastic deformation. The contribution of time also describes how a material creeps and stress relaxes over time. The importance of time is dependent on the material and loading application be analysed and sometimes it can be ignored.

Visco-Elastic constitutive laws describe the rate dependency behaviour of linear or non-linear elastic materials such as polymers, and rubbers, etc. This behaviour is exploited for smart and shape memory materials, which consists of the full history of the viscous strain development [140].

Visco-Plastic constitutive laws describe the rate dependency behaviour of linear or non-linear plastic materials such as metals. This behaviour always results in permanent deformation of the material and possesses the yield criterion as described for rate independent plasticity. Materials exhibiting visco-plastic behaviour are assumed to be rate independent below the yield point and rate dependent when the yield point is exceeded.

C. Finite Element Method (FEM)

The finite element method [141][142][143] is a numerical technique for obtaining solutions to a wide variety of engineering problems. In more and more engineering situations today, it is increasingly necessary to use modelling techniques such as the finite element method.

The label 'finite element method' first appeared in the 1960s, when it was used by Clough [145] in a paper on plane elasticity problems. However, the ideas behind the method date back much further. In the 1940s, Hrennikoff [146] and McHenry [147] made the first contribution to the development of finite element method by solving stresses in solids using one-dimensional elements. In 1956, Turner *et al.* [148] proposed the numerical procedures of the direct stiffness method and two-dimensional finite elements.

After more than 50 years of development, the finite element method now has received widespread use in engineering and is applicable to many application areas such as structural analysis, heat transfer, fluid flow and electromagnetic etc.

The solution of a continuum problem using FEM always follows an orderly step-by-step process [144]. The first step is to **discretize the continuum** or solution domain into a mesh called the finite elements. The more elements that are used to model the solution domain, the better the accuracy of the results. However, increasing the number of elements leads to high computational expenses.

The second step is to **select the interpolation functions** to approximate the variation of the variables over each element. Often, although not always, polynomials are selected as interpolation functions for the variables because they are easy to integrate and differentiate.

The third step is to **calculate the matrices** that represent each element. Once the finite element is established, the matrix equations expressing the properties of the individual elements are determined. For this task, the weighted residual approach also called Galerkin's method is used.

The fourth step is to **assemble all of the matrices into a global matrix.** To find the properties of overall system modelled by the network of elements, the important thing is to combine the matrix expressions expressing the behaviour of the elements and form the matrix equations expressing the behaviour of the entire solution region. The matrix equations for the system have the same form as the equations for an individual element except that they contain many more terms because they include all the nodes that make up the computational mesh.

The last step is to **solve the global system of equations.** The assembly process of the proceeding step gives a set of simultaneous equations that can be solved to obtain unknown nodal values of the field variables. Both direct (*i.e.* Gaussin Elemination) and iterative (*i.e.* Gauss-Seidel or Conjugate Gradient) solvers can be used to solve this global matrix. For non-linear problems where stress is a function of both the stain and stress states numerical techniques such as the Newton-Raphson method can be used in addition to direct and iterative matrix solvers.

Since the finite element solution technique is a numerical procedure, it is necessary to assess the accuracy of the final solution. If the accuracy criteria are not met, the numerical solution has to be repeated with refined solution parameters (such as finer meshes) until a sufficient accuracy is reached.

C.1 Linear Elasticity

A very important application area for finite element analysis is the elastic analysis of solids and structures. This is where the first practical finite element procedures were applied and where the finite element method has obtained its primary impetus of development. In this section, the procedure of using the finite element method to solve the mathematical model of elastic deformation due to both external mechanical forces and thermal, hygroscopic loads is explained.

C.1.1 Equilibrium Equations

The equilibrium equations govern the conservation of force. For a time independent static analysis these equations are:

$$\begin{aligned}
\frac{\partial \sigma_{xx}}{\partial x}+\frac{\partial \sigma_{xy}}{\partial y}+\frac{\partial \sigma_{xz}}{\partial z}&=f_x\\
\frac{\partial \sigma_{xy}}{\partial x}+\frac{\partial \sigma_{yy}}{\partial y}+\frac{\partial \sigma_{yz}}{\partial z}&=f_y\\
\frac{\partial \sigma_{xz}}{\partial x}+\frac{\partial \sigma_{yz}}{\partial y}+\frac{\partial \sigma_{zz}}{\partial z}&=f_z
\end{aligned} \tag{C.1}$$

where σ_{ij} and f_i are the components of stress and the body forces acting in the direction represented by i. For an isotropic homogeneous material undergoing small strains, the stress is related to the elastic strains via the linear elastic constitutive equation which in matrix form is

$$\sigma = \mathbf{D}\varepsilon^{(e)} \tag{C.2}$$

where for an isotropic material the stress σ and elastic strain $\varepsilon^{(e)}$ are represented by vectors of six components:

$$\begin{aligned}
\sigma &= \begin{bmatrix}\sigma_{xx} & \sigma_{yy} & \sigma_{zz} & \tau_{xy} & \tau_{yz} & \tau_{zx}\end{bmatrix}^{\mathrm{T}}\\
\varepsilon^{(e)} &= \begin{bmatrix}\varepsilon_{xx}{}^{(e)} & \varepsilon_{yy}{}^{(e)} & \varepsilon_{zz}{}^{(e)} & \gamma_{xy}{}^{(e)} & \gamma_{yz}{}^{(e)} & \gamma_{zx}{}^{(e)}\end{bmatrix}^{\mathrm{T}}
\end{aligned}$$

The elastic material matrix **D** contains the elastic material terms which in three dimensions are given by:

$$\mathbf{D}=\frac{E}{(1+\mu)(1-2\mu)}\begin{bmatrix}1-\mu & \mu & \mu & 0 & 0 & 0\\ \mu & 1-\mu & \mu & 0 & 0 & 0\\ \mu & \mu & 1-\mu & 0 & 0 & 0\\ 0 & 0 & 0 & \frac{1-2\mu}{2} & 0 & 0\\ 0 & 0 & 0 & 0 & \frac{1-2\mu}{2} & 0\\ 0 & 0 & 0 & 0 & 0 & \frac{1-2\mu}{2}\end{bmatrix}$$

where E and μ are the Young's modulus and Poisson's ratio, respectively. This is the standard matrix form of the constitutive relationship for a linear elastic material as described in many standard textbooks.

The total strains are related to the displacement via the following equation:

$$\varepsilon^{(tot)}=\mathbf{Ld} \tag{C.3}$$

where $\varepsilon^{(tot)}$ is the total strain and $\mathbf{d}=(u\ \ v\ \ w)^{\mathrm{T}}$ is the displacement vector representing the displacements in the x, y and z directions, respectively. The matrix L contains the differential operators and is given by:

$$\mathbf{L} = \begin{bmatrix} \frac{\partial}{\partial x} & 0 & 0 \\ 0 & \frac{\partial}{\partial y} & 0 \\ 0 & 0 & \frac{\partial}{\partial z} \\ \frac{\partial}{\partial y} & \frac{\partial}{\partial x} & 0 \\ \frac{\partial}{\partial z} & 0 & \frac{\partial}{\partial x} \\ 0 & \frac{\partial}{\partial z} & \frac{\partial}{\partial y} \end{bmatrix}$$

The constitutive equation states that the stresses are dependent on the elastic strains. These elastic strains are dependent on the total stain $\varepsilon^{(tot)}$, thermal strain $\varepsilon^{(th)}$, hygroscopic strain $\varepsilon^{(hy)}$ and plastic strain $\varepsilon^{(p)}$, therefore:

$$\varepsilon^{(e)} = \varepsilon^{(tot)} - \varepsilon^{(th)} - \varepsilon^{(hy)} - \varepsilon^{(p)} \tag{C.4}$$

Generally, the plastic strain is a function of the stress and the temperature. For simplicity, the plasticity effect is neglected here, i.e. $\varepsilon^{(p)} = 0$. The thermal strains are given by:

$$\varepsilon^{(th)} = \alpha \Delta T$$

where $\alpha = (\alpha_1, \alpha_2, \alpha_3, 0, 0, 0)$ is the vector of coefficients of thermal expansion and ΔT is the thermal load (the temperature change). The α_1, α_2 and α_3 represent the thermal expansion coefficients in *x*, *y* and *z* direction respectively, and the values for them are the same for an isotropic material but can be different for an anisotropic material.

Similarly, the hygroscopic strains are given by:

where n is the number of the Gauss points used in the approximation, w_i is the weight of the point in the sum and (s_i, t_i) represents the coordinates of each Gauss point.

The corresponding variable $f(x,y)$ in the global system can be calculated using:

$$I = \int f(x,y)dxdy = \int_{-1}^{1}\int_{-1}^{1} f(s,t)|J|dsdt = \sum_{i=1}^{n} w_i f(s_i,t_i)|J|_{(s_i,t_i)} \tag{C.5}$$

where $|J|$ is the determinant of the Jacobian matrix for the particular mesh element. In this way, the area integral is calculated in local co-ordinates using Gauss quadrature firstly and then transformed back to global coordinates using the Jacobian matrix. The weights and coordinates of Gaussian points on a quadrilateral are well defined and available in many standard textbooks [108].

Assuming a variable ϕ and its derivatives which could represent displacements, etc., can be approximated anywhere within a mesh element via:

$$\begin{gathered} \phi(s,t,u) = \sum_{i=1}^{m} N_i(s,t,u)\phi_i = \mathrm{N}\phi \\ \frac{\partial\phi(s,t,u)}{\partial k} = \sum_{i=1}^{m} \frac{\partial N_i(s,t,u)}{\partial k}\phi_i, \quad k = s,t,u \end{gathered} \tag{C.6}$$

where m is the number of nodes making up a mesh element and $N_i(s,t,u)$ is the shape function. For example, for bilinear quadrilaterals, these shape functions are:

$$\begin{aligned} N_1(s,t) &= 0.25(1+s)(1+t) \qquad & N_2(s,t) &= 0.25(1-s)(1+t) \\ N_3(s,t) &= 0.25(1-s)(1-t) \qquad & N_4(s,t) &= 0.25(1+s)(1-t) \end{aligned}$$

And for eight-node bricks, these shape functions are:

$$N_1(s,t,u)=0.125(1+s)(1+t)(1+u) \qquad N_2(s,t,u)=0.125(1-s)(1+t)(1+u)$$
$$N_3(s,t,u)=0.125(1-s)(1+t)(1-u) \qquad N_4(s,t,u)=0.125(1+s)(1+t)(1-u)$$
$$N_5(s,t,u)=0.125(1+s)(1-t)(1+u) \qquad N_6(s,t,u)=0.125(1-s)(1-t)(1+u)$$
$$N_7(s,t,u)=0.125(1-s)(1-t)(1-u) \qquad N_8(s,t,u)=0.125(1+s)(1-t)(1-u)$$

For the eight node brick mesh element, the displacement vector for ϕ is $\mathbf{d}=(u_1, v_1, w_1, ...u_8, v_8, w_8)^{\mathrm{T}}$. The shape function matrix **N** for the eight node brick element is given by:

$$\mathbf{N}=\begin{bmatrix} N_1 & 0 & 0 & N_2 & 0 & 0 & \ldots & N_8 & 0 & 0 \\ 0 & N_1 & 0 & 0 & N_2 & 0 & \ldots & 0 & N_8 & 0 \\ 0 & 0 & N_1 & 0 & 0 & N_2 & \ldots & 0 & 0 & N_8 \end{bmatrix}$$

For other mesh elements including triangles, wedges and tetrahedrals, different shape functions would apply.

The integrated form of the equilibrium equations will contain first-order derivatives of displacements which can be approximated in local coordinates by using Equation (C.6). To map these derivatives back to global coordinates the following transformation is used:

$$\begin{bmatrix} \frac{\partial N_i}{\partial x} \\ \frac{\partial N_i}{\partial y} \\ \frac{\partial N_i}{\partial z} \end{bmatrix} = \begin{bmatrix} \frac{\partial x}{\partial s} & \frac{\partial y}{\partial s} & \frac{\partial z}{\partial s} \\ \frac{\partial x}{\partial t} & \frac{\partial y}{\partial t} & \frac{\partial z}{\partial t} \\ \frac{\partial x}{\partial u} & \frac{\partial y}{\partial u} & \frac{\partial z}{\partial u} \end{bmatrix}^{-1} \begin{bmatrix} \frac{\partial N_i}{\partial s} \\ \frac{\partial N_i}{\partial t} \\ \frac{\partial N_i}{\partial u} \end{bmatrix}$$

where the 3×3 matrix above represents the Jacobian matrix $[J]$ for the mesh element. All entries in the Jacobian can be calculated using Equation (C.6). For example, at a specific point in the local coordinate system (s,t,u), the derivative of x with respect to s is:

$$\frac{\partial x}{\partial s}=\sum_{i=1}^{m}\frac{\partial N_i}{\partial s}X_i$$

where X_i are the x co-ordinates of the nodes of the corresponding mesh element in the global coordinate. Similar expressions can be obtained for the derivative of y with respect to t and the derivative of z to u.

C.1.3 Discretization of Equilibrium Equations

The equilibrium Equations (C.1) can also be expressed in tensor format as:

$$\frac{\partial \sigma_{ij}}{\partial x_j}=f_i$$

The finite element method integrates the above equations over the mesh elements and uses the approximations detailed above for the space and physical properties to transform the above partial differential equations into a set of algebraic equations which can be solved using matrix solvers and computers.

The Galerkin weighted residual procedure requires that the overall residual R_Ω, after substituting the approximations into the integral of the equilibrium equations, for the whole domain to be zero, i.e.

$$R_\Omega=\int_\Omega W\left(\frac{\partial \sigma_{ij}}{\partial x_j}-f_i\right)d\Omega=0 \qquad \text{(C.7)}$$

where W are the weighting functions and Ω is the volume of the domain. Considering the x-direction equilibrium equation in weighted residual form gives:

$$\int_\Omega W\left(\frac{\partial \sigma_{xx}}{\partial x}+\frac{\partial \sigma_{xy}}{\partial y}+\frac{\partial \sigma_{xz}}{\partial z}-f_x\right)d\Omega=0 \qquad \text{(C.8)}$$

Using the product rule of differentiation, the above integral for term σ_{xx} becomes

$$\int_{\Omega}\left(W\frac{\partial \sigma_{xx}}{\partial x}\right)d\Omega=\int_{\Omega}\frac{\partial\left(W\sigma_{xx}\right)}{\partial x}d\Omega-\int_{\Omega}\frac{\partial W}{\partial x}\sigma_{xx}d\Omega \tag{C.9}$$

In Equation (C.9), the divergence theorem is used to transform the integral equation by replacing the volume integrals with the corresponding integral over the boundary of the volume domain. If Γ devotes the boundary of the control volume Ω and the $\mathbf{n}=(n_x,n_y,n_z)$ is the outward normal vector at the boundary surface, then:

$$\int_{\Omega}\frac{\partial\left(W\sigma_{xx}\right)}{\partial x}d\Omega=\oint_{\Gamma}W\sigma_{xx}n_x d\Gamma$$

Similar expressions are obtained for the σ_{xy} , σ_{xz} terms. The following integral representation for the equilibrium equation in the x-direction can be reached.

$$-\int_{\Omega}\left(\frac{\partial W}{\partial x}\sigma_{xx}+\frac{\partial W}{\partial y}\sigma_{xy}+\frac{\partial W}{\partial z}\sigma_{xz}+Wf_x\right)d\Omega+\oint_{\Gamma}W\left(\sigma_{xx}n_x+\sigma_{xy}n_y+\sigma_{xz}n_z\right)d\Gamma=0$$

Therefore, the equilibrium Equation (C.7) can be written as:

$$-\int_{\Omega}\frac{\partial W}{\partial x}\sigma_{ij}d\Omega+\oint_{\Gamma}W\sigma_{ij}\cdot n_j d\Gamma=\int_{\Omega}Wf_i d\Omega$$

which in the matrix form is:

$$-\int_{\Omega}\mathbf{L}^{\mathrm{T}}\mathbf{W}\sigma d\Omega+\oint_{\Gamma}\mathbf{W}\sigma\cdot\mathbf{n}d\Gamma=\int_{\Omega}\mathbf{W}\mathbf{f}d\Omega \tag{C.10}$$

With respect to each mesh, and from Equation (C.2) and Equation (C.4), the stress can be expressed as a function of the total, thermal and hygroscopic strains:

$$\sigma=\mathbf{D}\left(\varepsilon^{(tot)}-\varepsilon^{(th)}-\varepsilon^{(hy)}\right) \tag{C.11}$$

If Equation (C.3) is used to substitute the total strain into Equation (C.11) and also take into account the relationship $\mathbf{d}=\mathbf{N}\mathbf{u}$ between the displacement vector at a point ($\mathbf{d}$) and the nodal displacement vector ($\mathbf{u}$), the following stress-displacement relationship in matrix form is derived:

$$\sigma = \mathbf{DLNu} - \mathbf{D}\varepsilon^{(th)} - \mathbf{D}\varepsilon^{(hy)}$$

If $\mathbf{B}=\mathbf{LN}$ and by substituting the stress in Equation (C.10) using the above relationship, it can be expressed in terms of the nodal displacement $\mathbf{u}$ for each mesh element control volume:

$$-\int_{\Omega}\mathbf{L}^{\mathrm{T}}\mathbf{W}\left(\mathbf{DBu}-\mathbf{D}\varepsilon^{(th)}-\mathbf{D}\varepsilon^{(hy)}\right)d\Omega+\oint_{\Gamma}\mathbf{W}\left(\mathbf{DBu}-\mathbf{D}\varepsilon^{(th)}-\mathbf{D}\varepsilon^{(hy)}\right)\cdot\mathbf{n}d\Gamma=\int_{\Omega}\mathbf{Wf}d\Omega$$

The Galerkin finite element approach takes the weighting functions $\mathbf{W}$ equal to the shape functions for the mesh element ($\mathbf{W}=\mathbf{N}^{\mathrm{T}}$) and zero elsewhere. For the internal adjacent mesh element the surface integral balances and does not contribute explicitly in the discretized equation for displacement. The surface integral contributes to the mesh element at the boundary of the domain. It is approximated by using the specified boundary conditions. The Galerkin finite element method expresses the discretized equation for an internal mesh element with volume V as:

$$-\int_{V}\mathbf{B}^{\mathrm{T}}\mathbf{DBu}dV=\int_{V}\mathbf{N}^{\mathrm{T}}\mathbf{f}dV-\int_{V}\mathbf{B}^{\mathrm{T}}\mathbf{D}\varepsilon^{(th)}dV-\int_{V}\mathbf{B}^{\mathrm{T}}\mathbf{D}\varepsilon^{(hy)}dV \qquad \text{(C.12)}$$

This equation represents the discretized form of equilibrium equations for a single element and can be written in the form:

$$\mathbf{A}^{\mathrm{e}}\mathbf{u}=\mathbf{b}^{\mathrm{e}}$$

The above volume integrals are calculated in local coordinates using Gauss quadrature and transformed back to global coordinates using the Jacobian matrix. Hence for $\mathbf{A}^{\mathrm{e}}$ we have:

$$-\int_V \mathbf{B}^{\mathrm{T}}\mathbf{D}\mathbf{B}\,dV = -\int_{-1}^{+1}\int_{-1}^{+1}\int_{-1}^{+1}\mathbf{B}^{\mathrm{T}}\mathbf{D}\mathbf{B}\,|J|\,dsdtdu$$

where $|J|$ is the determinant of the Jacobian matrix for this mesh element.

Boundary conditions are incorporated into the finite element procedure by reintroducing the surface integral into the formulation for the control volumes whose faces lie on the boundary of the domain. The following integral is added to the right side of Equation (C.12) to include boundary conditions in a general way.

$$-\int_\Gamma \mathbf{N}^{\mathrm{T}}\mathbf{D}\mathbf{B}\mathbf{u}\cdot\mathbf{n}\,d\Gamma$$

where Γ represents the boundary of domain. The boundary conditions can be in the form of prescribed displacement, force or pressure.

C.1.4 Solution Procedure

The contributions from each mesh element to each displacement degree of freedom i.e. (*u, v, w*) at each node are combined to form the following matrix system for the whole domain:

$$\mathbf{A}\mathbf{x} = \mathbf{b} \tag{C.13}$$

where **A** is a banded systems matrix, containing the coefficients relating each degree of freedom. $\mathbf{x} = (u_1, v_1, w_1, \ldots\ldots, u_n, v_n, w_n)^{\mathrm{T}}$ is the vector containing all degrees of freedom and **b** represents the source terms.

In FEM, Equation (C.13) is obtained by assembling contributions from all the elements, where:

$$\mathbf{A} = \sum_{ele=1}^{totele}\left[\int_V -\mathbf{B}^{\mathrm{T}}\mathbf{D}\mathbf{B}\,dV\right]_{ele}$$

$$\mathbf{b} = \sum_{ele=1}^{totele} \left[\int_{v} \mathbf{N}^{\mathrm{T}} \mathbf{f}\, dV - \int_{V} \mathrm{B}^{\mathrm{T}} \mathbf{D} \varepsilon^{(th)}\, dV - \int_{V} \mathbf{B}^{\mathrm{T}} \mathbf{D} \varepsilon^{(hy)}\, dV \right]_{ele} - \int_{\Gamma} \mathbf{N}^{\mathrm{T}} \mathbf{DBu} \cdot \mathbf{n}\, d\Gamma \quad \text{(C.14)}$$

where *toele* is the total number of mesh elements and the *sum* indicates the assembling contributions from all elements.

The Equation (C.13) represents the final sets of discretised equations that results from the finite element discretisation of the equilibrium equations. This linear system of equations can be solved by matrix solvers. The variables being solved at this stage are the components of displacement in the x, y, and z directions. These are solved at the nodal locations. After this the equations for strain and stress are solved usually at the gauss points within each element.

C.2 Elasto Visco-Plasticity

The finite element method has been used for a number of years to solve plastic material behaviour. This section describes the numerical procedure used to solve elastic visco-plastic material behaviour. This is a rate dependent material behaviour model, which can also recover the rate-independent elasto-plastic model as solution time approaches infinity [151].

C.2.1 Elasto-Viscoplasticity Material Model

The basic physical features of the elasto-viscoplastic model can be introduced by means of a one dimensional mechanical system as depicted in Figure C.3. The system consists of a spring with elastic properties, serially coupled to a friction slider and a dashpot, which comprise the viscoplastic contribution. The friction slider is inactive if the stress is below the yield point, resulting in no viscoplastic deformation. The dashpot reflects the viscous properties of viscoplasticity when the slider is active. The total deformation then consists of the elastic displacement in the spring plus the displacement of the viscous dashpot.

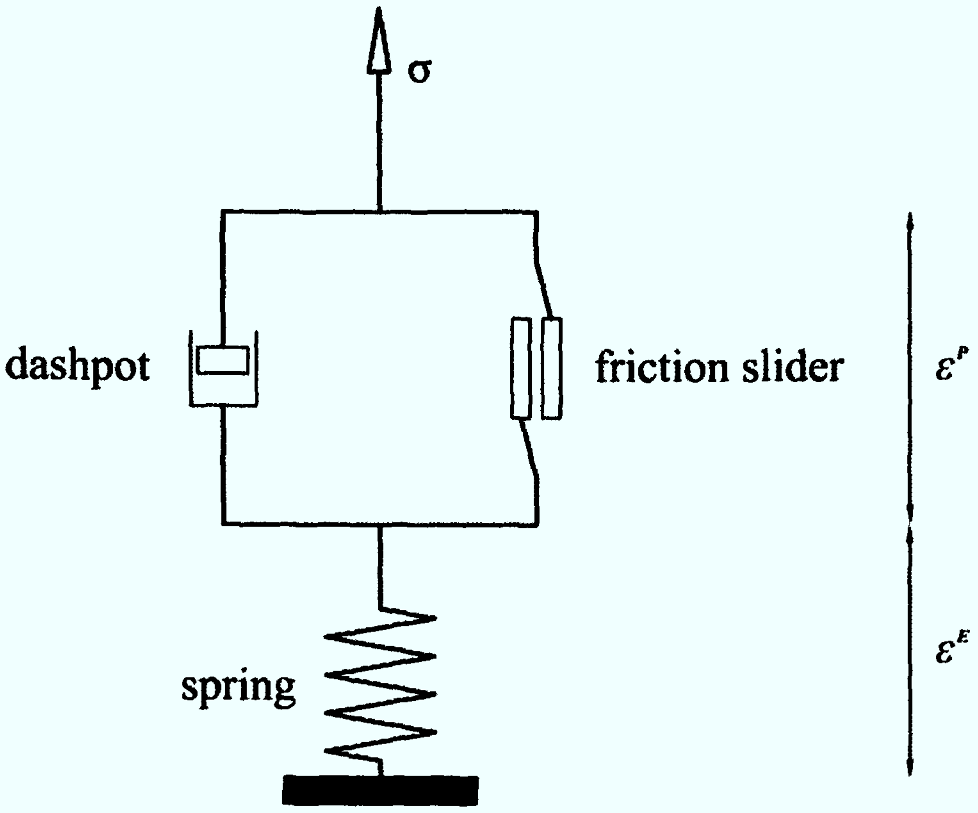

Figure C.3: Sketch of a mechanical model that reflects the basic physics of elasto-viscoplastic deformation

Equilibrium of any part of the structure implies that the sum of the normal stresses is σ every where. The onset of viscoplastic deformation occurs when $\sigma = C_Y$, where C_Y is the yield stress. For $\sigma < C_Y$ the deformation is purely elastic, whereas for $\sigma \geq C_Y$, the material is in a combined elasto-viscoplastic state. The friction slider develops an internal stress:

$$\sigma^P = \begin{cases} C_Y, \sigma \geq C_Y \\ \sigma, \ \ \sigma < C_Y \end{cases}$$

When the friction slider is active ($\sigma > C_Y$), the dashpot experiences a stress $\sigma^D = \sigma - \sigma^P$, which is related to the viscoplastic strain rate $\dot{\varepsilon}^P$ by the constitutive relation $\sigma^D = \mu\dot{\varepsilon}^P$, in analogy with viscous fluid flow, μ is a viscosity coefficient.

The constitutive law for the viscoplastic part of structure can be expressed as:

$$\dot{\varepsilon}^P = \langle \Phi(F) \rangle \frac{1}{\mu} \sigma^D$$

where $F = \sigma - C_Y$, the notation $\langle \Phi(F) \rangle = \begin{cases} \Phi(F), F > 0 \\ 0, F \le 0 \end{cases}$

Therefore, the relationship between the total stress and strain in the two cases can be developed. In the purely elastic case, $\sigma < C_Y$ and $\varepsilon^P = 0$, we get:

$$\sigma = E\varepsilon$$

Whereas, $\dot{\varepsilon}^P = \frac{1}{E}\dot{\sigma} + \gamma\left(\sigma - C_Y(\varepsilon^P)\right)$

where $\gamma = 1/\mu$ is the material property fluidity. C_Y is treated as a function of the total viscoplastic strain ε^P when considering the stain hardening behaviour of the material.

C.2.2 Three Dimensional Elasto-Viscoplastic Model

The fundamental assumption of elasto-viscoplasticity is that the total deformation can be separated into elastic and viscoplastic parts. More specifically, one can express the total rate of strain $\dot{\varepsilon}$, according to:

$$\dot{\varepsilon} = \dot{\varepsilon}^E + \dot{\varepsilon}^P \tag{C.15}$$

where $\dot{\varepsilon}^P$ is the viscoplastic strain rate, and $\dot{\varepsilon}^E$ is the elastic strain rate. The strain rate is related to the stress through the time-differentiated version of Hook's generalized law,

$$\dot{\sigma} = D\dot{\varepsilon}^E \tag{C.16}$$

The constitutive law for the viscoplastic strains can be written as:

$$\dot{\varepsilon}^P = \gamma \langle \Phi(F) \rangle \frac{\partial Q}{\partial \sigma} \qquad \text{(C.17)}$$

where $F = f(\sigma_{ij} - C_Y)$, Q is the plastic potential, the common case of associated plasticity corresponds to taking $Q = F$. A widespread choice of the $\Phi(F)$ is $\Phi(F) = (F/C_Y)^N$ for some prescribed constant N.

In elastic case, we have:

$$\int_{\Omega} B_i^T \sigma \, d\Omega + f_i = 0, \qquad i = 1, \ldots, n \qquad \text{(C.18)}$$

where f_i contains body forces and surface integrals of the tractions. The relation between the total stain and the displacement field is expressed in the following time differentiated and spatially discrete form:

$$\dot{\varepsilon} = \sum_{j=1}^{n} B_j \dot{u}_j \qquad \text{(C.19)}$$

The quantities like B_j, u_j and D can be recalled from the elastic analysis.

In the elasticity problem, the stress and strain quantities can be easily eliminated to obtain a vector equation for the displacement field. This is more complicated in the present elasto-viscoplastic problem, because of the nonlinearities introduced by the $\dot{\varepsilon}$ term. By proper discretizations, an iterative procedure can be derived where a linear system is solved with respect to the displacement field. In its simplest form, the linear system appearing in this numerical method has a coefficient matrix identical to that of the elasticity problem.

Combining Equation (C.15), Equation (C.16) and Equation (C.19) yields:

$$\dot{\sigma} - D\left(\sum_j B_j \dot{u}_j - \dot{\varepsilon}^P \right) = 0 \qquad \text{(C.20)}$$

Since $\dot{\varepsilon}^P$ depends nonlinearly on σ, making the above equation a nonlinear ordinary differential equation for σ. Hence, we can not eliminate σ and must work with essentially two types of spatially discrete equations governing σ and u_j, using Equation (C.18) and Equation (C.20).

In Equation (C.20), the time derivatives can be approximated by a θ-rule [151]. Depending on the value taken we obtain an explicit or implicit formulation.

$$\frac{\Delta\sigma}{\Delta t}-D\sum_{j=1}^{n}B_j\frac{\Delta u_j}{\Delta t}+D\theta\dot{\varepsilon}^{P,l}+D(1-\theta)\dot{\varepsilon}^{P,l-1}=0$$

where the notation $\Delta\sigma\equiv\sigma^l-\sigma^{l-1}$, $\Delta u_j\equiv u_j^{\,l}-u_j^{\,l-1}$,.

Utilizing these approximations in Equation (C.18) and Equation (C.20) gives the following nonlinear discrete problem:

$$\int_\Omega B_i^T\sigma^l d\Omega+f_i^l=0, \qquad i=1,\ldots,n$$

$$\Delta\sigma-D\sum_{j}^{n}B_j\Delta u_j+\Delta tD\theta\dot{\varepsilon}^{P,l}+\Delta tD(1-\theta)\dot{\varepsilon}^{P,l-1}=0$$

C.2.3 A Newon-Raphson-Based Iteration Method

The above nonlinear problem can be solved using a Newon-Raphson procedure, and the nature of the resulting approximations enables us to eliminate $\Delta\sigma$ and derive a linear system for $\Delta u_j (j=1,\ldots,n)$. For example, if we define:

$$\Psi_i^l\equiv\int_\Omega B_i^T\sigma^l d\Omega+f_i^l, \qquad \text{(C.21)}$$

$$R^l\equiv\Delta\sigma-D\sum_{j}B_j\Delta u_j+\Delta tD\theta\dot{\varepsilon}^{P,l}+\Delta tD(1-\theta)\dot{\varepsilon}^{P,l-1} \qquad \text{(C.22)}$$

And then consider $\Psi_i^l = 0$ and $R^l = 0$ as a simultaneous nonlinear system of algebraic equations for σ^l, and u^l, $i = 1,..,n$. A Newton-Raphson approach consists in making first-order Taylor-series expansions of Ψ_i^l and R^l around an approximation $\sigma^{l,k}$, $u^{l,k}$ in iteration k. Enforcing the linear Taylor-series expansion to vanish results in linear equations for the increments $\delta\sigma^{l,k+1}$, $\delta u^{l,k+1}$:

$$\Psi_i^{l,k+1} \approx \Psi_i^{l,k} + \int_\Omega B_i^T \delta\sigma^{l,k+1} d\Omega = 0 \tag{C.23}$$

$$\begin{aligned} R^{l,k+1} &\approx R^{l,k} + \left(\frac{\partial R}{\partial \sigma^l}\right)^{l,k} \delta\sigma^{l,k+1} + \sum_{j=1}^{n} \left(\frac{\partial R}{\partial u_j^l}\right)^{l,k} \delta u_j^{l,k+1} \\ &= R^{l,k} + \delta\sigma^{l,k+1} - D\sum_{j=1}^{n} B_j \delta u_j^{l,k+1} + \Delta t D\theta C\delta\sigma^{l,k+1} = 0 \end{aligned} \tag{C.24}$$

with $C = \left(\dfrac{\partial \dot{\varepsilon}^P}{\partial \sigma}\right)^{l,k}$.

Equation (C.24) can be solved with respect to the stress increment, resulting in:

$$\delta\sigma^{l,k+1} = \hat{D}\sum_j B_j \delta u_j^{l,k+1} - QR^{l,k} \tag{C.25}$$

where $\hat{D} = (D^{-1} + \theta\Delta t C)^{-1}$, $Q = (I + \theta\Delta t DC)^{-1}$.

Inserting this $\delta\sigma^{l,k+1}$ in Equation (C.23) yields a linear system for $\delta u_j^{l,k+1}$:

$$\sum_j \left(\int_\Omega B_i^T \hat{D} B_j d\Omega \right) \delta u_j^{l,k+1} = \int_\Omega B_i^T Q R^{l,k} d\Omega - \Psi_i^{l,k}$$

At time $t = 0$, $\dot{\varepsilon}^{P,0} = 0$, and the stresses correspond to a purely elastic state. That is, u^0 is determined from a standard elasticity problem:

$$\sum_j \left(\int_\Omega B_i^T \hat{D} B_j \, d\Omega \right) u_j^0 = -f_i^0, \qquad i = 1, \ldots, n.$$

With the associated stresses $\sigma^0 = D \sum_j B_j u_j^0$. Suppose u^{l-1}, σ^{l-1} and $\dot{\varepsilon}^{P,l-1}$ are known. New displacements u^l are generally computed by an iteration procedure. As an initial guess for the iterations, we set $u_j^{l,0} = u_j^{l-1}$, $\sigma_j^{l,0} = \sigma_j^{l-1}$, $\dot{\varepsilon}_j^{P,l,0} = \dot{\varepsilon}_j^{P,l-1}$. For k = 0, 1…, until convergence of the Newton-Raphson method, to assemble and solve the linear system for the correction $\delta u_j^{l,k+1}$ of the displacement field. And then calculate the displacements and stresses according to:

$$\begin{aligned} \sigma^{l,k+1} &= \sigma^{l,k} + \delta\sigma^{l,k+1} \\ u^{l,k+1} &= u^{l,k} + \delta u^{l,k+1} \end{aligned}$$

where $\delta\sigma^{l,k+1}$ can be found from Equation (C.25).

The final step is to calculate the new viscoplastic strain rate from the following equation and then proceed with the next iteration.

$$\dot{\varepsilon}^{P,l,k+1} = \gamma \left\langle \Phi\left(F(\sigma_{i,j}^{l,k+1}) \right) \right\rangle \left(\frac{\partial F}{\partial \sigma} \right)^{l,k+1}$$

If the iterative procedure converges in m iterations, we can define u^{l-m} as the converged solution u^l at this time level.

The calculation of the viscoplastic strain increment can be explicit or implicit. If the method is implicit then the latest values of stress will change the viscoplastic strain increment, and possibly the matrix system, requiring an iterative procedure at each increment. If the procedure is explicit, then the viscoplastic strain increment will be based on the values of stress at the previous step. For example, the explicit approximation at time step l+1 is given by:

$$\Delta\varepsilon^{p}_{l+1} = \Delta t\left(\frac{\partial \varepsilon^{p}}{\partial t}\right)_{l}$$

where t is the time step and the viscoplastic strain rate is approximated using values of stress etc., obtained from the previous step. The use of an explicit will require very small time steps [150].

D. PHYSICA - A Simulation Tool

PHYSICA [152] is a software environment for the modelling and analysis of multi-physics phenomena where material may behave as a solid or fluid during its processing. This analysis tool is a collection of interacting solution procedures, including CFD finite volume (FV) based techniques for heat transfer, fluid flow and Finite Element (FE) based elasto-visco-plastic solid mechanics. A numerical modelling tool such as PHYSICA is used in three stages, which are:

- Pre-processing
- Solution
- Post-processing

At the pre-processing stage, the geometry to be analysed will be generated in the computer using a suitable computer aided design (CAD) package. Boundary conditions and suitable properties for the materials in the domain will then be applied to the geometry. Finally, the domain will be broken down into a mesh over which the governing equations are solved. PHYSICA is linked to a software package called FEMGV [153] which is used as the pre-processor and post-processor and this environment has been used in this research.

In the solution stage, the design engineer will inform the programme on the relevant physics to solve, and then the software will check to ensure that all the relevant data including boundary conditions, material properties etc., have bee provided and that the quality of the mesh is suitable for the solution to take plac Matrix solvers will then be used to solve the algebraic equations, resulting from th discretisation process, for variables such as fluid velocities, temperature and soli displacements.

In the post-processing stage, FEMVIEW which is integrated with the softwar package FEMGV, will be used for post-processing and visualization of the simulatio results. There are some options for presenting the result data including vector plots plots of displaced shape of the design, contour plots of the solved quantity etc. T achieve accurate results from a simulation may require further analysis using a fine mesh to ensure that the results are mesh independent.

E. Liquid Crystal Display: A Case Study Using PHYSICA

This section describes the modelling process and results obtained from the analysi of the behaviour of a Liquid Crystal Display (LCD) that was packaged for use in hars environments. The packaging processes used adhesive materials and their effect on th reliability and performance of the LCD was analysed.

The core of the LCD package is an Active Matrix Liquid Crystal Displa (AMLCD) which needs to be protected from severe environments. The ruggedisatio or packaging process consists of laminating the LCD with cover glasses. This provide a more robust structure. The top view of the final LCD package is showed in Figur E.1.

A section view of this laminated LCD package is shown in Figure E.2, where th structure and materials involved are described. There is a very thin layer of Liqui Crystal which is sealed between the two AMLCD glasses. The material in yello represents the silicon resin which is soft and easily to be deformed, and thus it can b used for protecting the LCD package from external forces and also releasing the buil

E.1 Problem Description

When used in service this ruggedised display will experience extremes of temperature both hot and cold. When passed through qualification the display design will have to withstand the stress imposed due to temperature cycling. As the materials all have different coefficients of thermal expansion, each material will tend to expand by a different amount and this will result in stress.

A certain degree of stress within the LCD structure is of course allowed but too much stress can affect the structural integrity of the display and its performance. A concern from the industrial partner on this project was the stresses around the interfaces and joint materials. Computer modelling was suggested as a means to predict these stresses and to investigate how changes to design variables such as the material properties of the filled silicon resin and its thickness could affect these stresses.

E.2 Geometry and Computational Mesh

The geometry details are summarized in Table E.1. In order to study the effect of the thickness of the silicone resin, two models were built. Due to the symmetry in the LCD package, only a one-eighth model of the whole domain is used in the analysis. This reduces the amount of computing time required in the analysis. Once the package geometry and all the model components are parametrically defined, they are automatically meshed. In this model a totally of 22858 elements were generated and this resulted in mesh independent results. The mesh details of the model are shown in Figure E.3.

A temperature load from 25°C to 100°C was applied to the whole domain. Th properties of all the materials are listed in Table E.2. All the material was considere as elastic material, isotropic and homogeneous. The temperature dependent materia properties were not considered in this analysis due to lack of data.

Table E.2: The basic material information

	Young's Modulus E (GPa)	CTE (ppm/°C)	Poisson's Ratio
Borosilicate Glass	67.6	4.6	0.28
AMLCD Glass	67.6	4.6	0.28
Silicone Resin (soft gel)	0.001	350	0.3
Silicone Resin (firm gel)	0.1	300	0.3
Silicone Perimeter Seal	0.1	300	0.3
Liquid Crystal	0.001	200	0.3
LCD Perimeter Seal	20	70	0.3
CAB Polarizer Film	1.0	140	0.3

E.4 Solution of the Modelling Analysis

There are two data files need to be edited before doing the modelling analysis ir PHYSICA. One is the geometry file (*.geo) which includes all the geometry and mesl information, the index and location of the material and boundary conditions.

Another file needs to be edited is the "Inform" file, in which the values of the material properties and boundary conditions, having the same index number as the geometry file, are defined. There are several modules that are used for differen applications such as the Heat Module, EVP module etc. Different numerical solver based on iterative methods are available in PHYSICA, such as the over relaxed form

References

[1] Lau, J.H. (2000), *Low Cost Flip Chip Technologies for DCA, WLCSP, and PBGA Assemblies*, Published by McGraw Hill, ISBN: 0-07-135141-8, pp1-17.

[2] Tummala, R.R. (2006), Moore's Law Meets Its Match Continued, http://www.spectrum.ieee. org/jun06/3649.

[3] Ulrich, R.K. and Brown, W.D. (2006), *Advanced Electronic Packaging*, published by John Wiley & Sons, Inc. ISBN: 13978-0-471-46609-X, pp.1-28.

[4] Liu, J. (1999), *Conductive Adhesives for Electronics Packaging*, Electrochemical Publications Ltd, Port Erin, Isle of Man, ISBN 0901-150-37-1, pp.1-14.

[5] Liu, J. (1999), *Conductive Adhesives for Electronics Packaging*, Electrochemical Publications Ltd, Port Erin, Isle of Man, ISBN 0901-150-37- 1, pp.234-248.

[6] Charles, A.H. (1997), *Electronic Packaging & Interconnection Handbook*, Published by McGraw-Hill, ISBN: 0-07-26694-8.

[7] Teh, L.K., Teo, M., Anto, E., Wong, C.C., Mhaisalkar, S.G., Teo, P.S. and Wong, E.H. (2005), "Moisture-Induced Failures of Adhesive Flip Chip Interconnects", IEEE Trans on Components and Packaging Technologies, Vol.28, No.3, pp.506-516.

[8] Ferguson, T.P. and Qu, J.M. (2004), "Moisture and Temperature Effects on the Reliability of Interfacial Adhesion of a Polymer/Metal Interface", Proceedings of the 54th IEEE Electronic Components and Technology Conference (ECTC), Las Vegas, pp.1752-1758.

[9] Tan, C.W., Chan, Y.C. and Yeung, N.H. (2003), "Effect of Autoclave Test on Anisotropic Conductive Joints", Journal of Microelectronics Reliability, Vol.43, Issue: 2, pp.279-285.

[10] Caers, J.F.J.M., Zhao, X.J., Lekens, G., Dreesen, R., Croes, K. and Wong, E.H. (2003), "Moisture Induced Failures in Flip Chip on Flex Interconnections using Anisotropic Conductive Adhesives", Proceedings of International IEEE Conference on the Business of Electronic Product Reliability and Liability, Hong Kong & ShenZhen, pp.171-176.

[11] Wei, Z, Waf, L.S., Loo, N.Y., Koon, E.M. and Huang, M. (2002), "Studies on Moisture-induced Failures in ACF Interconnection", Proceedings of the 7th Electronics Packaging Technology Conference (EPTC), pp.133-138.

[12] Mercodo, L.L., White, J., Sarihan, V. and Lee, T.Y.T. (2003), "Failure Mechanism Study of Anisotropic Conductive Film (ACF) Packages", IEEE Transactions on Components and Packaging Technologies, Vol.26, No.3, pp.509-516.

[13] Kim, W.K., Ikeda, T. and Miyazaki, N. (2004), "Mechanical Reliability of Anisotropic Conductive Adhesive Films under Moisture/Reflow Sensitivity Test", WCCM VI in conjunction with APCOM'04, Beijing, China, pp.501-510.

[14] Kristiansen, H. and Liu, J. (1998), "Overview of Conductive Adhesive Interconnection Technologies for LCD's", IEEE Transactions on Components, Packaging, and Manufacturing Technology, Part A, Vol.21, No.2, pp.208-214.

[15] Lee, K.K., Ng, K.T., Tan, C.W.; Chan Y.C. and Cheng L.M. (2004), "Fabrication of Smart Card Using UV Curable Anisotropic Conductive Adhesive (ACA.) Part I: Optimization of the Curing Conditions", Proceedings of International Conference on Business of Electronic Product Reliability and Liability, Portland, Oregon, USA, pp.134-139.

[16] Lee, K.K., Tan, C.W. and Chan, Y.C. (2005), "Investigation of Conductive Bonding Using UV Curable Anisotropic Conductive Adhesives at Different Curing Conditions", Journal of Electronic Packaging, Transaction of ASME, pp.52-58.

[17] Tan, C.W., Siu, Y.M., Lee, K.K., Chan, Y.C. and Cheng, L.M. (2004), "Fabrication of Smart Card Using UV Curable Anisotropic Conductive Adhesive (ACA) Part II: Reliability Performance of the ACA joints", 2004 International Conference on Business of Electronic Product Reliability and Liability, Portland, Oregon, USA, pp.140-144.

[18] Zhang, J.H., Chan, Y.C., Zeng, Z.M. and Chiu, Y.W. (2002), "Research on the Interfacial Reaction between Anisotropically Conductive Film and Bumpless Die", Proceedings of the 52nd Conference on Electronic Components and Technology (ECTC), San Diego, USA, pp.1569-1574.

[19] Ogunjimi, A.O., Boyle, O.A., Whalley, D.C. and Williams, D.J. (1992), "A Review of the Impact of Conductive Adhesive Technology on Interconnection", Journal of Electronic Manufacturing, Vol.2, No.3, pp.109-118.

[20] Chang, W.K. and Chan, Y.C. (2005), "Reliability of Anisotropic Conductive Film Joints Using Bumpless Chip—Influence of Reflow Soldering and Environmental Testing", ASME Journal of Electronic Packaging, Vol.127, pp.113-119.

[21] Frisk, L. and Ristolainen, E. (2005), "Flip Chip Attachment on Flexible LCP Substrate Using an ACF", Journal of Microelectronics and Reliability, Vol.45, Issues 3-4, pp.583-588.

[22] Paik, K.W., Yim M.J. and Jay, Y.D. (2000), "Flip Chip Assembly on Organic Boards Using Anisotropic Conductive Adhesives (ACAs) and Ni/Au Bumps", Proceedings of the 50th IEEE Electronic Components and Technology Conference (ECTC), pp.378-384.

[23] Yim, M.J., Jeon, Y.D. and Paik, K.W. (2000), "Reduced Thermal Strain in Flip Chip Assembly on Organic Substrate using Low CTE Anisotropic Conductive Film", IEEE Transactions on Electronics Packaging Manufacturing, Vol.23, No.3, pp.171-176.

[24] Yim, M.J., Hwang, J.S. and Kim, JG. (2004), "Anisotropic Conductive Adhesives with Enhanced Thermal Conductivity for Flip-Chip Applications", Proceedings of the 54th IEEE Electronic Components and Technology Conference (ECTC), pp.159-164.

[25] Pataki, W.S. (1997), "Optimization of Free Radical Initiation Reactions in the Electrical Industry", Proceedings of the Electrical Insulation Conference and Electrical Manufacturing and Coil Winding Conference, pp.745–751.

[26] Jacob, J., Chia, L.H.L. and Boey, F.Y.C. (1995), "Comparative Study of Methyl Methacrylate Cure by Microwave Radiation Versus Thermal Energy", Polymer Testing, Vol.14, No.4, pp.343-354.

[27] Davis, C., Tanikella, R., Sung, T., Kohl, P. and May, G. (2003), "Optimization of Variable Frequency Microwave Curing Using Neural Networks and Genetic Algorithms", Proceedings of the 53rd IEEE Electronic Components and Technology Conference, pp.1718-1723.

[28] Fu, Y., Wang, T. and Liu, J. (2003), "Microwave-transmission, Heat and Temperature Properties of Electrically Conductive Adhesive", IEEE Transactions on Components and Packaging Technologies, Part A, Vol.26, Issue: 1, pp.193-198.

[29] Islam, R.A. and Chan, Y.C. (2004), "Effect of Microwave Preheating on the Bonding Performance of flip chip on flex joint", Journal of Microelectronics Reliability, Vol.44, Issue 5, pp.815-821.

[30] Wang, T.B., Fu, Y., Becher, M. and Liu, J. (2001), "Microwave Cure of Metal-Filled Electrically Conductive Adhesive", Proceedings of the 51st IEEE Electronic Component Technology Conferenc (ECTC), Orlando, USA, pp.593-597.

[31] Shiming, L. and Liu, J. (2002), "Development and Characterization of Single Mode Microwave Cured Adhesives for Electronics Packaging Application", Proceedings of 52nd IEEE Electronic Components and Technology Conference (ECTC), pp.1147-1150.

[32] Chang, S.M., Jou, J.H., Hsieh, A., Chen, T.H., Chang, C.Y., Wang, Y.H. and Huang, C.M. (2001), "Characteristic Study of Anisotropic Conductive Film for Chip-on-film Packaging", Journal of Microelectronics Reliability, Vol.41, Issue 12, pp.2001-2009.

[33] Chan, Y.C. and Luk, D.Y. (2002), "Effects of Bonding Parameters on the Reliability Performance of Anisotropic Conductive Adhesive Interconnects for Flip-chip-on-flex Packages Assembly I. Different Bonding Temperature", Journal of Microelectronics Reliability, Vol.42, Issue: 8, pp.1185-1194.

[34] Chan, Y.C. and Luk, D.Y. (2002), "Effects of Bonding Parameters on the Reliability Performance of Anisotropic Conductive Adhesive Interconnects for Flip-chip-on-flex Packages Assembly II Different Bonding Pressure", Journal of Microelectronics Reliability, Vol.42, Issue 8, pp.1195-1204.

[35] Chen, X., Zhang, J., Jiao C.L., Liu, Y.M. (2006), "Effects of Different Bonding Parameters on the Electrical Performance and Peeling Strengths of ACF Interconnection", Journal of Microelectronics Reliability, Vol.46, pp.774–785.

[36] Uddin, M.A., Alam, M.O., Chan, Y.C. and Chan, H.P. (2004), "Adhesion Strength and Contact Resistance of Flip Chip on Flex Packages—Effect of Curing Degree of Anisotropic Conductive Film", Journal of Microelectronics Reliability, Vol.44, Issue: 3, pp.505-514.

[37] Tan, S.C., Chan, Y.C., Chiu, Y.W. and Tan, C.W. (2004), "Thermal Stability Performance of Anisotropic Conductive Film at Different Bonding Temperatures", Journal of Microelectronics Reliability, Vol. 44, Issue: 3, pp.495-503.

[38] Cao, L.Q., Lai, Z.H. and Liu, J (2005), "Interfacial Adhesion of Anisotropic Conductive Adhesives on Polyimide Substrate", ASME Journal of Electronic Packaging, Vol.127, pp.43-46.

[39] Vries, J.D., Delft, J.V., Slob, C. (2005), "100μm Pitch Flip Chip on Foil Assemblies with Adhesive Interconnections", Journal of Microelectronics Reliability, Vol.45, pp.527–534.

[40] Lam, D.C.C., Yang, F. and Tong, P. (1999), "Chemical Kinetic Model of Interfacial Degradation of Adhesive Joints", IEEE Transactions on Components and Packaging Technology, Vol.22, No.2, pp.215-220.

[41] Kwon, W.S., Yim, M.J., Paik, K.W., Ham, S.J. and Lee, S.B. (2005), "Thermal Cycling Reliability and Delamination of Anisotropic Conductive Adhesives Flip Chip on Organic Substrates with Emphasis on the Thermal Deformation", ASME Journal of Electronic Packaging, Vol.127, pp.86-90.

[42] Ali, L., Chan, Y.C. and Alam M.O. (2005), "The Effect of Thermal Cycling on the Contact Resistance of Anisotropic Conductive Joints", Journal of Soldering and Surface Mount Technology, Vol.17, No.3, pp.20-31.

[43] Palm, P., Määttänen, J., Tuominen, A., Ristolainen, E. (2001), "Reliability of 80μm Pitch Flip Chip Attachment on Flex", Journal of Microelectronic Reliability, Vol.41, pp.633-638.

[44] Vries, J.D. (2004), "Failure Mechanism of Anisotropic Conductive Adhesive Interconnections in Flip Chip ICs on Flexible Substrates", IEEE Transactions on Components and Packaging Technologies, Vol. 27, No.1, pp.161-166.

[45] Veris, J.D., Delft, J.V. and Slob, K., (2005), "SMT- Compatibility of Adhesive Flip Chip on Foil Interconnections with 40-μm Pitch" IEEE Transactions on Components and Packaging Technologies, Vol.28, No.3, 2005, pp.499-505.

[46] Wu, Y.P., Alam, M.O., Chan, Y.C. and Wu, B.Y. (2004), "Dynamic Strength of Anisotropic Conductive Joints in Flip Chip on Glass and Flip Chip on Flex Packages", Journal of Microelectronics Reliability, Vol.44, Issue: 2, pp.295-302.

[47] Tan, C.W., Chan, Y.C. and Yeung, N.H. (2003), "Behaviour of Anisotropic Conductive Joints under Mechanical Loading", Journal of Microelectronics Reliability, Vol.43, Issue: 3, pp.481-486.

[48] Rizvi, M.J., Chan, Y.C., Bailey, C. and Lu, H. (2005), "Study of Anisotropic Conductive Adhesive Joint Behaviour Under 3-point Bending", Journal of Microelectronics Reliability, Vol.45, Issues: 3-4, pp.589-596.

[49] Kim, J.W., Jung, S.B. (2006), "Effects of Bonding Pressure on the Thermo-Mechanical Reliability of ACF Interconnection", Journal of Microelectronic Engineering, dio:10.1016/j.mee.2006.10.029.

[50] Reports from International Technology Roadmap for Semiconductors (ITRS) (2005 edition), www.itrs.org

[51] Whalley, D.C., Chen, L. and Liu, J. (2001), "Modelling of the Anisotropic Adhesive Assembly Process", Proceedings of the Fourth International Symposium on Electronic Packaging Technology, Beijing, pp.319-324.

[52] Ogunjimi, A.O., Mannan, S.H., Whalley, D.C. and Williams D.J. (1995), "The Assembly Process for Anisotropic Conductive Joints Some New Experimental and Theoretical Results", Journal of Electronic Manufacturing, Vol.5, pp.263-272.

[53] Mannan, S.H., Whalley, D.C., Ogunjimi, A.O. and Williams, D.J. (1995), "Modelling of the Initial Stages of the Anisotropic Adhesive Joint Assembly Process", Proceeding of the 17th Japan IEEE IEMTS, Omiya, pp.142-145.

[54] Dudek, R., Meinel, S., Schubert, S., Michel, B., Dorfmüller, L., Knoll, P.M. and Baumbach, J. (1999), "Flow Characterization and Thermo-mechanical Response of Anisotropic Conductive Films", IEEE Transactions on Components and Packaging Technology, Vol.22, pp.177-185.

[55] Mannan, S.H., Whalley, D.C., Ogunjimi, A.O. and Williams, D.J. (1996), "Assembly of the Planar Array Components using Anisotropic Conducting Adhesives- a Benchmark Study: Part II Theory", IEEE Transactions on Components, Packaging and Manufacturing Technology -Part C, Vol.19, pp.264-269.

[56] Whalley, D.C., Glinsky, G., Bailey, C. and Liu, J. (2001), "Computational Modelling of the Anisotropic Conductive Adhesive Assembly Process", Proceeding of the 3rd International Symposium on Electronics Materials and Packaging, Jeju, Korea.

[57] Liu, J. (2000), "ACA Bonding Technology for Low Cost Electronics Packaging Applications- Current Status and Remaining Challenges", Proceedings of the 4th IEEE International Conference on Adhesive Joining and Coating Technology in Electronics Manufacturing. Espoo, Finland, pp.1-15.

[58] Buratynski, E.K. (1993), "Thermo-mechanical Modelling of Direct Chip Interconnection Assembly", Journal of Electronic Packaging, Vol.115, pp.382-391.

[59] Wu, S.X., Hu, K.X. and Yeh, C.P. (1999), "Contact Reliability Modelling and Material Behaviour of Conductive Adhesive under Thermo-mechanical Loads", Chapter 6 in Conductive Adhesive for Electronics Packaging, edited by Johan Liu, Electrochemical Publications Ltd, (Port Erin, Isle of Ma n, UK).

[60] Pinardi, K., Lai, Z.H., Vogel, D., Kang, Y.L., Liu, J., Liu, S., Haug R. and Willander, M. (2000), "Effect of Bump Height on the Strain Variation during the Thermal Cycling Test

of ACA Flip- Chip Joints", IEEE Transactions on Components and Packaging Technologies, Vol.23, No.3, pp.447- 451.

[61] Wu, C.M.L., Liu, J. and Yeung, N.H. (2001), "The Effects of Bump Height on the Reliability of ACF in Flip-Chip", Journal of Soldering and Surface Mount Technology, Vol.13, pp.25-30.

[62] Yeung, N.H., Chan, Y.C., and Tan, C.W. (2003), "Effect of Bonding Force on the Conducting Particle with Different Sizes", Journal of Electronic Packaging, Vol.125, No.4, pp.624-629.

[63] Williams, D.J. and Whalley, D.C. (1993), "The Effects of Conducting Particles Distribution on the Behaviour of Anisotropic Conducting Adhesives- Non Uniform Conductivity and Shorting between Connections", Journal of Electronic Manufacturing , Vol.3, pp.85-94.

[64] Williams, D.J. and Whalley, D.C., Boyle, O.A. and Ogunjumi, A.O. (1993), "Anisotropic Conducting Adhesives for Electronic Interconnection", Journal of Soldering and Surface Mount Technology, Vol.14, pp.4-8.

[65] Yim, M.J., and Paik, K.W. (1998), "Design and Understanding of Anisotropic Conductive Films (ACFs) for LCD Packaging", IEEE Transactions on Components, Packaging and Manufacturing Technology- Part A, Vol.21, pp.226-234.

[66] Shi, F.G., Abdullah, M., Chungpaiboonpatana, S., Okuyama, K., Davidson, C. and Adams J.M. (1999), "Electrical Conduction of Anisotropic Conductive Adhesive: Effect of Size Distribution of Conducting Filler Particles", Material Science in Semi-conducting Processing, Vol.2, pp.263-269.

[67] Chiang, K.N., Chang, C.W. and Lin, J.D. (2000), "Analysis of ACA/ACF package Using Equivalent Spring Method", Proceeding of the 50th IEEE Electronics Packaging Technology Conference, Las Vegas, pp.110-116.

[68] Määttänen, J. (2003), "Contact Resistance of Metal-coated Polymer Particles Used in Anisotropically Conductive Adhesives", Journal of Soldering and Surface Mount technology, Vol.15, No.1, pp.12-15.

[69] Dou, G., Chan, Y. C. and Liu, J. (2003), "Electrical Conductive Characteristics of Anisotropic Conductive Adhesive Particles", Journal of Electronic Packaging, ASME, Vol.125, pp.609-616.

[70] Shiozawa, N., Isaka, K. and Ohta, T. (1995), "Electric Properties of Connections by Anisotropic Conductive Film", Journal of Electronic Manufacturing, Vol.5, No.1, pp.33-37.

[71] Liu, J. (1999), Conductive Adhesives for Electronics Packaging, Electrochemical Publications Ltd, Port Erin, Isle of Man. Chapter 8, pp.189.

[72] Dou, G., Whalley, D. C. and Liu, C. (2004), "Electrical Conduction Characteristics of Solid Metal Anisotropic Conductive Adhesive Particles", the 4th International IEEE Conference on Polymers and Adhesives in Microelectronics and Photonics, Portland, Oregon, pp.132-136.

[73] Tummala, R.R. (1998), *Fundamentals of Microsystems Packaging*, Published by McGraw-Hill, ISBN: 0-07-137169-9, pp.342-397.

[74] Larson, M.C., Verges, M.A. and Liu, X. (2006), "Residual Compression in Area Array Packages Induced by Underfill Shrinkage", Journal of Microelectronics and Reliability, Vol.46, Issue: 2-4, pp. 496-502.

[75] Wolf, M.J., Engelmann, G., Dietrich, L. and Reichl, H. (2006), "Flip Chip Bumping Technology-Status and Update", Journal of Microelectronics Reliability, Vol.565, Issue: 1, pp: 290-295.

[76] Ho, P.S., Wang, G.T., Ding, M., Zhao, J.H., Dai, X. (2004), "Reliability Issues for Flip-Chip Packages", Introductory Invited Paper for Journal of Microelectronics Reliability Vol.44, pp.719–737.

[77] Lau, J.H., Chang, C. (1999), "TMA, DMA, DSC and TGA of Lead Free Solders", Journal of Soldering & Surface Mount Technology, Vol.11, No. 2, pp.17-24.

[78] Environment Agency, "The Restriction of Hazardous Substances in Electrical and Electronic Equipment" (ROHS) Directive 2002/95/EC, www.environmental-agency.gov.uk

[79] EC Directive on Waste Electrical & Electronic Equipment (WEEE). DTI. Sustainable Development. www.dti.gov.uk

[80] Directive 2000/53/EC of the European Parliament & Council of 18th Sept 2000. End of Life Vehicles.

[81] Kim, K.S., Yu, C.H., Yang, J.M. (2006), "Tin Whisker Formation of Lead-free Plated Lead Frames", Journal of Microelectronics Reliability, Vol.46, pp.1080–1086.

[82] Fang, T., Osterman, M., Pecht, M. (2006), "Statistical Analysis of Tin Whisker Growth", Journal of Microelectronics Reliability, Vol.46, pp.846–8491.

[111]Crank, J. (1956), *The Mathematics of Diffusion*, Oxford University Press, Ely House, London, pp.1-50.

[112]Jain, A., Gupta, V., Basu, S.N.(2002), "A Quantitative Study of Moisture Absorption in Polyimide and Its Effect on The Strength of the Polyimide/Silicon Nitride Interface", Journal of Acta Materialia, Vol.53, pp.3147-3153.

[113]Dubek, R., Walter, H. and Michel, B. (2002), "Studies on Moisture Diffusion and Popcorn Cracking", Proceedings of the 3rd IEEE Conference on Benefiting from Thermal and Mechanical Simulation in Micro-Electronics, Paris, pp.225-232.

[114]Wong, E. H., Teo, Y. C., Lim, T. B., (1998), "Moisture Diffusion and Vapour Pressure Modelling of IC Packaging", Proceedings of the 48th IEEE Electronic Components and Technology Conference (ECTC), pp.1372-1378.

[115]Wong, E.H., Koh, S.W., Lee, K.H. and Rajoo, R. (2002), "Advanced Moisture Diffusion Modelling and Characterisation for Electronic Packaging", Proceedings of the 52nd of IEEE Electronic Component and Technology Conference (ECTC), pp.1297-1303.

[116]Wong, E.H., Chan, K.C., Rajoo, R. and Lim, T.B. (2000), "The Mechanics and Impact of Hygroscopic Swelling of Polymeric Materials in Electronic Packaging", Proceedings of the 50th of IEEE Electronic Component and Technology Conference (ECTC), pp.576-580.

[117]Tee, T.Y. and Ng, H.S. (2002), "Whole Field Vapour Pressure Modelling of QFN during Reflow with Coupled Hygro-mechanical Thermo-mechanical Stresses", Proceedings of the 52nd Electronic Components and Technology Conference (ECTC), pp.1552-1559.

[118]Tee, T.Y., Kho, C.L., Yap, D., Toh, C., Baraton, X. and Zhang, Z. (2003), "Reliability Assessment and Hygro-swelling Modelling of FCBGA and No-flow Underfill", Journal of Microelectronics Reliability, Vol.43, pp.741-749.

[119]Kirsten, W.Z., Walter, H., Hélène, F. (2005), "Moisture Diffusion in Printed Circuit Boards: Measurements and Finite-Element-Simulations", Journal of Microelectronics Reliability, Vol.45, pp.1662-1667.

[120]Ardebili, H., Hillman, C., Natishan, M.A.E., McCluskey, P., Pecht, M.G. and Peterson, D. (2002), "A Comparison of the Theory of Moisture Diffusion in Plastic Encapsulated Microelectronics With Moisture Sensor Chip and Weight-Gain Measurements", IEEE Transactions on Components and Packaging Technologies, Vol.25, No.1, pp.132-139.

[121]Liu, J., Wang, Y., Morris, J. and Kristiansen, H. (2005), "Ontology for the Anisotropic Conductive Adhesive Interconnect Technology for Electronics Packaging Applications",

Proceedings of the Seventh IEEE CPMT Conference on High Density Microsystem Design, Packaging and Failure Analysis (HDP'05), pp.156-172.

[122] Yim, M.J., Ryu, W., Jeon, Y.D., Lee, J., Kim, J., Paik, K.W. (1999), "Microwave Model of Anisotropic Conductive Adhesive Flip-Chip Interconnections for High Frequency Applications", Proceeding of the 49th Electronic Components & Technology Conference (ECTC), pp.488-492.

[123] Fan, S.H. and Chan, Y.C. (2002), "Effect of Misalignment on Electrical Characteristics of ACF Joints for Flip Chip on Flex Applications", Journey of Microelectronics Reliability, Vol.42 No.7, pp.1081-1090.

[124] Dou, G.B., Whalley, D.C., Liu, C.Q. (2006), "Effect of Co-planarity Variation on Anisotropic Conductive Adhesive Assemblies", Proceedings of the 56th Electronic Components & Technology Conference (ECTC), San Diego, USA, pp.932-938.

[125] Liu, J (2001), "Life Time Prediction of Anisotropic Conductive Adhesive Joints during Temperature Cycling for Electronics Interconnect", Proceedings of the 1st International IEEE Conference on Polymers and Adhesives in Microelectronics and Photonics, pp.209-212.

[126] Yin, C.Y., Alam, M.O., Chan, Y.C., Bailey, C. and Lu, H. (2003), "The Effect of Reflow Process on the Contact Resistance and Reliability of Anisotropic Conductive Film Interconnection for Flip Chip on Flex Applications", Journal of Microelectronics Reliability, Vol.43, pp.625-633.

[127] Yin, C.Y., Lu, H., Bailey, C. and Chan, Y.C. (2004), "Effects of Solder Reflow Process on the Reliability of Flip-Chip on Flex Interconnections Using Anisotropic Conductive Adhesives", IEEE Transactions on Electronics Packaging Manufacturing, Vol.27, No.4, 2004, pp.254-259.

[128] Yin, C.Y., Lu, H., Bailey, C. and Chan, Y.C (2006), "Macro-Micro Modelling Analysis for an ACF Flip Chip", Journal of Soldering and Surface Mounting Technology, Vol.18, No.2, pp.27-32.

[129] Yin, C.Y., Lu, H., Bailey, C. and Chan, Y.C (2003), "Using the Anisotropic Conductive Adhesive (ACA) for Flip-Chip Interconnects" Proceeding of Postgraduate Research Conference in Electronics, Photonics, Communications and Software (PREP), pp.89-90.

[130] Yin, C.Y., Lu, H., Bailey, C. and Chan, Y.C (2003), "Experimental and Modeling Analysis of the Reliability of the Anisotropic Conductive Films", Proceeding of the 53rd Electronic Component and Technology Conference (ECTC), pp.698-702.

[131]Yin, C.Y., Lu, H., Bailey, C. and Chan, Y.C (2004), "Effects of Reflow Process on the Reliability of Flip Chip on Flex Interconnections Using Anisotropic Conductive Adhesives", Proceeding of the International IEEE Conference on Asian Green Electronics (AGEC), pp.240-245.

[132]Lu, H., Bailey, C., Yin, C., Stoyanvo, S. (2004), "Modeling the Reliability of Green Electronic Interconnects", Proceedings of the International IEEE Conference on Asian Green Electronics (AGEC), pp.63-67.

[133]Yin, C.Y., Lu, H., Bailey, C. and Chan, Y.C (2005), "Moisture Effects on the Reliability of Anisotropic Conductive Films", the 6th International Conference on Thermal, Mechanical and Multiphysics Simulation and Experiments in Micro-Electronics and Micro-Systems (EuroSimE 2005), Berlin, pp.162-167.

[134]Yin, C.Y., Lu, H., Bailey, C. and Chan, Y.C (2005), "Experimental and Modeling Analysis on the Moisture Induced Failures in Flip Chip Interconnections with Anisotropic Conductive Adhesives", International IEEE Conference on Asian Green Electronics (AGEC), ShangHai, pp.172-177.

[135]Yin, C.Y., Lu, H., Bailey, C. and Chan, Y.C (2005), "Macro-Micro Modeling Analysis for High Density Packaged Flip Chips", the 7th International IEEE CMPT Conference on High Density Packaging and Component Failure Analysis (HDP'05), Shanghai, pp.105-108.

[136]Yin, C.Y., Lu, H., Bailey, C. and Chan, Y.C, (2005) " Moisture Effects on the Reliability of Anisotropic Conductive Film Interconnection for Flip Chip on Flex Applications", Proceedings of InterPACK: The Pacific Rim/ASME International Electronic Packaging Technical Conference and Exhibition, San Francisco.

[137]Yin, C.Y., Lu, H., Bailey, C. and Chan, Y.C (2005), "Modeling of the Performance of Flexible Substrates for Lead-Free Applications", Proceedings of the 7th Electronic Packaging Technology Conference (ECTC), Singapore, pp.342-346.

[138]Yin, C.Y., Lu, H., Bailey, C. and Chan, Y.C (2005), "Moisture Effects on the Reliability of ACF Interconnections", Electronics World, pp.20-25, ISBN: 9-770959-833103.

[139]Dieter, G.E. (1988), *Mechanical Metallurgy*, McGraw-Hill Book Company Ltd. ISBN: 0-07-084187-X, pp.17-68.

[140]Taylor, G.A. (1996), "A Vertex Based Discretisation Scheme Applied to Material Non-Linearity within a Multi-Physics Finite Volume Framework", A thesis for the Doctor of Philosophy of the University of Greenwich.